SAPIENZA
UNIVERSITÀ DI ROMA

Facoltà di Ingegneria

Dipartimento di Scienza e Tecnica dell'Informazione e Comunicazione

Dottorato di Ricerca in Telerilevamento
Ciclo XXX

Sounder Data Processing and Techniques for Geophysical Parameters Estimation

Maria Carmela Raguso

A thesis submitted for the degree of

Doctor of Philosophy

2017

Supervisor: L. Piazzo
Co-Supervisor: R. Seu

TABLE OF CONTENTS

Abstract

In the last decade the interest in radar systems for the exploration of planetary bodies and for Earth Observation (EO) from orbit increased considerably. The main reason for this is the capability of radars to overcome limitations of passive systems and thanks the intrinsic properties of the transmitted signals, which make it possible to retrieve information also from parts of the targets which are even not visible such as ice thickness, internal layers structures and basal environment on Earth as well as on extraterrestrial planets such as Mars.

The use of radars for the subsurface analysis is a well-known technique exploited for more than forty years on the Earth first with surface-mounted ground penetrating radars (GPRs) and later with airborne RSs. Thanks to their Nadir-looking geometry and the use of long wavelengths, these can provide vertical profiles of the subsurface, showing the subsurface stratigraphy with high detail and reaching several kilometers of depth. GPRs and RSs are thus key instruments for the study of the subsurface of icy and arid regions, which are nowadays of high interest as they provide information about the past and present climate of our planet and for the detection and mapping of subsurface water or ice reservoirs that can be indicators of life in the Solar System. Therefore, in the last ten years two orbiting RSs operated at Mars: the Mars

Advanced Radar for Subsurface and Ionosphere Sounding (MARSIS), onboard the European Space Agency's (ESA) orbiter Mars Express and operating since August 2005; the Shallow Radar (SHARAD) mounted on the Mars Reconnaissance Orbiter and operating since November 2006.

One of the major problems on sounding is related to the limitations in resolution. The resolution of radar surface and subsurface imaging using normal pulse compression algorithms is limited by the bandwidth of the transmitted signal, and depends on the sharpness of the signal's auto correlation function. Meanwhile, for high penetration depth, low frequency electromagnetic wave is commonly employed by SRs so that the bandwidth of transmitted signal in the SRs system is usually narrow. Therefore, it is difficult to widen bandwidth in order to obtain high resolution radar subsurface imaging by using conventional pulse compression method. To achieve the desired resolution, the radar should have a large bandwidth but in many practical applications, this may not be possible or desired. The radar may have bandwidth restrictions. Thus, algorithms with improved resolution are desired for radar imaging.

For obtaining high resolution radar surface and subsurface imaging with limited data, in the past decade, spectral estimation techniques have been approved as an adaptive way for radar imaging processing. Autoregressive (AR) based spectral estimation techniques have been used in radar imaging. Using these techniques, one can improve the range (or cross range resolution, if necessary) of a radar image. The idea is to estimate the down range (and/or cross-range) profiles using the autoregressive model and use the AR model for extrapolating the scattering field data beyond the measured range.

In this thesis, the use of a data extrapolation technique is proposed for improve range resolution in Radar Sounders data. By means of three AR methods: The Burg method, Modified Covariance method and Yule-Walker method, the extrapolation coefficients of the linear auto-regression model are calculated. Using the AR algorithms, the unknown coefficients of the AR model are computed independently for the spectral data of each radar pulse. The coefficients are then used in linear prediction filters to extrapolate the received signal before the pulse compression performed via Fourier transformation.

First, we present a theoretical and empirical statistical study of the properties of the AR methods employed for radar data extrapolation. Such a study drives the development of a multi-layer simulator for the generation of the surface and subsurface radar echoes. Assumed sinusoidal periodicities in the received radar signal, the study exploits the ability of the AR methods to fit the measured data and the capacity of the linear prediction filters to perform an accurate bandwidth extrapolation (BWE) over the available radar bandwidth. The quality of the different data extrapolation methods is investigated with various signals and SNR configurations and model orders.

The second part is focused on the analysis of AR methods behavior on data acquired by two planetary sounders: MARSIS and SHARAD and by the Cassini radar in altimetry mode. Qualitative and quantitative experimental results obtained on real planetary RS data will show the effectiveness of the proposed methods according to the results of simulator developed in this thesis. Finally, the third contribution is a technique for reconstruct the sounder radar data affected by electromagnetic interferences (EMI). Signal interferences is a major concern in the radar processing, they often dominate and obscure the radar returns from target and degrade the resulting sounder product. The proposed method is based on the automatic detection of the interferences that affected the SHARAD spectrum, their suppression and the following reconstruction of the frequency gaps in the range domain using the bandwidth extrapolation techniques previously studied as bandwidth interpolator.

Chapter 1

Fundamentals and Background

1.1 Basic Radar Principles

The term RADAR was coined in 1940 by United States Navy and is a contraction of words: Radio Detection and Ranging. Radars are electromagnetic systems used for the detection and the location of reflecting objects such as aircraft, ships, spacecraft, people, vehicles and natural environments. It operates by radiating energy into space and detecting the echo reflected from the target. This reflected energy not only indicated the presence of a target, but by comparing the received echo signal with the transmitted one we can obtain also range informations.

A transmitter generates an electromagnetic signal which is radiated into space by an antenna. A portion of this energy is intercepted by the target and reradieted in many directions. the portion directed back towards the radar is received by the radar antenna and delivered to the receiver. Since radar pulses propagate at the speed of light, the range to the target is proportional to the time it takes between the transmission and the reception of the radar echo [1].

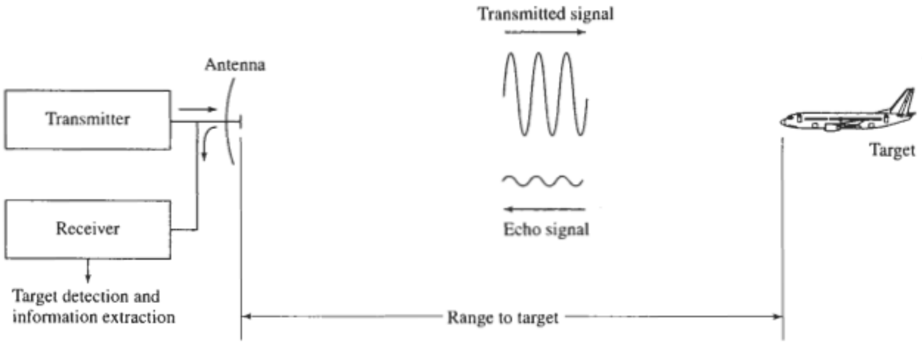

Fig. 1.1 Basic Radar Principles.

1.1.1 The Simple Form of The Radar Equation

The fundamental relation between the characteristics of the radar, the target and the received signal is called the *Radar Equation*. It is useful not only for determining the maximum range at which a particular radar can detect a target, but also for understanding the factors affecting radar performances [1]. When a power P_t is transmitted by an isotropic antenna, the power density at distance R form the radar is equal to the radiated power divided by the spherical surface of radius R.

$$P(R) = \frac{P_t}{4\pi R^2} \tag{1.1}$$

Radars, however, employ directive antennas to cancentrate the radiated power in a particular direction. So power density at range R from a directive antenna with a transmitting gain G is then

$$P(R,\theta,\phi) = \frac{P_t G(\theta,\phi)}{4\pi R^2} \tag{1.2}$$

The target intercepts a portion of the incident energy and reradiates it in various directions and also to the radar. The radar scattering cross-section σ is a function of the directions of the incident wave as well as of the scatter shape and dielectric properties and determines the power density back towards to the radar. The radar antenna captures a portion of the echo energy incident on it and the final form of the equation is obtained

$$P_r(R,\theta,\phi)=\frac{P_t G(\theta,\phi)\sigma}{4\pi R^2(4\pi R^2)}A_{eff} \tag{1.3}$$

Since the effective area of an antenna is related to its gain we can rewrite the radar equation as

$$P_r(R,\theta,\phi)=\frac{P_t G(\theta,\phi)^2\lambda^2\sigma}{(4\pi)^3 R^4} \tag{1.4}$$

The maximum range of the radar $R_{\max}$ occurrs when the received signal power P_r is the minimum signal detectable by radar ($P_r=S_{\min}$) and represents the distance beyond which the target cannot be detected.

$$R_{\max}=\left[\frac{P_t G(\theta,\phi)^2\lambda^2\sigma}{(4\pi)^3 S_{\min}}\right]^{1/4} \tag{1.5}$$

Except the radar cross section, others equation parameters are under control of the radar designer [2]. Now referring to radar equation if we want achieve long distance, the radiated energy should be concentrated into a narrow beam, the receiver should be more sensitive to weak signals and transmitted power should be larger. The form given in (1.5) is for the so-called monostatic radar Fig.1.2, this basic equation may be modified to take into account other factors, such as receiver noise, signal processing, attenuation caused by a radome, attenuation due to atmospheric losses or precipitation, and various other losses and propagation effects.

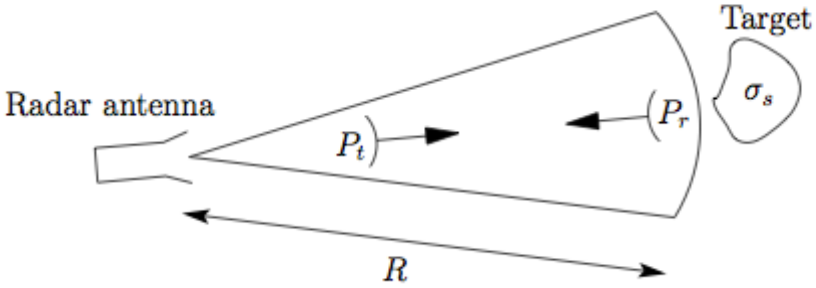

Fig. 1.2 Monostatic Radar Configuration.

1.2 Radar Sounder

Radar Sounding is a nonintrusive technique which allows the investigation of the structural and dielectric characteristics of the subsurface. A radar sounder generates an high-power pulse which is radiated by the antenna towards the surface, some of the energy impinging on the surface will be transmitted to the subsurface structures or dielectric discontinuities and will then travel towards the next reflecting interface. When this energy pulse encounters the second layer interface, some of it will be returned toward the sounder and some will be transmitted to the next layer [3].

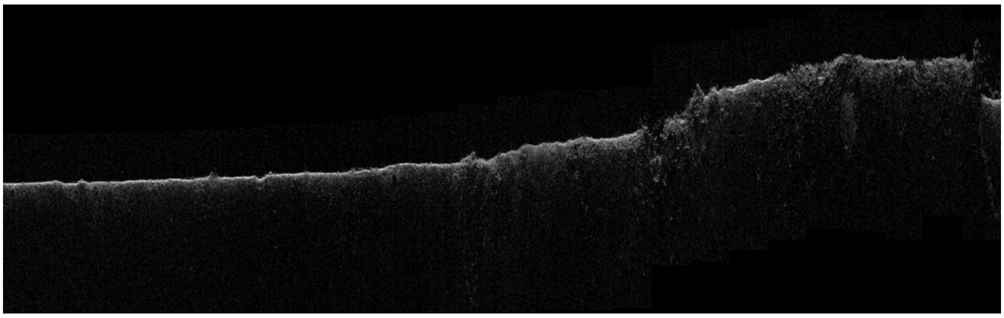

Fig. 1.3 SHARAD Data Product 2389801.

Radar sounders data are usually stored as a radargrams. Radargrams are 2D images that represent the radar recorded echo power color-coded in shades of gray for a given range position as a function of time (or distance) on one axis and of the along-track position on the other. As an example, Fig. 1.3 shows a radargram acquired by SHARAD instrument, each column of the image is an individual frame, where brighter pixels corresponding to the higher power levels.

1.2.1 Principles and Acquisition Geometry

Radar sounders are conceptually simple; 3D acquisition geometry is shown in Fig. 1.4. Sounders are usually mounted on a platform which flies at an altitude of h_0 from the ground where (x_0,y_0) represents the radar nadir point. If we denotes with (x,y) a generic position of the surface characterized by an elevation h(x,y), the distance from this generic position to the radar is R(x,y), which is:

$$R(x,y) = \sqrt{(x-x_0)^2 + (y-y_0)^2 + (h_0 - h(x,y))^2} \qquad (1.6)$$

A transmitter generates a high-power pulse which is radiated by the antenna towards the surface and penetrates the subsurface where is attenuated by the medium. When this energy pulse encounters a dielectric discontinuity, a portion of it travels back to the received antenna and is recorded as a function of travel time.

The knowledge of the velocity of propagation of the transmitted wave into the medium is important in order to translate the recorded signal from the time domain to the depth domain. Time delay t is proportional to depth z according to the following equation:

$$z = \frac{vt}{2} \quad where \quad v = \frac{1}{\sqrt{\mu\varepsilon}} = \frac{1}{\sqrt{\mu_r \varepsilon_r}\sqrt{\mu_0 \varepsilon_0}} \tag{1.7}$$

Where 2 at the denominator is necessary to convert time to range and ε_r force propagation velocity, in fact the higher the dielectric permittivity the lower the speed into it. Due to transmission and attenuation losses, the returns from the subsurface should be much weaker then those of the surface. In order to transmit enough energy, the transmitted waveform must be spread over a much longer period for obtain the desired time resolution, then the longer pulse must be “compressed” to achieve the desired resolution and to isolate weak subsurface returns that are too close to the strong surface echo [5].

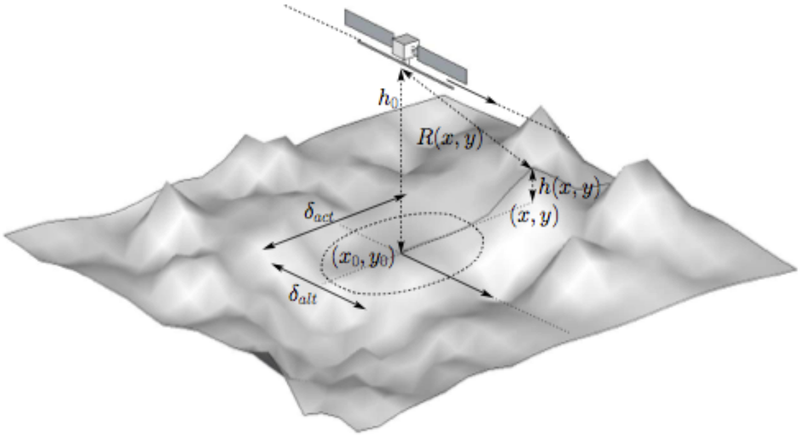

Fig. 1.4 Acquisition Geometry of a Radar Sounder.

1.3 Synthetic Aperture Radar

The Synthetic Aperture Radar is a radar using for mapping of the ground and imaging of stationary objects. SAR is unique in its imaging capability: it provides high-resolution two-dimensional images independent from daylight, cloud coverage and weather conditions. The radar system transmits electromagnetic pulses with high power and receives the echoes of the backscattered signal in a sequential way. The range resolution is obtained with either a conventional short-pulse or a pulse-compression waveform while resolution in cross-range is obtained by synthesize the effect of a large antenna aperture [1].

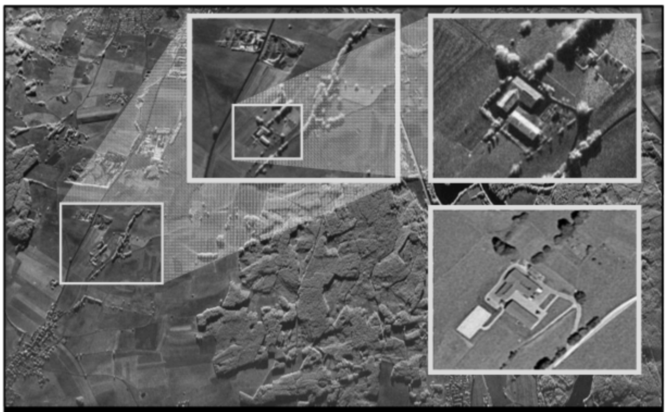

X-band, High Resolution Airborne SAR, F-SAR, Kaufbeuren, Germany

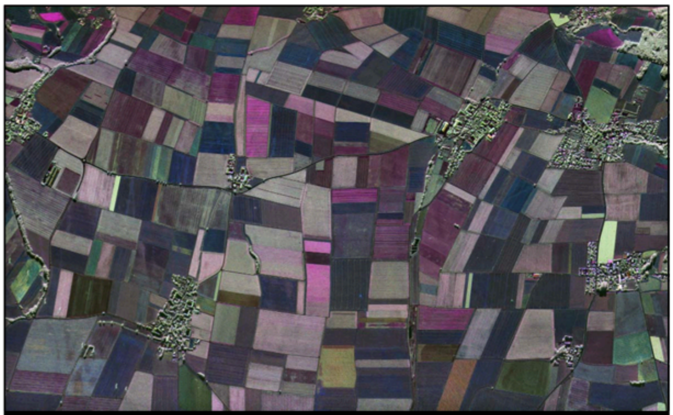

C-band, Airborne SAR, F-SAR, Full Polarimetric

Fig. 1.5 SAR images.

1.3.1 Acquisition Geometry

Synthetic Aperture Radars were developed as a means of overcoming the limitations of real aperture radars. A synthetic aperture is produced by using the forward motion of the radar. As it passes a given scatterer, many pulses are reflected in sequence, by recording and then combining these individuals signals, a "Synthetic Aperture" is created in the computer providing a much improved azimuth resolution.[13] The platform flies along-track at a constant velocity v, with an altitude h_0 and carries a side-looking radar antenna that illuminates Earth's surface with its beam. Considering the platform as the reference coordinate system, we can distinguish two directions: across-track (or range direction) and along-track (or azimuth direction). In the first case, we should also distinguish between slant-range (the direction identified by the conjunction between the target and the platform) and ground-range (slant-range projection on the ground). Figure 1.6 illustrates these directions.

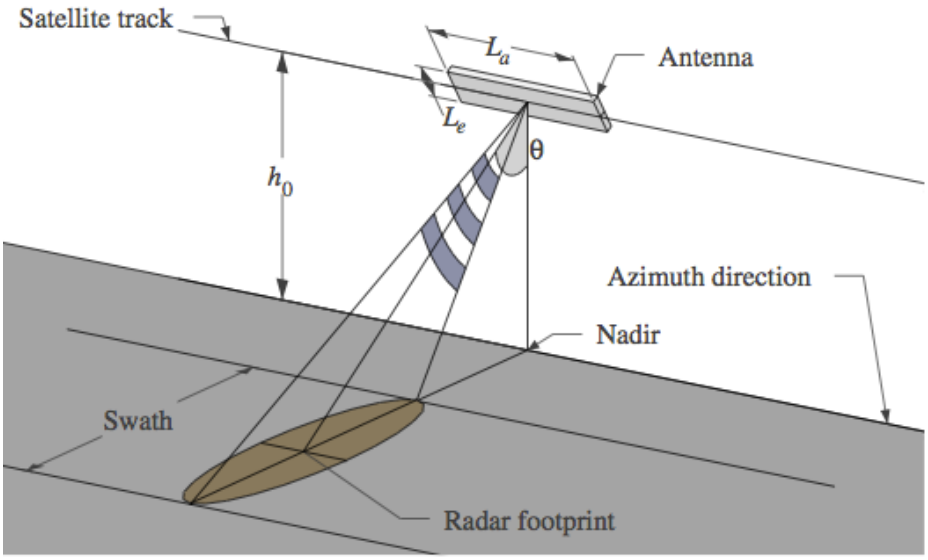

Fig. 1.6 Illustration of SAR acquisition geometry

The footprint of the main lobe of the radar beam on the ground can approximated by an ellipse with the following axes:

$$w_x = R\cdot\theta_{3dB,a} = \frac{h_0\cdot\theta_{3dB,a}}{\cos(\theta)}$$
$$w_y = R\cdot\theta_{3dB,e} = \frac{h_0\cdot\theta_{3dB,e}}{\cos^2(\theta)} \tag{1.8}$$

where:

$$\theta_{3dB,a} = \frac{\lambda_c}{L_a} \qquad and \quad \theta_{3dB,e} = \frac{\lambda_c}{L_e} \tag{1.9}$$

are the azimuth and elevation antenna beamwidth and L_a and L_e are azimuth and elevation antenna dimensions. (see Fig.1.7)

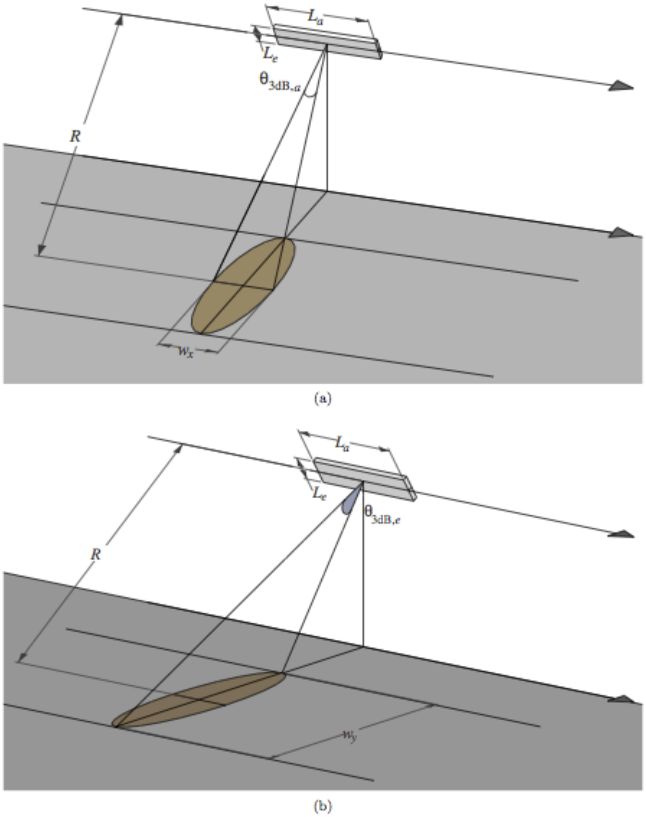

Fig 1.7 Angles and antenna footprint sizes of SAR systems. (a) Azimuth (b) Range direction.

1.3.2 SAR Resolution

Range resolution in a radar system consists in its ability to distinguish two objects separated by some minimum distance. If the objects are adequately separated, each will be located in a different range resolution cell, if not the radar will return a complex combination of two objects signals. Pulse compression techniques with matched filter processing are used for obtain high range resolution and high SNR at the same time. For achieve these results, SAR systems use a linear frequency modulated pulses called chirps, which have the power proprieties of the long pulse and resolution proprieties of the short pulse. Fig.1.8

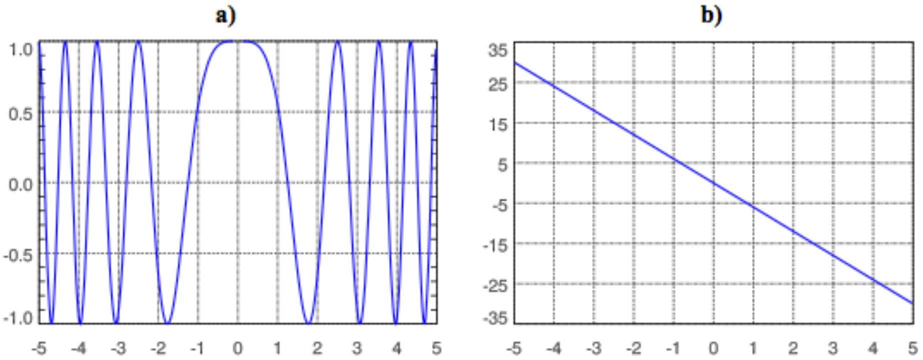

Fig. 1.8 Chirp pulses: a) Complex Amplitude, b) Istantaneous frequency.

The slant-range resolution δ_{slr} (Fig.1.9) is defined as the minimum distance in range beyond which two targets cannot be resolved by SAR system. The ground-range resolution δ_{act} instead depends on the local incident angle and will change nonlinearly across the swath, in fact if we consider two ground-range resolution referred to near and far range we obtain that far range resolution is better then near range one. If we consider a short-range airborne system, for incident angles between 15° and 60°, this means that system would have ground-range resolution at far range that are a factor 0.3 of resolution at near range. In this situation features that are completely distinguishable at the far range can become invisible at near range. [10]

$$\delta_{slr} = \frac{c}{2 \cdot B}$$

$$\delta_{act} = \frac{c}{2 \cdot B \cdot \sin\theta} \rightarrow if \quad \begin{array}{c} \theta_F > \theta_N \\ \sin\theta_F > \sin\theta_N \end{array} \quad so \;\; \delta_{Nact} > \delta_{Fact} \tag{1.10}$$

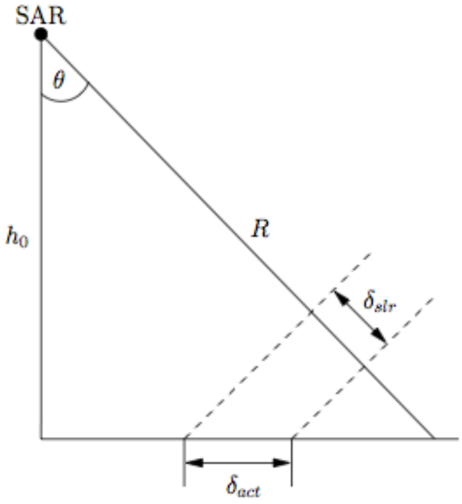

Fig. 1.9 Slant and ground-range geometry.

The pulse compression in range is a standard form used in many sorts of radars, the particular technology of SAR manifests itself in the azimuth direction. The azimuth processing is called SAR focusing and is equivalent to synthesizing a large antenna of length L_{SA} from the pulses backscattered by a given scatter as the beam passes over it. [10] The time during which the target is illuminated by the azimuth's beam of the real antenna determines the extension of this synthetic aperture.

$$T_{SA} = \frac{\theta_{AZ} \cdot R_0}{V_S} = \frac{\lambda \cdot R_0}{L_{SA} \cdot V_S} \tag{1.11}$$

the extension of the synthetis aperture is related to the length of the trajectory described by the platform during T_{SA}

$$L_{SA} = V_S \cdot T_{SA} = \frac{\lambda \cdot R_0}{d_a} \tag{1.12}$$

and the archievable azimuth resolution is:

$$\delta_{az} = \frac{\lambda}{2L_{sa}} \cdot R_0 = \frac{d_a}{2} \tag{1.13}$$

where the factor 2 comes because the 2-way pattern of synthetic array has the same shape as the one way pattern of the real antenna of twice of lenght. Therefore, the azimuth resolution of a SAR sensor is only dependent on the length of the actual antenna, but not on the distance between sensor and target. From Eq. (1.11), the SAR azimuth resolution is half the real antenna dimension in the azimuth direction and is independent on range and wavelength. This resolution is obtained for a SAR operating in STRIPMAP MODE, when the antenna pointing direction is fixed. [10] [11]

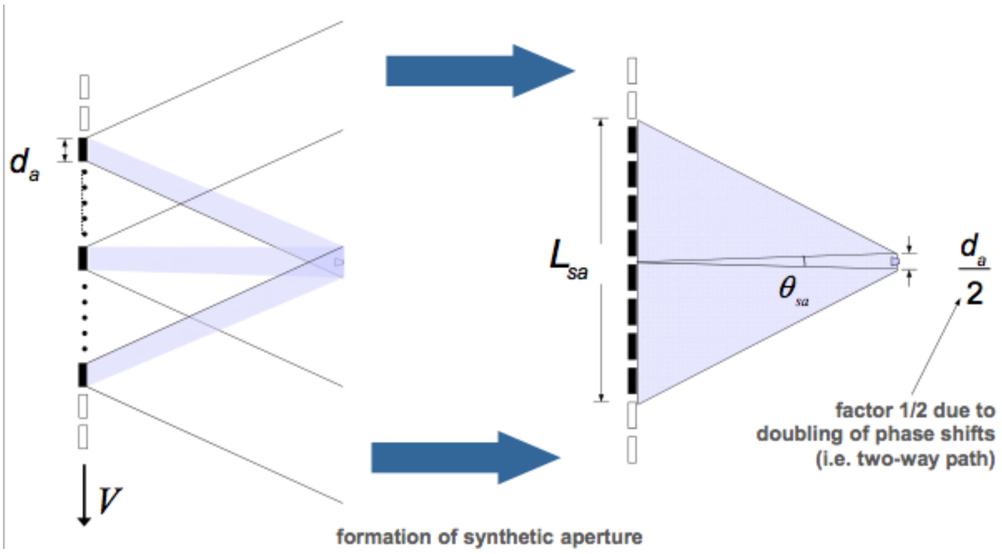

Fig. 1.10 SAR azimuth processing.

A higher resolution is obtained if the beam is steered (electronically) to keep the target in the beam for a larger time in order to form a longer synthetic antenna. This SAR mode is called SPOOT LIGHT and is capable of improving azimuth resolution considerably at the expense of spatial coverage. [10]

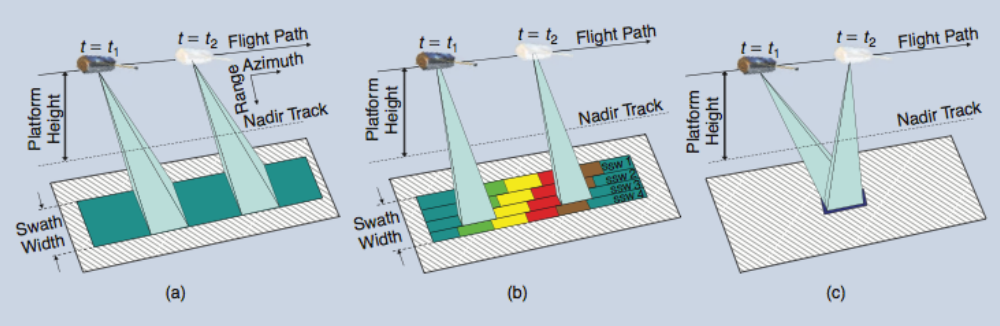

Fig. 1.11 Illustration of different SAR operation modes use for improve azimuth resolution: (a) Stripman, (b) ScanSAR, (c) Spotlight.

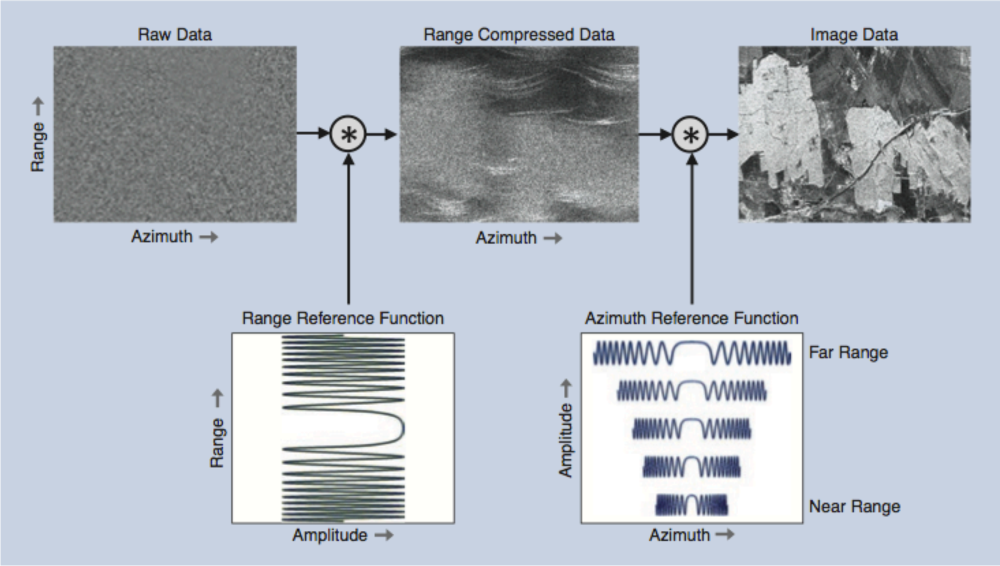

Fig. 1.12 Summary of SAR processing steps.

1.4 Radar Altimeter

1.4.1 Altimetry Principles

The principal objective of a radar altimeter is to measure the range R from the satellite to target surface. The altimeter transmits a short pulse of microwave radiation with pre-defined power toward the target surface and measures the time it takes to reach the surface. The pulse interacts with the rough surface and part of the incident radiation is reflected back to the altimeter. Since electromagnetic radiation travels with speed of light in vacuum the distance from the satellite to the surface (R_0) is in first approximation given by:

$$R_0 = c(t_0/2) \tag{1.14}$$

where c is the speed of light and t_0 the two-way travel time measured by the altimeter. The range defined in equation 2.1 is overestimated. If the medium is not the vacuum we have to consider the correction due to the refraction. For that reason the range R from the satellite to surface is estimated by:

$$R = R_0 - \sum_j \Delta R_j \tag{1.15}$$

where R_0 is the range computed neglecting refraction index and ΔR_j , j=1,....,N are corrections for the various components of the atmospheric refraction and for biases between the mean electromagnetic scattering surface and mean reference target surface.

The range estimate (1.15) varies along the satellites orbit from along-track variations of both the surface topography (mainly sea-surface) and the orbit height relative to the centre of the Earth. For more accurate mission requirements, as oceanography, the range estimate must be transformed to a fixed coordinate system. As introduced in section 3, this is achieved by precision orbit determination of the height *H* of the satellite relative to center of mass above the reference ellipsoid. The range measurements are then converted to the height *h* of the target surface relative to reference ellipsoid by:

$$R = H - R_0 = H - R_0 + \sum_i \Delta R_j \qquad (1.16)$$

A primary characteristic in design of an altimeter system is the area on the target surface over which the range from the altimeter to the reference surface height is measured. The footprint of an antenna is traditionally described in terms of the beam-limited footprint, defined to be the area on target surface within the field of view subtended by the beam width of the antenna gain pattern. For a narrow-beam antenna, the antenna beam-width can be expressed as:

$$\gamma = 2tan^{-1}\left(\frac{r}{R}\right) \approx 2\frac{r}{R} \qquad (1.17)$$

where *r* is the footprint radius and *R* is the orbit range.

The limitation of the beam-limited altimeter design can be overcome by transmitting a very short pulse with duration of a few nanoseconds (pulse- limited configuration) from an antenna with a smaller diameter and correspondingly wider beamwidth. The qualitative difference between these two modes is that the illuminated area on the surface is determined by the antenna beamwidth or transmitted pulsewidth, respectively. In order to indicate which mode is being used, the geometry of the altimetry must be examined. Figure 1 shows a nadir oriented antenna operating above a mean surface from the altitude *h*. The antenna beamwidth is given as BW and the transmitted pulsewidth is PW. The diameter of the area of the circle on the surface that is within the beamwidth is:

$$d_B = 2h\,tan\left(\frac{BW}{2}\right) \tag{1.18}$$

Furthermore, the area of the circle formed by the intersection of the leading edge of the pulse with the mean surface when the trailing edge just intersects the surface at nadir point has a diameter given by:

$$d_P = 2\sqrt{(h + cPW)^2 - h^2} \tag{1.19}$$

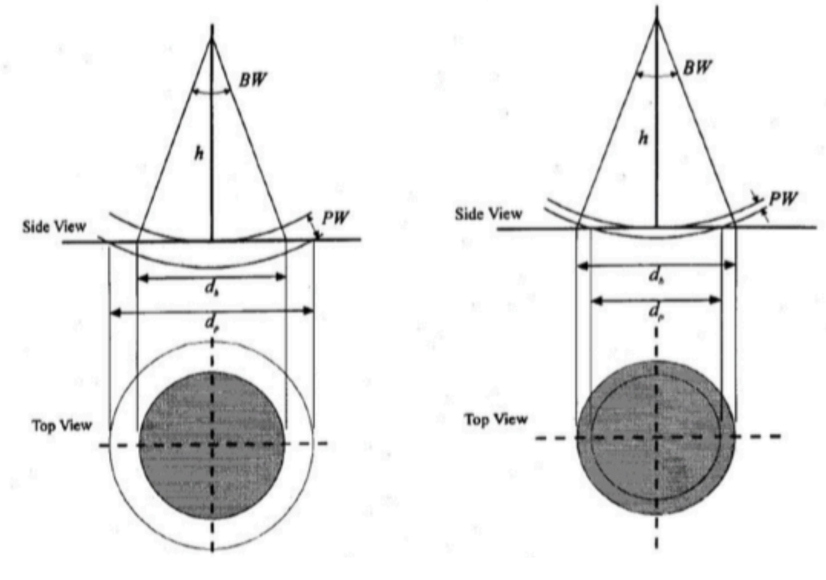

Fig. 1.13 Geometry of a nadir oriented (sx) beamwidth-limited altimeter and (dx) pulsewidth-limited altimeter.

1.4.2 Off-Nadir Altimetry Technique

Conventional altimeter provides a surface topography profile along the flight line. In most cases, the scientific requirement is to acquire surface topography over two-dimensional surface. A first intuitive solution to the problem of spatial and temporal sampling for the ocean or land observations is represented by the modification of the conventional Pulse Limited radar altimeter concept by extending its limited, although high performing, nadir looking measurement capability with the inclusion of off-nadir measurements taken from additional antenna beams pointed off-nadir. The individual beam's footprints should be spaced in the horizontal plane to achieve the swath widths needed for various scientific applications. The extent of the footprints is determined by the beam forming antenna system. Figure 1.14 shows the geometry of the acquisition for these kind of systems.

The individual beam's footprints should be spaced in the horizontal plane to achieve the swath widths needed for various scientific applications. The extent of the footprints is determined by the beam forming antenna system. The addition of off-nadir beams creates a remarkable increase in the number of intersections (crossovers) between ascending and descending tracks.

The instantaneous surface footprint of a real aperture imaging altimeter usually defines the superficial resolutions *Xr* and *Xa* in the cross track and along track dimensions, respectively. The height resolution (ΔH) depends on the surface slope, illumination geometry, and sensor characteristic.

Being ξ the off-nadir angle, the echo will be spread as a result of the oblique geometry as shown in Figure 1.14 and expressed by the following relation:

$$\Delta \mathrm{H} = \frac{H\,\theta_B \tan(\xi)}{\cos(\xi} \qquad (1.20)$$

where θ_B is the angle between the half power points of the main beam.

This causes an echo spread that leads to a decrease in the total height measurement accuracy. This effect can be reduced by analysing the total echo shape instead of measuring the time of arrival of the leading edge, but this implies an accurate satellite attitude control system. A possible solution to the attitude estimation problem is to model the expected return waveforms for a range of off-nadir angles and compare them to the measured return. This method requires huge data storage and, inevitably, long processing times.

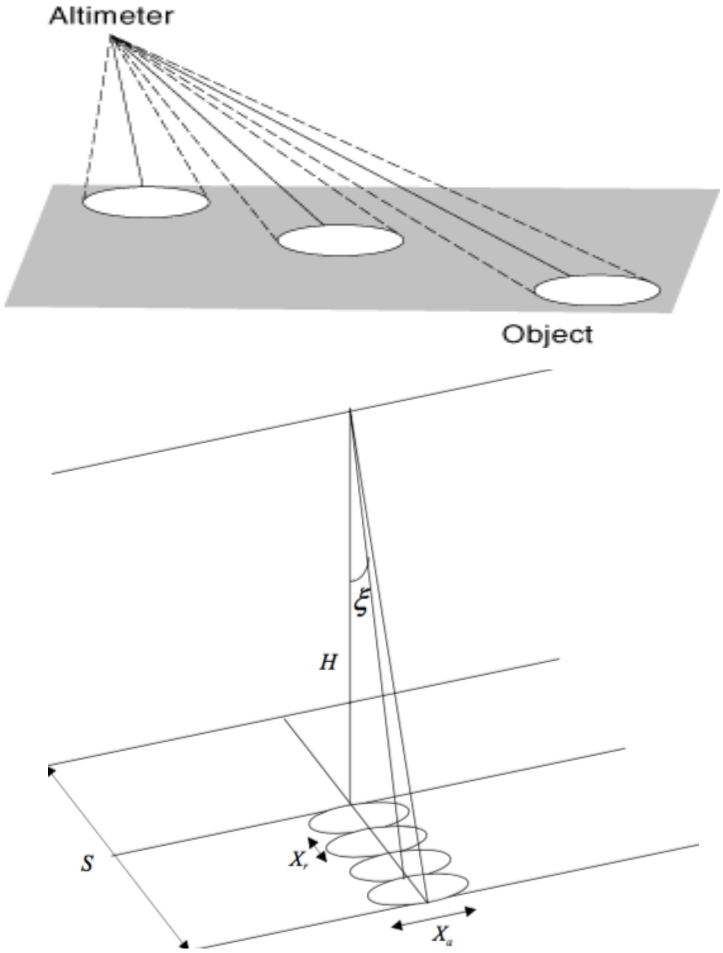

Fig.1.14 Geometry of an off-nadir radar altimeter.

Chapter 2

Planetary Explorations

2.1 An overview of the geological history of Mars

Mars is the fourth planet in the solar system in order of distance from the Sun and the second smallest planet in the Solar System, after Mercury. It has approximately half the diameter of Earth (equatorial radius is 3398 km), less dense then earth, having about 15% of Earth's volume and 11% of the mass. (Fig.2.1) and it's one of the five planets that can be easily seen with the naked eye if one knows when and where to look. Mars is easily recognised since it has a distinctive coloration, infact it's popularly called "The Red Planet" because the iron oxide (rust) prevalent on its surface gives it a reddish apparence. The characteristic red color of Mars is basically due to the fact that the planet's soil is rich in ferrous components that, for millions of years exposed to oxygen and water vapor in the atmosphere reacted oxidizing. This massive presence of iron on Mars is due to the fact that during the early stages of the birth of the solar system it had, in planetary terms, a very fast cooling and the iron ores mixed the surface and the mantle, in opposite of what happened to our planet where the metal compounds are precipitated into the nucleus through the fractures of the mantle driven by gravity, the size and mass.

Of all the planets in the solar system, the seasons of Mars are the most Earth-like, thanks to its topographical and orbital properties similar to those on Earth (i.e. the rotational period is a little over 24 hours and similar tilts of the planets' rotational axes) which makes this planet, the most fascinating for future explorations and also for the creation of human settlements in the future.

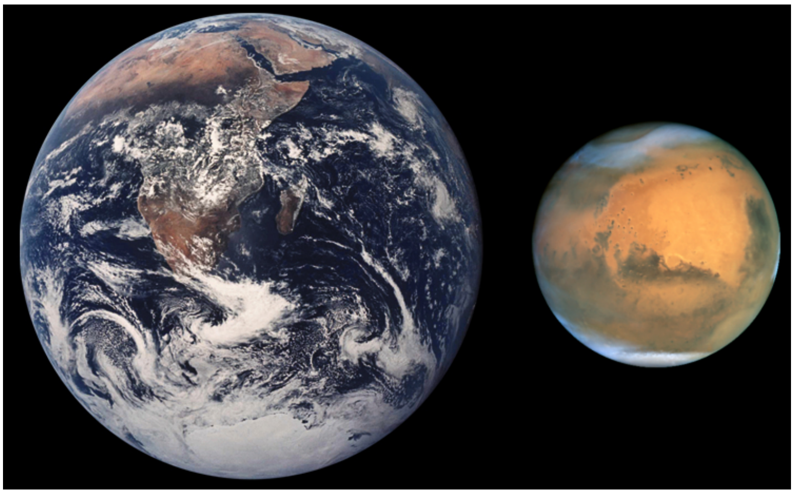

Fig.2.1 Mars Earth Comparison

Differing in situ values have been reported for the average temperature on Mars, with a common value being -55°C, Martian surface temperature may reach a high of about 20°C at summer noon and a low of about -153 °C at the winter polar caps, this wide range of temperatures is due to its thin atmosphere which cannot store much solar heat and its very low atmospheric pressure.

The image below shows the nighttime (2 AM) temperature of the Martian surface misured by TES (Thermal emission Spectrometer) instrument on the Mars Global surveyor. Data were acquired during the first 500 orbits of the mission, the coldest temperatures (purple zones) are -120C while the warmest temperatures (white zones) are -65C. As we can see, Valles Marineris (-10S,30-90W) and the channels leading into Acidalia Planitia are clearly visible as regions composed by warm materials (sand and rocks) instead the south polar cap it's the coldest region composed by very fine dust grains.

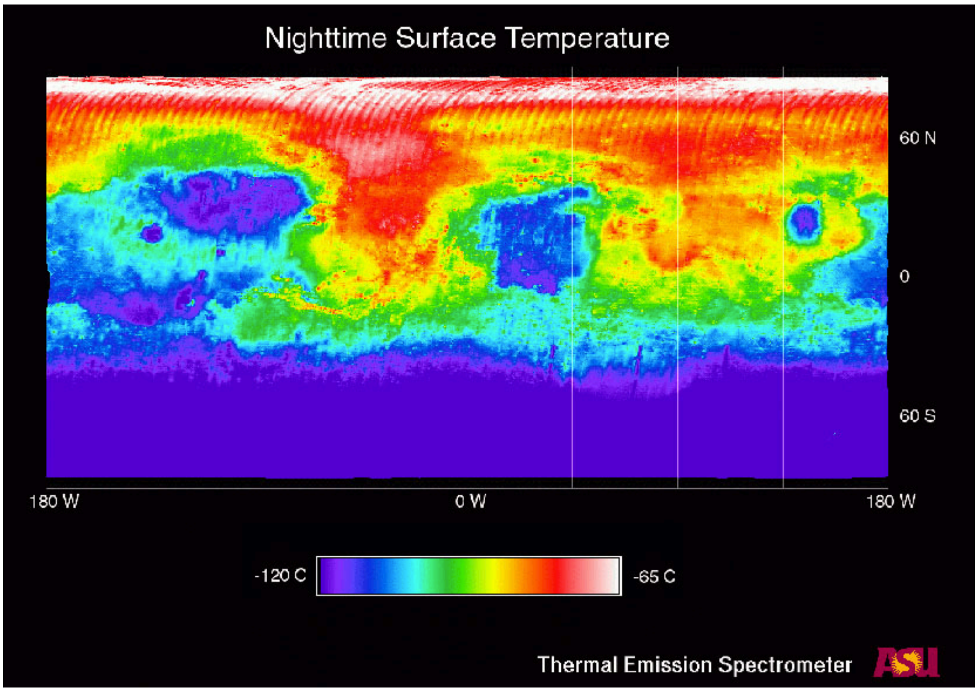

Fig. 2.2 Mars nighttime temperature taken by TES during the MGS mission.

Mars is a terrestrial planet that consists of minerals containing silicon, oxygen and metals, its surface is primarily composed of tholeiitic basalt, silica-rich and iron oxide dust but hematite and pristine olivine have also been found. The first discovery of hematite on Mars hae been documented in 1998, when the infrared spectrometer on Mars Global Surveyor (TES - Thermal Emission Spectrometer) as shown a strong and extensive concentration of gray hematite in the Martian equator called "Sinus Meridiani." This discovery, in addition to others, indicates that liquid water might have been present for relatively short period on the Mars' surface and that a large amounts of liquid water flowed on Mars' surface in the past.

Mars is geologically diverse planet with heavily cratered terrains, huge volcanoes, big canyons, and lots of channels looking like they have been created by running water. On a large scale, the surface is characterized by the so-called Martian hemispheric Dichotomy (Fig. 2.3); the northern hemisphere is covered by plains, sedimentary deposits, where we can see a low density of craters created by ancient impacts, while the southern hemisphere is instead characterized by a high density of craters testifying to the fact that, in the past, Mars was subjected to the so-called "Late Heavy Bombardment" in these areas.

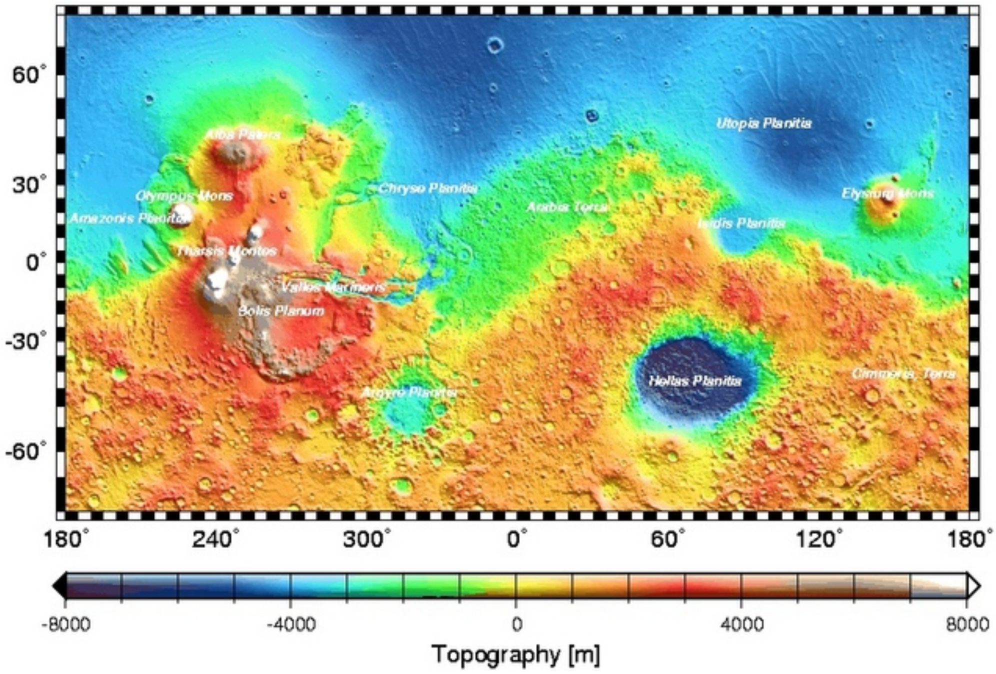

Fig.2.3 Elevation map of Mars based on MGS data

A total of 43,000 craters with a diameter of 5 km or greater have been found on Mars surface. In particular in the southern hemisphere there are some basins due to large impacts, the most impressive of which is the Hellas basin (the blue spot in the Fig. 2.3), a ligth albedo feature clearly visible from Earth. Another very interesting area of the red planet, called Tharsis (shades of red and brown in the Fig. 2.3), lies instead in the

Northern Hemisphere. It is characterized by three massive volcanoes (three white spot in Fig. 2.3) that together with the largest mountain in the solar system, Olympus Mons (average diameter at the base of 500 km and a height of about 24 km), forming an area that probably, in a recent geological past, have had an intense volcanic activity. [15]

Along the equator of Mars, on the east side of the Tharsis Bulge there's Valles Marineris, a system of canyons that runs Martian surface. With its 4,000 km long, 200 km wide and up to 7 km deep, this system is one of the larger canyons of the Solar System. There have been many different theories about its formation, ideas in the 1970s were erosion by water or thermokarst activity or a withdrawal of subsurface magma.

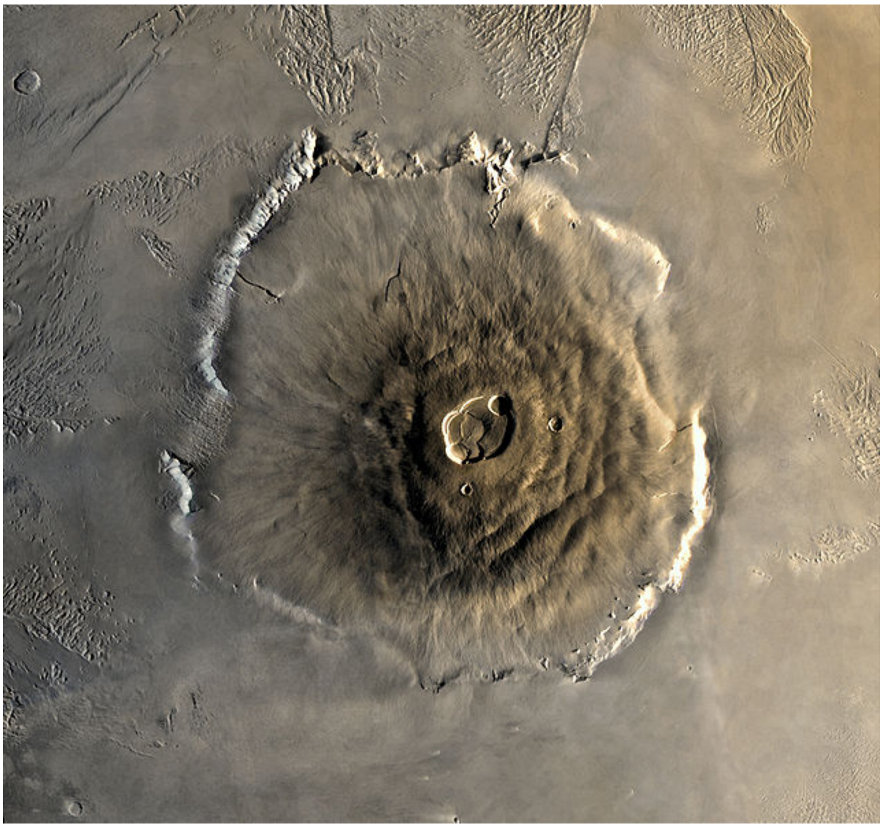

Fig. 2.4 Olympus Mons.

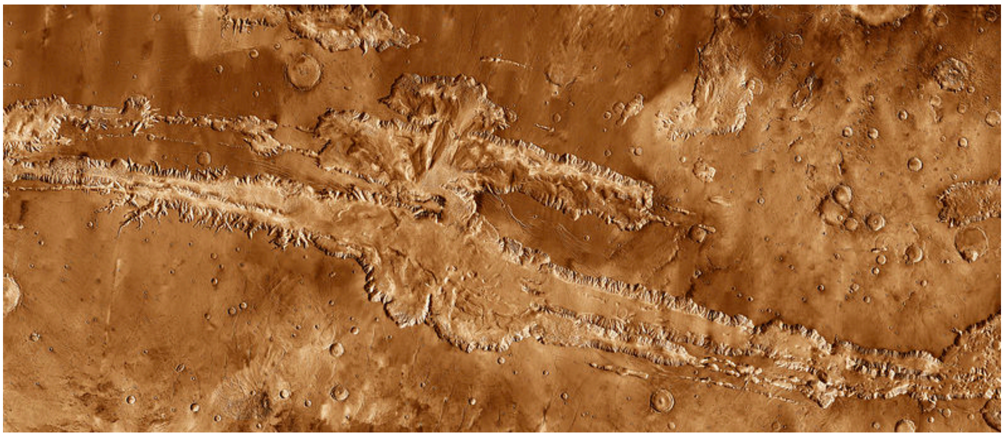

Fig. 2.5 Valles Marineris in mosaic images from 2001 Mars Odissey.

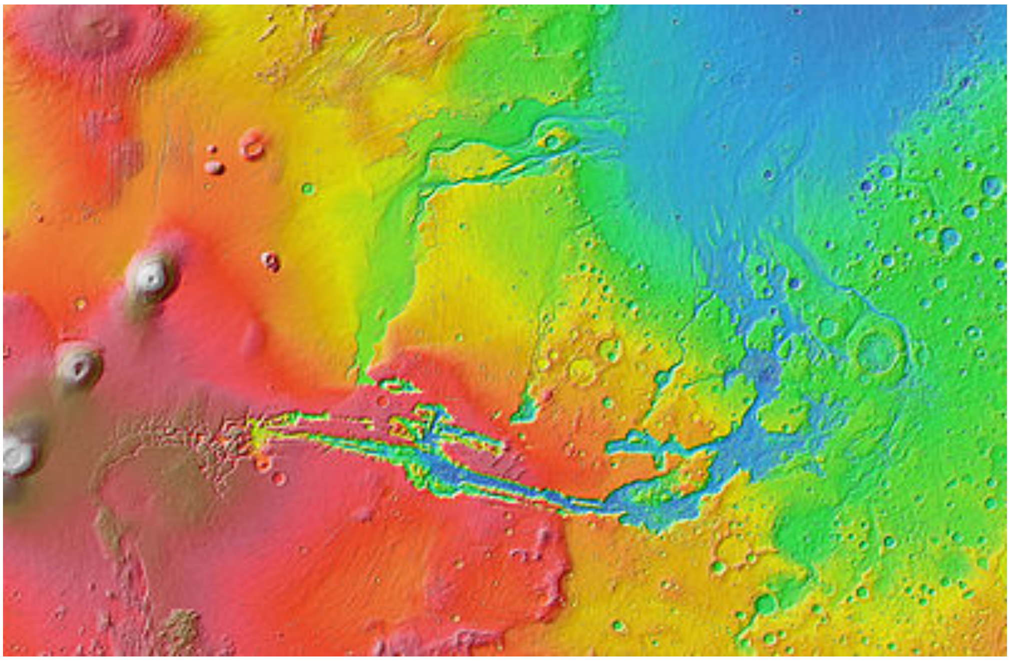

Fig.2.6 Topographic map of Valles Marineris based on MOLA data.

2.2 Space Missions on Mars

Mars has long been the subject of human fascination, its exploration has been an important part of the space explorations (see Table 1). For size, internal activity level, surface structures and atmospheric density, Mars is a body that lies in an intermediate position between Venus and Earth and is the only planet in the solar system where there is probability of finding life forms. Its exploration has therefore been essential for better understanding of the Earth. During the last 50 years, more then ten spacecrafts have been launched toward the planet, including orbiters, landers and rovers. [38] In 1964 NASA lunched Mariner 4, a small exploration spacecraft with a television camera that passed near Mars at a distance of 10 km end providing the first close-up photographs of Martian surface. Thanks to this successfull mission NASA continued the Mariner program with another pair of Mars flyby probes, Mariner 6 and 7. They were sent at the next launch window, and reached the planet in 1969. The mission aim was to study the surface and atmosphere of Mars during close flybys and in total they send back to Earth hundreds of shots covering about 20% of the planet surface. [23]

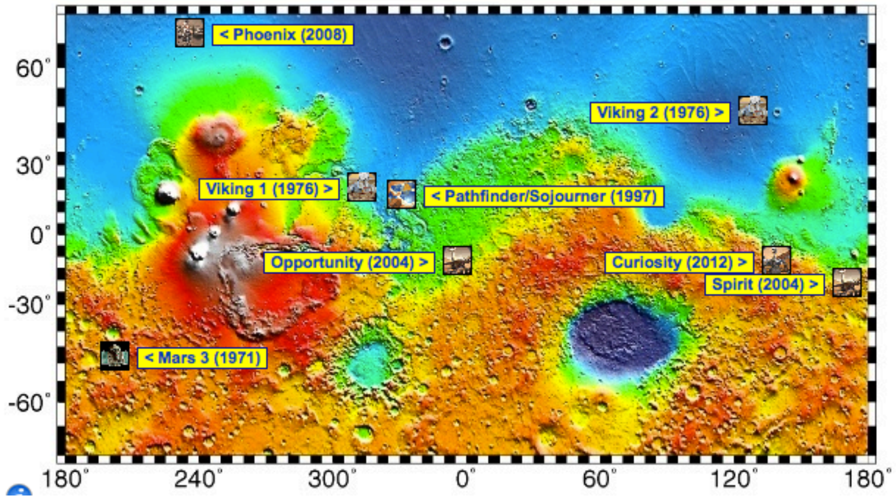

Fig.2.7 Image Map of Mars Landings

The same mission was programmed in 1971 with Mariner 8 and Mariner 9, Mariner 9 successfully entered orbit about Mars after Mariner 8 failure and became the first Martian artificial satellite. It was totally obscured by a dust storm that lasted for a month but after that it returned stunning shots which offer more detailed evidence that liquid water might at one time have flowed on the planetary surface. [38] They also finally discerned the true nature of many Martian albedo features such as Tarsis region and Olympus Mounts and roughly zone parallel to the equator called "Valleys Marineris" in honor of the mission. In 1975 NASA decided to launch two spacecraft, Viking 1 and Viking 2, the program consisted of two orbiters and two landers –an orbiter designed to photograph the surface of Mars from orbit and a lander designed to study the planet from the surface, observe metereologic, seismic and magnetic properties of Mars. The images from the orbiters caused a revolution in our ideas about water on Mars, in fact huge river valleys were found that showed the existance of water in Mars' past.

Lunch Date	**Name**	**Country**	**Result**
Oct.10, 1960 Oct.14, 1960	Korabl 4 Korabl 5	USSR USSR	Failed in Earth Orbit Failed in Earth Orbit
Oct.24, 1962 Nov.1, 1962 Nov.4, 1962	Korabl 4 Mars 1 Korabl 5	USSR USSR USSR	Failed in Earth Orbit Lost communications Failed in Earth Orbit
Nov.5, 1964 Nov.28,1964 Nov.30,1964	Mariner 3 **Mariner 4** Zond 2	USA USA USSR	Lunch failure **Reached Mars July 15** Lost communications
July18, 1965	Zond 3	USSR	Reached Mars orbit
Feb.24, 1969 Mar.27,1969 Mar.27,1969 Apr.14,1969	**Mariner 6** **Mariner 7** None None	USA USA USSR USA	**Flyby July 31, Successful** **Flyby Aug. 5, Successful** Failed Failed
July 21, 1973 July 25,1973	Mars 4 Mars 5	USSR USSR	Failed Partially Successful

Aug. 5, 1973	Mars 6	USSR	Failed
Aug. 9, 1973	Mars 7	USSR	Failed
Aug. 20, 1975	**Viking 1**	USA	**Orbited 1976 June 19;**
Sept. 5, 1975	**Viking 2**	USA	**Orbited 1976 Aug. 7;**
Aug. 5, 1988	Phobos 1	USSR	Lost contact Aug. 31, 1993
Aug. 9, 1988	Phobos 2	USSR	Lost contact Mar 27
Sept. 25, 1992	Mars Observer	USA	Lost Contact Aug 21
Nov. 7, 1996	**MGS**	USA	**Successful**
Nov. 16, 1996	Mars 96	Russia	Failed
Dec. 4, 1996	**Mars pathfinder**	USA	**Successful**
July 3, 1998	Nozomi	USA	Failed
Dec. 11, 1998	Mars Surveyor	USA	Lost contact
Jan. 3, 1999	Mars Surveyor	USA	Lost contact
April 7, 2001	2001 Mars Odyssey	USA	Successful
June 2, 2003	**Mars Express**	**ESA**	**Successful**
June 10, 2003	**“Spirit”**	**USA**	**Successful**
July 7, 2003	**“Opportunity”**	**USA**	**Successful**
Aug. 12, 2005	**MRO**	**USA**	**Successful**
Aug. 4, 2007	**Phoenix Mars**	**USA**	**Successful**

Table 1. Missions To Mars

2.3 Mars Express

In 2003, ESA's Mars Express was launched, carrying instruments for the search of subsurface water, the dynamics of the atmosphere and the surface environment. “Express” originally referred to the speed and efficiency with which it was designed and built, but it’s also referred to the short interplanetary travel made by the spacecraft, a result of being launched when the Earth and Mars were in opposition. The spacecraft borrows technology achieved in the course of the failed Mars 96 mission and from Rosetta mission, launched by ESA in March 2004 and currently en route to comet 67P/Churyumov-Gerasimenko.

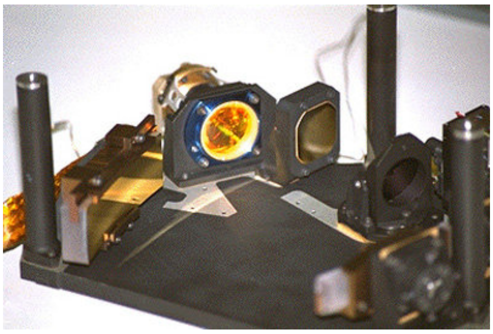

The scientific objectives of the ME mission represent an attempt to fulfill in part the lost scientific goals of the Russian Mars 96 mission. The primary purpose is the mineral characterization at the medium scale of the surface, the study of interaction of the atmosphere with the solar wind, radar sounding of the subsurface structure down to the permafrost and the high-resolution photogeology (10m resolution), mineralogical mapping (100m resolution) and the study of the subsurface structures in search of water or ice.

[15]-[20] These scientific objectives are achieved with the following Mars Express instruments:

- OMEGA - Visible and Infrared Mineralogical Mapping Spectrometer is a visible and near-IR mapping spectrometer, operating in the spectral range 0.38- 5.1 µm. Combining imaging and spectrometry, it studies the mineralogical and molecular composition of the surface and atmosphere of Mars through the spectral analysis of the diffused solar light and surface thermal emission. It providesglobal coverage at medium resolution (2-5 km) for altitudes from 1500km to 4000km, and high-resolution (<350m) spectral images of selected areas.[15]-[16]

- **SPICAM - Ultraviolet and Infrared Atmospheric Spectrometer**. SPectroscopy for the Investigation of the Characteristics of the Atmosphere of Mars consistes in two spectrometers: UV spectrometer addresses key issues about ozone and H_2O coupling, the IR spectrometer is aimed at water abundaces and vertical profiling of water and aerosols. [15]-[19]

- **MARSIS - Sub-Surface Sounding Radar Altimeter .** A radar altimeter, its primary objective is to map the distribution of liquid and solid water in the upper position of the Martian crust but also subsurface probing and ionosphere sounding.[16]-[20]

- **PFS - Planetary Fourier Spectrometer.** Makes observations of atmospheric temperature and pressure, is determining the composition of the Martian atmosphere from the wavelengths of sunlight (in the range 1.2-45 microns) absorbed by molecules in the atmosphere and from the infrared radiation they emit. [15]-[20]

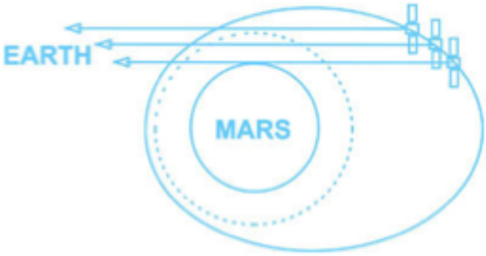

- **ASPERA - Analyzer of Space Plasmas and Energetic Atoms.** Designed to study solar wind and Martian atmosphere interaction and to characterise the plasma and the gas enviroment in near-Mars space. It is measuring ions, electrons and energetic neutral atoms in the outer atmosphere to reveal the number of oxygen and hydrogen atoms. [15]-[20]

- **HRSC - High Resolution Stereo Camera.** Originally developed for the Russian-led Mars-96 mission, produces color images with up to 2 m resolution. Its unique feature is the ability to obtain near-simultaneous imaging data of a specific site at high resolution, with along-track triple stereo, four colours and five different phase angles, thus avoiding any time-dependent variations of the observational conditions.[15]-[19]

- **MELACOM - Mars Express Lander Communications.** Allows Mars Express to act as a communication relay for landers on the Martian surface. (Has been tested with Mars Exploration Rovers and was used to support the landing of NASA's Phoenix mission).[15]-[19]

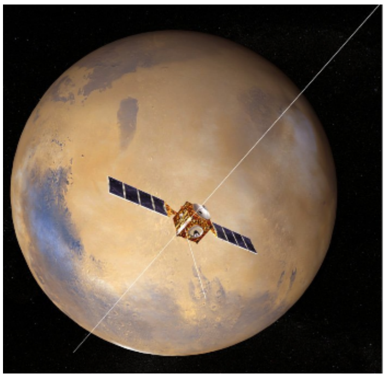

- **MaRS - Mars Radio Science Experiment.** Uses radio signals to sound the neutral martian atmosphere to derive vertical density, pressure and temperature profiles as functions of height. Determine the dielectric and scattering proprieties of the martian surface and gravity anomalies.[15]-[20]

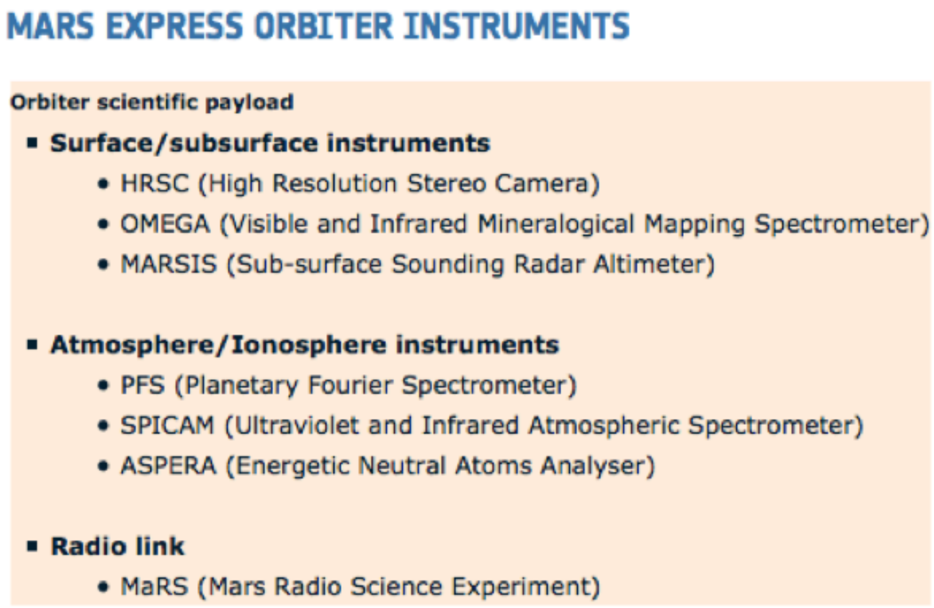

MARS EXPRESS ORBITER INSTRUMENTS

Orbiter scientific payload

- **Surface/subsurface instruments**
    - HRSC (High Resolution Stereo Camera)
    - OMEGA (Visible and Infrared Mineralogical Mapping Spectrometer)
    - MARSIS (Sub-surface Sounding Radar Altimeter)

- **Atmosphere/Ionosphere instruments**
    - PFS (Planetary Fourier Spectrometer)
    - SPICAM (Ultraviolet and Infrared Atmospheric Spectrometer)
    - ASPERA (Energetic Neutral Atoms Analyser)

- **Radio link**
    - MaRS (Mars Radio Science Experiment)

Fig. 2.7 Mars Express Payload.

2.3.1 MARSIS

[15] The MARSIS instrument is a low-frequency nadir-looking radar sounder and altimeter with penetration capabilities, which uses synthetic aperture techniques and a secondary receiving antenna to isolate subsurface reflections. The operation altitudes for MARSIS are up to 800 km above the Martian surface for subsurface sounding and up to 1200 km for ionospheric sounding. In its standard operating mode, the instrument is capable of making measurements in 1 MHz wide bands centred at 1.8, 3.0, 4.0 and 5.0 MHz. A 1MHz bandwidth and a pseudo-linear frequency modilates pulse (chirp) allows a vertical resolution of 150m in vacuum or 50-100m in the subsurface, depending on the EM wave propagation in the terrain. Azimuth compression is performed by coherent unfocused Doppler processing, to reduce along- track surface clutter and noise power; the along-track resolution after azimuth compression is sharpened to 5-9 km (depending on the altitude).

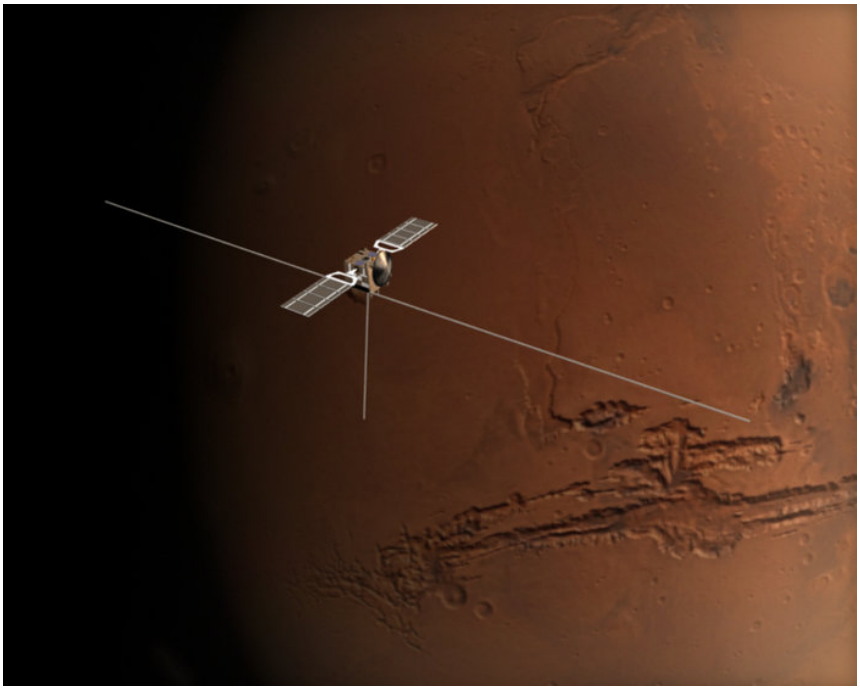

Fig. 2.8 Mars Express in orbita around Mars

Transmitted pulses are radiates through a 40m tip-to-tip dipole (Fig.2.9), the return signal is received on both the primary dipole antenna mounted normally to the direction of motion and from the secondary monopole antenna oriented along the nadir axis. This one receives mostly the off-nadir surface returns that can be subtracted from the main received signal during ground processing in order to reduce surface clutter level (about 15-20 dB).

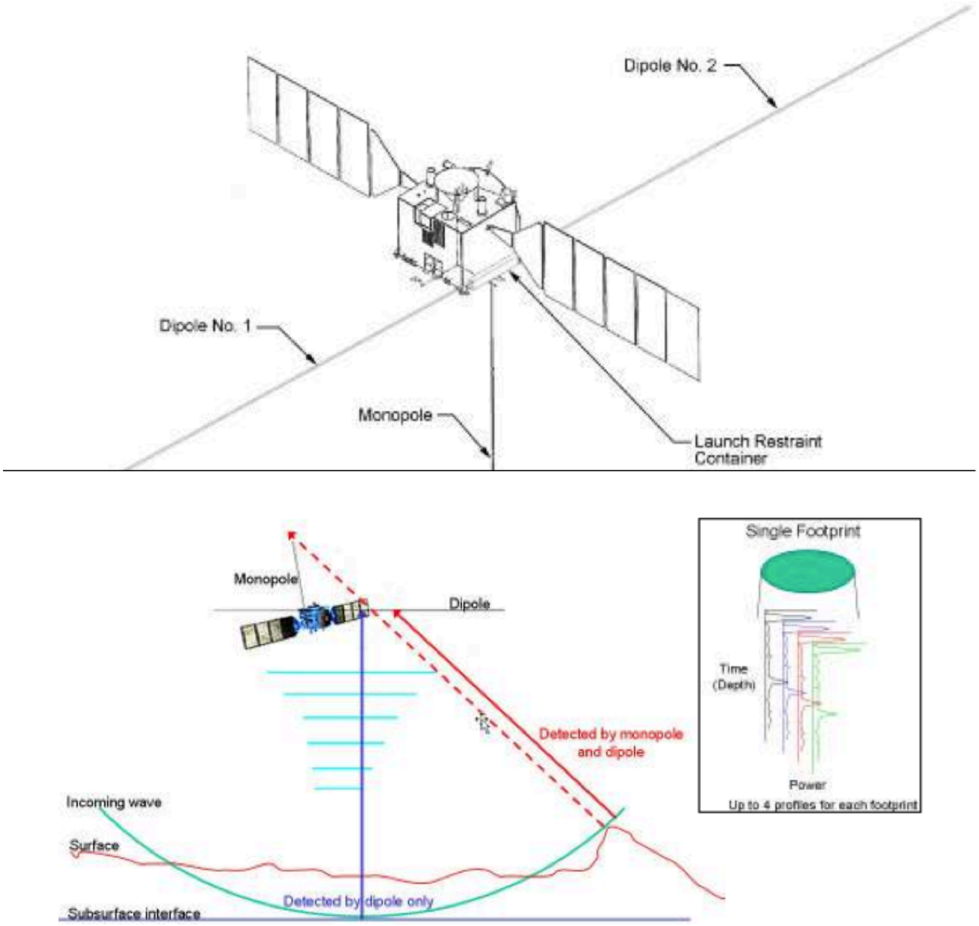

Fig. 2.9 MARSIS dual antenna.

The study of the martian ionosphere is important not only as a topic in its own right, but also because the ionosphere has a strong influence on the subsurface and surface soundings. These measurements employ both passive and active techniques. In passive mode, the thermal emission line at the local electron plasma frequency is used to measure the local electron density. The active technique uses radar soundings to measure the vertical range to the ionospheric reflection point as a function of frequency. [15][21]

MARSIS is composed of three subsystems:

- The Antenna Subsystem (AS)
- The Radio Frequency Subsystems (RFS)
- The Digital Electronics Subsystem (DES)

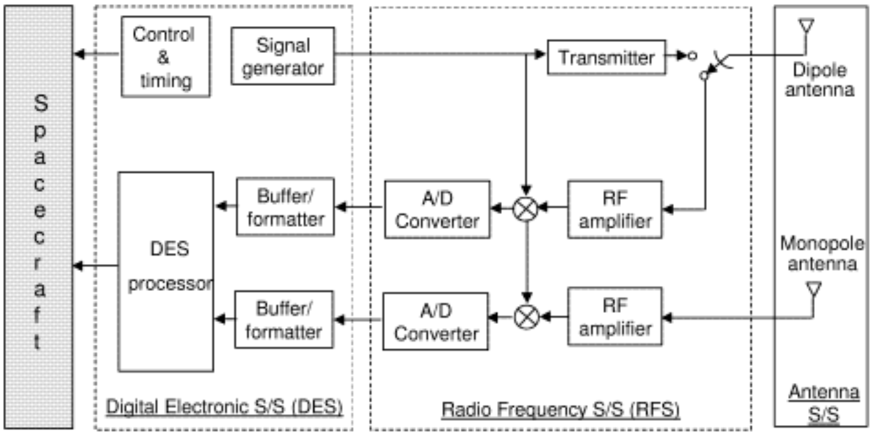

Fig.2.10 MARSIS Subsystems description.

The Antenna Subsystem including the primary dipole antenna with two 20 meter elements, arranged so that its peak gain is in the spacecraft nadir direction. The secondary monopole antenna used for clutter cancellation is a seven meter long, arranged so that its gain null is in the spacecraft nadir direction.

The Radio Frequency Subsystems contains all the radio frequency parts, it consists of a power amplifier, the transmitter which is connected to the primary antenna through an impedance matching network and two receivers to collect echoes from each antennas. Each receiver channel has a selectable bandpass filter, a mixer, an amplifier chain, low-pass filtering and an analogue to digital converter. The output of the A/D converters is passed to the digital electronic subsystem. [21]

[11] The DES contains all the logic for the instrument and the interfaces with the S/C. This subsystem processes the echoes in two separated channels related to each antenna and is also responsible for:

- Processing of the digital data from the receivers
- Receipt and execution of telecommands from the spacecraft
- Control of the transmitter and receivers
- Synthesis of the transmit chirp and local oscillator signals
- Transmission of formatted science, event and housekeeping data to the spacecraft.

2.4 Mars Reconnaissance Orbiter

Mars Reconnaissance Orbiter Nasa mission was launched to Mars in August 2005 and after a seven-month cruise to Mars (from August 2005 to March 2006) and after Mars Orbit Insertion, a check of spacecraft health and six months of aerobraking it entered its final science orbit and began its primary science phase, which still continues today. The purpose of the MRO mission are global mapping of the surface, investigation of subsurface, high-resolution targeting of specific spots on the surface, search for evidence of the presence of water on the red planet and in particular to determine how long the water remained on it and whether life ever arose on it.

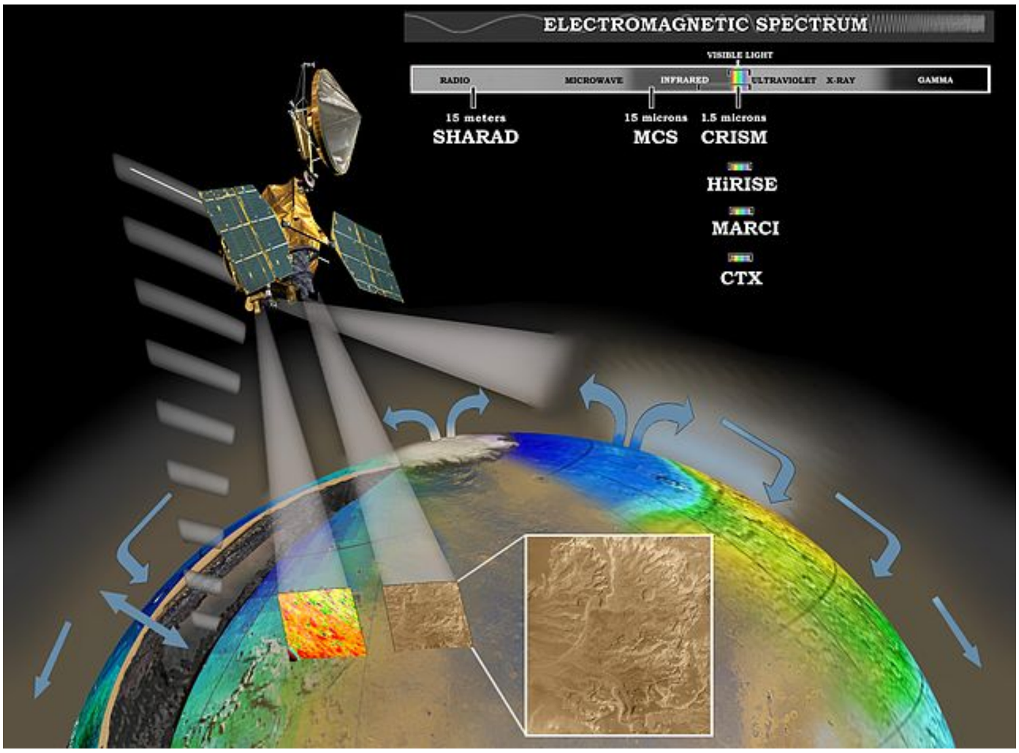

Fig.2.11 Diagram of instrumentation aboard MRO

[16] MRO contains a host of scientific instruments such as 3 cameras, 2 spectrometers and a radar, which are used to analyze the landforms, stratigraphy, minerals, and ice of Mars. The spacecraft carries eleven six instruments, divided in six science instruments, three engineering instruments and two science-facility experiments.

- Cameras

HiRISE ***(High Resolution Imaging Science Experiment)***

This visible camera can reveal small-scale objects in the debris blankets of mysterious gullies and details of geologic structure of canyons, craters, and layered deposits.
Is a 0.5 m reflecting telescope, the largest ever used in a space mission,and had a esolving power of 1 microrad or 0.3 m from an altitude of 300 km. Can receive color images in 3 color bands: red, green, and blue, and infrared. To facilitate the mapping and identification of possible landing sites, HiRISE can produce stereoscopic images where the topographic information will be shown with a definition of 0.25 meters.[20][19]

CTX ***(Context Camera)***

This camera provides wide area grayscale images with a pixel resolution up to about 6m. The optics consist of a 350 mm focal length Cassegrain telescope with a 5,064 pixel wide line array CCD.

MARCI ***(Mars Color Imager)***

This weather camera ia a wide-angle, relatively low-resolution camera that splitthe image of Mars surface in 5 bands of the visible and ultraviolet 2. It produce global maps of the planet with pixel resolution of 1 to 10 km to study the daily changes, seasonal and annual climate and to monitor clouds and dust storms.

- Spectrometer

MCS ***(Mars Climate Sounder)***

Is a 9 channel spectrometer that operate from the visible to the near infrared, in particular one channel operats at 0.3-3 micrometers and the others operating between 12 to 50 micrometers. These channels were selected to measure temperature, pressure, water vapor and dust levels.These measurements are assembled into daily global weather maps to show the basic variables of Martian weather: temperature, pressure, humidity, and dust density.

CRISM (Compact Reconnaissance Imaging Spectrometer for Mars)

is an imaging spectrometer that operates from the visible to the near infrared and aims to identify different minerals, in particular those that would be obtained by the presence of water. It measures the spectrum in 544 channels and has a resolution of 18m at an altitude of 300 km.

- Radar

SHARAD *(SHAllow RADar)*

This sounding radar is designed to probe the internal structure of the Martian polar ice caps. It also gathers planet-wide information about underground layers of ice, rock and possibly liquid water that might be accessible from the surface.

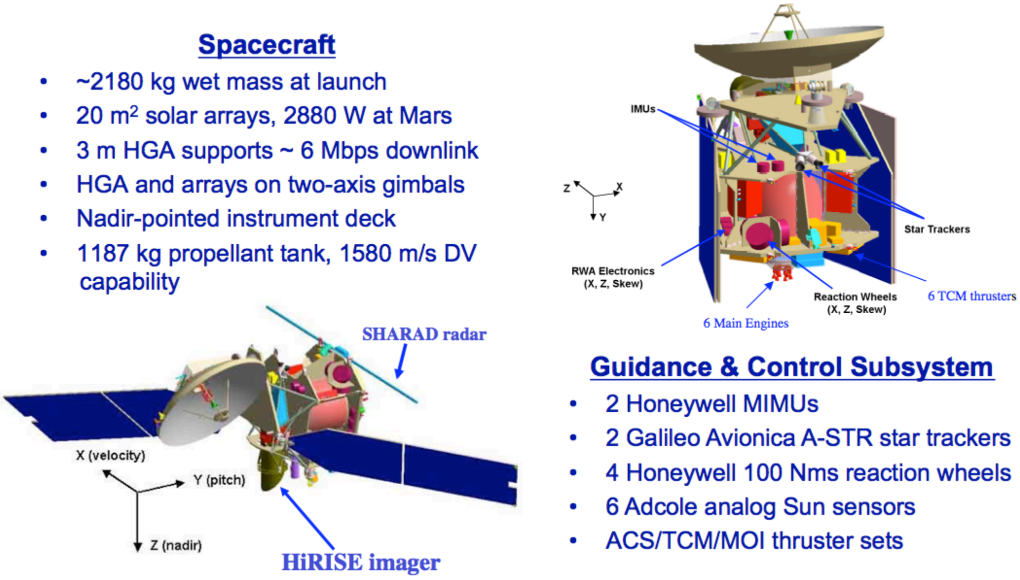

Spacecraft

- ~2180 kg wet mass at launch
- 20 m^2 solar arrays, 2880 W at Mars
- 3 m HGA supports ~ 6 Mbps downlink
- HGA and arrays on two-axis gimbals
- Nadir-pointed instrument deck
- 1187 kg propellant tank, 1580 m/s DV capability

Guidance & Control Subsystem

- 2 Honeywell MIMUs
- 2 Galileo Avionica A-STR star trackers
- 4 Honeywell 100 Nms reaction wheels
- 6 Adcole analog Sun sensors
- ACS/TCM/MOI thruster sets

Fig.2.12 Spacecraft overwiev

Mars Reconnaissance Orbiter carries three instruments that assist the spacecraft navigation and communications. [16]

Electra UHF Communications and Navigation Package

Electra is a UHF software defined radio created to allows the spacecraft to act as a communications relay between the Earth and landed crafts on Mars. Electra also provides Doppler information on landed vehicles that are very helpfull to accurately determine the surface location of Mars landers and rovers.

Optical Navigation Camera

Tested for improved navigation capabilities. in the future would be able to serve as high-precision interplanetary "eyes" to guide incoming spacecraft as they near Mars.

Ka-band Telecommunications Experiment Package

Mars Reconnaissance Orbiter tests the use of a radio frequency called Ka-band to demonstrate its potential for future missions.

In addition to its equipment, MRO carries a variety of Science Facility Experiments:

Gravity Field Investigation Package

By tracking the orbiter in the primary science phase, it measures the variations in the Martinan gravitational field through spacecraft's velocity changes that are detected by measuring the doppler shifts in MRO's signal received on Earth. In this way team menbers are able to map the gravity field and understand geological processes that produce these surface features.

Atmospheric Structure Investigation Accelerometers

Accellerometers used during aerobraking help scientists understand Martian atmosphere.

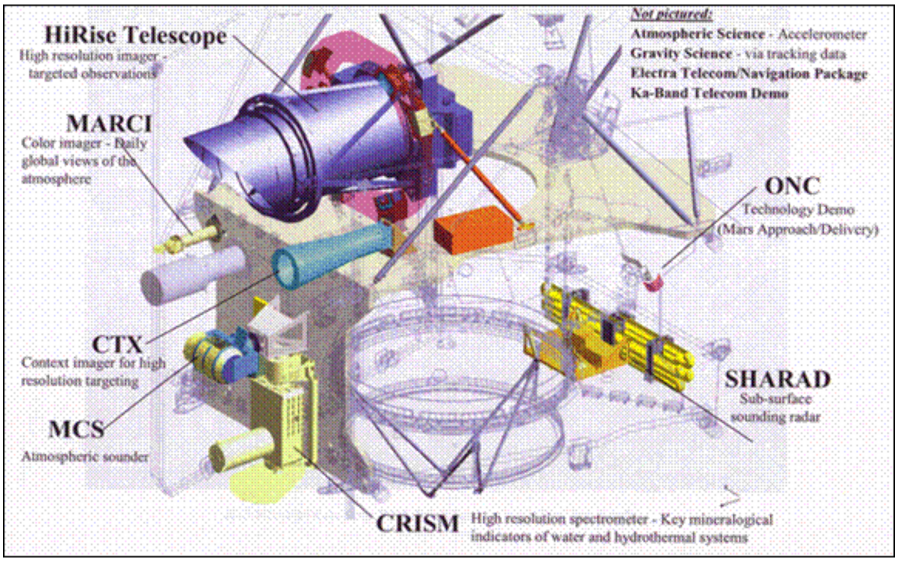

Fig.2.13 Mars Reconnaissance Orbiter' Payload.

2.4.1 SHAllow RADar (SHARAD)

[37][25] SHARAD (SHAllow RADar) is one of the main instruments on board the Mars Reconnaissance Orbiter (MRO), NASA's planetary exploration spacecraft launched in August 2005 and operating in Mars' orbit since the end of 2006. The primary scientific objective of the SHARAD investigation is to map, in selected locales, dielectric interfaces to depths of up to one kilometer in the martian subsurface and to interpret these interfaces in terms of the occurrence and distribution of expected materials, including rock, regololith, water and ice. [13]

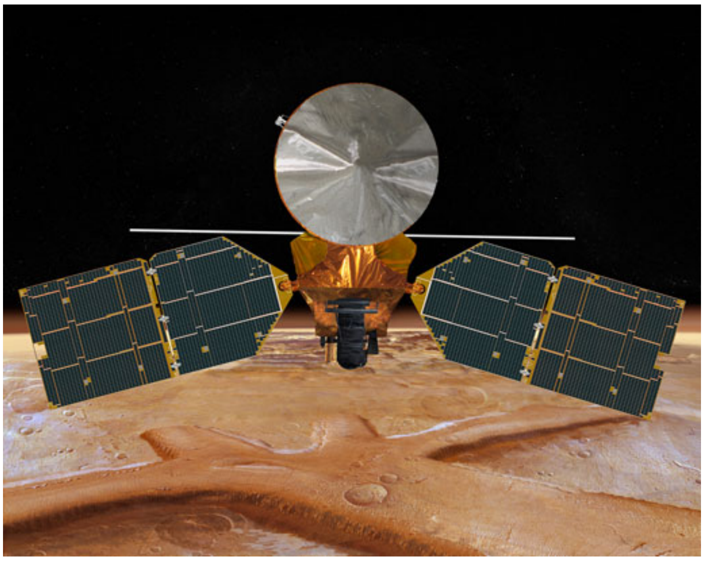

Fig.2.14 Mars Raiconnassaince Orbiter

It’s a sounding radar developed in Italy and supplied to NASA by ASI as a Facility Instrument, is designed to detect dielectric contrasts related to geologic layering on vertical scale of 15m in free space. The radar instrument points to the nadir (nadir-looking) and impulses on two modalities of radar and altimeter. In order to isolate, the reflectors of the subsurface and to reduce the antenna footprint for increase resolution, SHARAD uses the synthetic aperture technique. The radar transmits a

10W, 85μsec chirped pulse with its 10m dipole consisting of two fiberglass tubes (Fig. 2.13) and collects the surface and subsurface reflections.

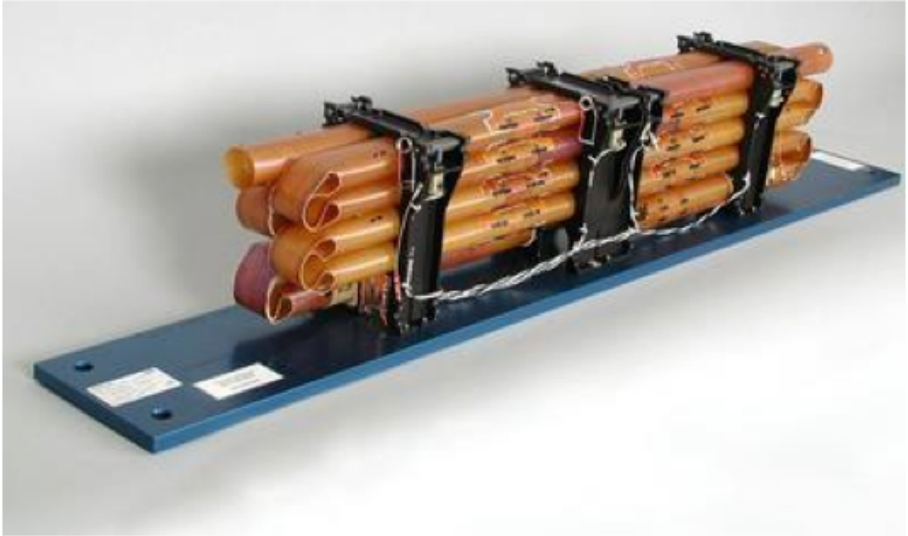

Fig. 2.15 SHARAD 10m dipole folded for launch.

As discussed in the previous chapter, in a radar sounder the surface will reflect some of the energy back toward the radar, typically with a strong ‘‘quasi- specular’’ behavior due to mirror-like reflections from parts of the surface tilted toward the sensor [Hagfors, 1964]. The energy impinging on the surface will be transmitted to the subsurface and will then travel toward the next reflecting interface until encounters the second dielectric interface. A portion of its energy will be returned back toward the sounder while the remainder will be transmitted further downward. As we seen SHARAD employs a “chirp”, a long pulse that is linearly modulated in frequency, to obtain small resolutions, if we supposed to have a subsurface reflector at depth d, this use may produce a subsurface reflection slightly stronger than the sidelobes of the surface reflection limiting the subsurface detection capability of the radar. [Seu et alii, 2007] (Fig. 2.14)

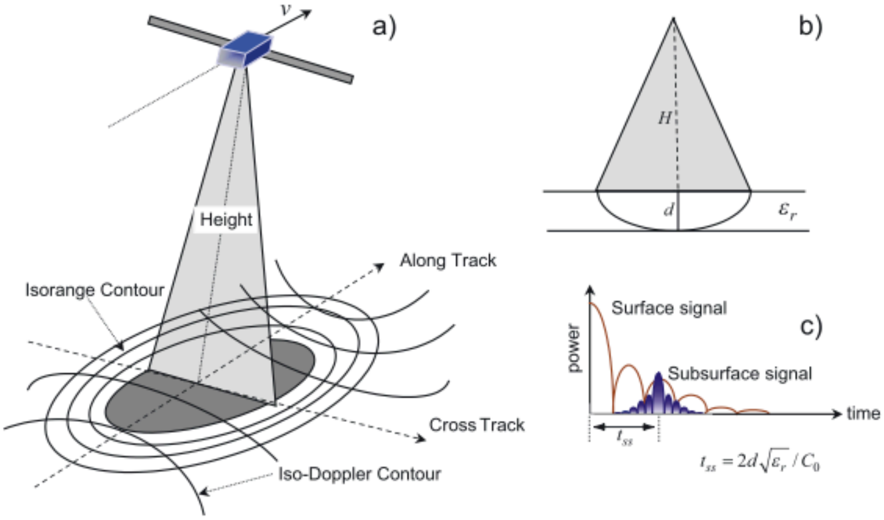

Fig.2.16 Principle of operation of SHARAD sounder.

A two dimensional picture (called radargram) is so built up in one direction thanks to the time delay and in orthogonal direction by spacecraft motion along orbit track. (Fig.2.15)

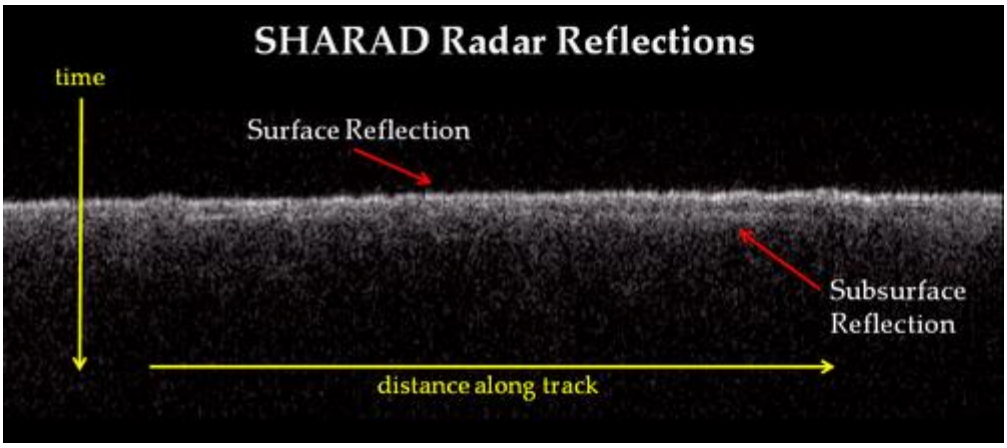

Fig.2.17 SHARAD 2D image (or radargram)

The instrument operates with 20MHz center frequency and a 10MHz bandwidth., which translates to a vertical resolution of 15m in free space and round trip and $15/\sqrt{\varepsilon}$ m in a medium with relative permittivity ε. Horizontal surface resolution depends on surface roughness characteristics, but for most Martian surface the cross-track footprint is 3-

6 km while the along-track, achieved thanks to a synthetic aperture processing, is 0.3-1 km. The returned signal is recorded as a time series of complex-valued voltages.

Regarding the PRF it is important to underline that its value cannot be only selected on the basis of swath dimension. An incorrect PRF selection may causes performance degradation if it's too lower or, if it's too much higher, undesired increase of computational power demand on board and *generates high* data volume that needs to be transmitted *to the* ground station. For this reason nominal PRF is about 700 Hz, twice the maximum Doppler spectrum, allowing for coherent integration of pulses on-board. Except for on-board pre-summing, all data processing are performed on-ground. [23]

Ground processing of SHARAD data involves the following steps:

. Decompression and Pre-Summing

. Range Processing

. Azimuth Processing

. Calibration

. Ionosphere Correction

. Time Alignment of Echoes

2.5 MARSIS Data Processing

2.5.1 Range and Azimuth Data Processing

The range processing consists in a filter that performs the cross-correlation of the transmitted waveform with the received echo. After the ADC conversion, the digital signal is filtered to obtain the components in phase(I) and in-quadrature (Q) and the resulting baseband analytical signal. The conversion to baseband can be represented as in the follow scheme I / Q type:

$$\begin{cases} I = \cos\left[\pi K\left(t - t_0\right)^2 - 2\pi f_p t_0\right] \\ Q = \sin\left[\pi K\left(t - t_0\right)^2 - 2\pi f_p t_0\right] \end{cases} \longrightarrow X = I + jQ = \exp\left\{j\left[\pi K\left(t - t_0\right)^2 - 2\pi f_p t_0\right]\right\} \quad (2.1)$$

The analytical signal is represented by the I and Q components together, expressed as:

$$t_0 = \frac{2}{c}R \longrightarrow X = \exp\left\{j\left[\pi K\left(t - \frac{2}{c}R\right)^2 - \frac{4\pi}{\lambda}R\right]\right\} = \mathrm{e}^{j\pi K\left(t-\frac{2}{c}R\right)^2} e^{-j\frac{4\pi}{\lambda}R} \quad (2.2)$$

where K=B/T=1MHz/250usec = 4 MHz/usec.

Instead, in the range direction the signal can be described as follows:

$$x_{rx}\left(t\right) = \exp\left[j\pi K\left(t - t_0\right)^2\right] rect_T\left(t - t_0\right) \quad (2.3)$$

The received signal is than range compressed by convolving it with a reference function. Since a time domain convolution correspond to a product in the frequancy domain, we can express the output range as:

$$R_x(t) = \int_{-\infty}^{+\infty} x_{rx}(\tau)\, x^*(\tau - t)\, d\tau = \int_{-\infty}^{+\infty} e^{+j\pi K(\tau - t_0)^2}\, rect_T(\tau - t_0)\, e^{-j\pi K(\tau - t)^2}\, rect_T(\tau - t)\, d\tau$$

$$\tau' = \tau - t_0 \longrightarrow R_x(t) = T\,\frac{\sin\left[\pi B(t - t_0)\left(1 - \frac{|t - t_0|}{T}\right)\right]}{\pi B(t - t_0)} \approx T \sin c\left[\pi B(t - t_0)\right] \qquad (2.4)$$

The waveform described in (2.4) is a sinc function, which has a width equal to T and with the first zero in 1/B, which means that range resolution is related to the pulse bandwidth.

Because the surface reflection can be very strong, secondary sinc lobes can mask the subsurface weak signals which are delayed several microseconds respect to the first surface return. To overcome this limitation, we can multiplying the received signal for some window function. Every window has its features in terms of: Level of secondary lobes, Loss in SNR and resolution.

So the choice of the window is a trade-off between the gain obtained in the sidelobes suppression and the consequent loss in terms of SNR and range resolution.

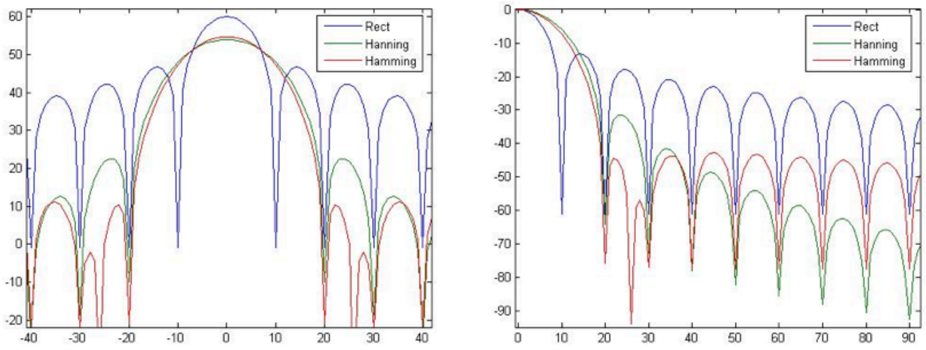

Fig 2.3 Side lobes level after weighting function

In general the azimuth processing can be coherent or incoherent, the first one is performed to reduce speckle and for application in which an improvement in SNR is required, while the coherent processing is often used for radar imaging (i.e. SAR), by integrating coherently the scatters returns received while the antenna is in we can create a synthetic array in the azimuth direction with a longer dimension antenna respect to the real one which commonly is a dipole.

For sounders radar, just like MARSIS, the primary objective is not to obtain a better azimuth resolution, but to reduce the surface clutter signals which can decrease the subsurface sounding detection. It should be noted that the scenarios encountered in the case of sounder may differ from those of a side looking SAR, therefore the Doppler processing should be properly implemented by taking into account the refractive index sounded medium, in order to get a better subsurface focalization.

For sounders as MARSIS or SHARAD where low frequencies are adopted and the spacecraft altitude is several times respect to the penetration depth, the classical SAR processing can be implemented without loose focusing performance.

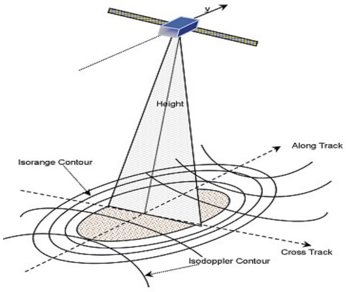

DOPPLER SIGNAL

For each PRI (Pulse repetition Interval) the radar transmits and receives signals which are stored in a matrix. Repeating the process the whole matrix will be filled, it has on the two dimensions two different times scale: on the rows is the range time (or fast time in relation to signal speed c, and is sampled at step 1/fs) on the columns is the azimuth time (or slow time, in relation to the speed V of the platform, and is sampled at step 1/PRF).

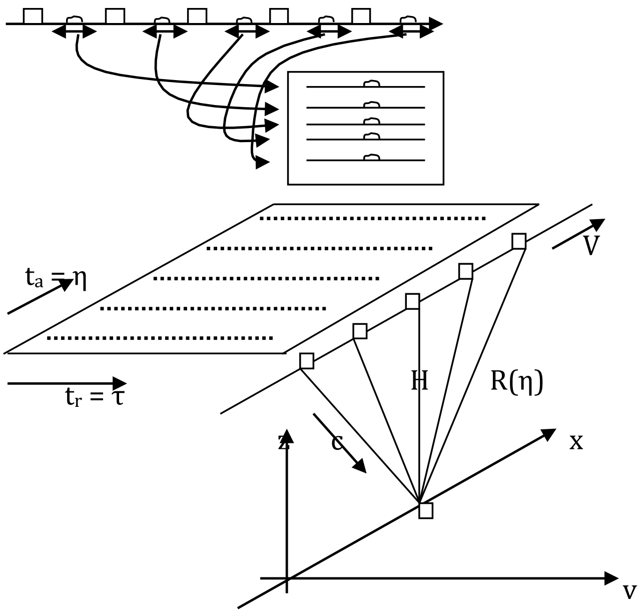

In the rows matrix, the sample time between two data elements is 1/fS, while the total number of elements on a line is equal to the duration of the receive window Trx multiplied by fs. In the column the sample time between two elements is 1/PRF, while the total number of elements of a column is equal to the azimuth observation multiplied by PRF.

Here following, we will refer the different axes of the fast time and slow time with the Greek letters τ and η, and the relative magnitudes will be denoted by the subscript "r" and "a".

The point scattered signal recorded into the matrix is therefore a two dimensional signal:

$$x(\tau,\eta) = \mathrm{e}^{j\pi K_r\left[\tau-\frac{2}{c}R(\eta)\right]^2} e^{-j\frac{4\pi}{\lambda}R(\eta)} rect_{T_r}\left[\tau-\frac{2}{c}R(\eta)\right] rect_{T_a}(\eta-\eta_0) \tag{2.6}$$

Explicit the relation between η and R the range equation is obtained:

$$R(x) = \sqrt{H^2+(x-x_0)^2} \tag{2.7}$$

Considering for a first analysis a uniform motion of the platform, the coordinate x is equal to the speed of the instrument multiplied by the azimuth time, then:

$$R(\eta) = \sqrt{H^2+(V\eta-V\eta_0)^2} = \sqrt{H^2+V^2(\eta-\eta_0)^2} \cong H+\frac{V^2(\eta-\eta_0)^2}{2H} \tag{2.8}$$

The range equation is approximated by following the development in Taylor series truncated at second term. By inserting this relation in the second exponential in (2.11) we get:

$$e^{-j\frac{4\pi}{\lambda}R(\eta)} = e^{-j\frac{4\pi}{\lambda}\left[H+\frac{V^2(\eta-\eta_0)^2}{2H}\right]} = e^{-j\frac{4\pi}{\lambda}H} e^{-j\pi\frac{2V^2}{\lambda H}(\eta-\eta_0)^2} = e^{-j\phi_0} e^{-j\pi K_a(\eta-\eta_0)^2} \tag{2.9}$$

So the data stored automatically forms a signal with parabolic phase in the direction of azimuth (Doppler chirp). The following describes the parameters of the two chirp signals within the two-dimensional matrix:

$$\begin{cases} \mathrm{e}^{j\pi K_r(\tau-\tau_0)^2} rect_{T_r}(\tau-\tau_0) \\ e^{-j\pi K_a(\eta-\eta_0)^2} rect_{T_a}(\eta-\eta_0) \end{cases} \rightarrow \begin{cases} \tau_0 = \dfrac{R(\eta)}{c/2} \\ \eta_0 = \dfrac{x_0}{V} \end{cases} ; \begin{cases} K_r = \dfrac{B_r}{T_r} \\ K_a = \dfrac{B_a}{T_a} = \dfrac{2V^2}{\lambda H} \end{cases} \tag{2.10}$$

As for the chirp in range we can think to process the waveform to obtain the desired resolution with a suitable selection of the azimuth integration period. The result of the compression matched filter in range and azimuth will be:

$$y(\tau,\eta) \cong T_r T_a \sin c\left[\pi B_r\left(\tau-\tau_0\right)\right] \sin c\left[\pi B_a\left(\eta-\eta_0\right)\right] \rightarrow \begin{cases} r_r = \dfrac{c/2}{B_r} \\ r_a = \dfrac{V}{B_a} \end{cases}$$

(2.11)

2.5.2 Unfocused Processing

The Fast Fourier Transform filters width is equal to the inverse of the observation time in the dimension on which the transformation is done and corresponds to the frequency resolution of the instrument (two targets at the same filters cannot be discriminated at least in frequency) . When the observation time is small enough, the width of each filter is large and can hold all the Doppler history of a target.

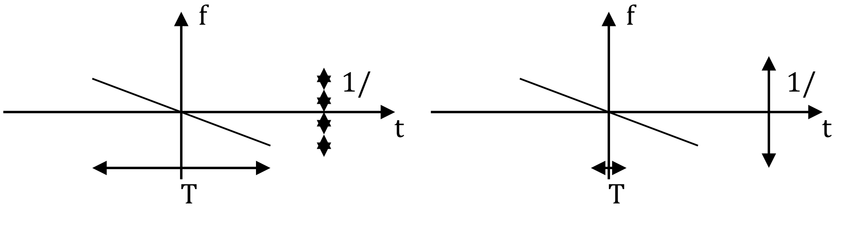

This is true when we impose the condition that the inverse of the integration time is smaller than the azimuth of the target band.

The maximum length for a synthetic unfocused SAR is equal to:

$$L_s = VT_a = V\sqrt{\frac{1}{K_a}} = V\sqrt{\frac{H\lambda}{2V^2}} = \sqrt{\frac{H\lambda}{2}} \qquad (2.12)$$

And the maximum resolution achieved is:

$$r_a = \frac{H\lambda}{2L_s} = \frac{H\lambda}{2\sqrt{\frac{H\lambda}{2}}} = \sqrt{\frac{H\lambda}{2}} \qquad (2.13)$$

The maximum resolution of an unfocused SAR correspond to the maximum length for a synthetic unfocused aperture.

2.6 SHARAD Data Processing

The raw science data produced by SHARAD are typical coherent radar data (i.e. samples of signal voltage and phase vs time of the received data signals) with a simple coherent pre-summing performed on-board. [24] When pre-summing N is selected, the samples from N sequential pulse repetition intervals (PRIs) are summed sample-by-sample. After that data samples are down-linked at either 8-bit, 6-bit or 4-bit resolutions. The collected data is compressed to reduce the amount of memory required, packaged and then sent to the ground, where all operations and the whole chain of processing (range and azimuth compression) necessary to obtain the Radar images are executed through different software tools installed at the operational center of the instrument. During this coherent pre-summing operation, SHARAD produces housekeeping telemetry to enable ground monitoring of instrument operations. The MRO flight software subsequently packetizes all the SHARAD data, and send it to the ground. The SHARAD products received on the ground will thus be a mix of science and instrument engineering health data, along with housekeeping data associated with telemetry products. [23]

In the SHOC, SHarad Operational Center, data processing software is divided in three categories: Instrument Monitoring software which consists in packet de-formatting, instrument health assessments and instrument sequence verification. Quick look software which gives a rapid evaluation of the scientific performance and Science Processing software which contains ancillary data processing necessary to understand the SHARAD data, doppler and range informations plus the reconstructed ground tracks and using Mars Orbiter Laser Altimeter (MOLA) topography data for the identification of possible clutter features.

Data, once tested checking their integrity and formatted according to the PSD standard (Planetary Data System) became Level 1A products, also known as EDR (Experiment Data Record). Experiment Data Record contains the data acquired by SHARAD with all auxiliary information necessary to place the data in space and time. Each EDR is an aggregation of SHARAD data blocks produced through the onboard processing of one or more received echoes, which are collected using the same operation mode, instrument status and onboard processing scheme. The fact that unprocessed echoes do not show any indication of subsurface interfaces make this EDR data products not so useful for scientific community. (Fig. 2.18a) [23]

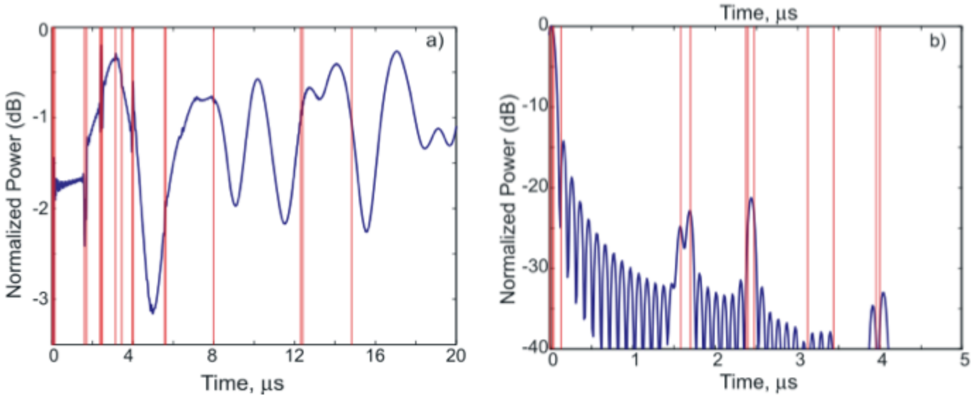

Fig.2.18 Simulation of SHARAD EDR data (a) and SHARAD RDR data (b).

Level 1B data, or RDR, will consist of received echoes that have been Doppler filtered, range compressed and has been included in the data the necessary informations on space and time localization. For achieve desired resolution in azimuth, Level 1B processor performs an estimation of the Doppler shift based on planet maps and on data collected from M.O.L.A. and then uses the Chirp Scaling algorithm (see Fig.2.19). In this way processed echoes show structured of the Martian subsurface that make RDRs data products more interesting then EDRs one. (Fig. 2.18b) As shown in Fig.2.16 blue plots represents the power received by the instrument as function of time and vertical red lines mark instants in which a subsurface echoes back towards to radar. As we can see, in a) peaks coming from subsurface are not visible instead in b) peaks corresponding to individual subsurface reflections are successfully detected while if layers are too close or too deep peaks are not discernable. [23][24]

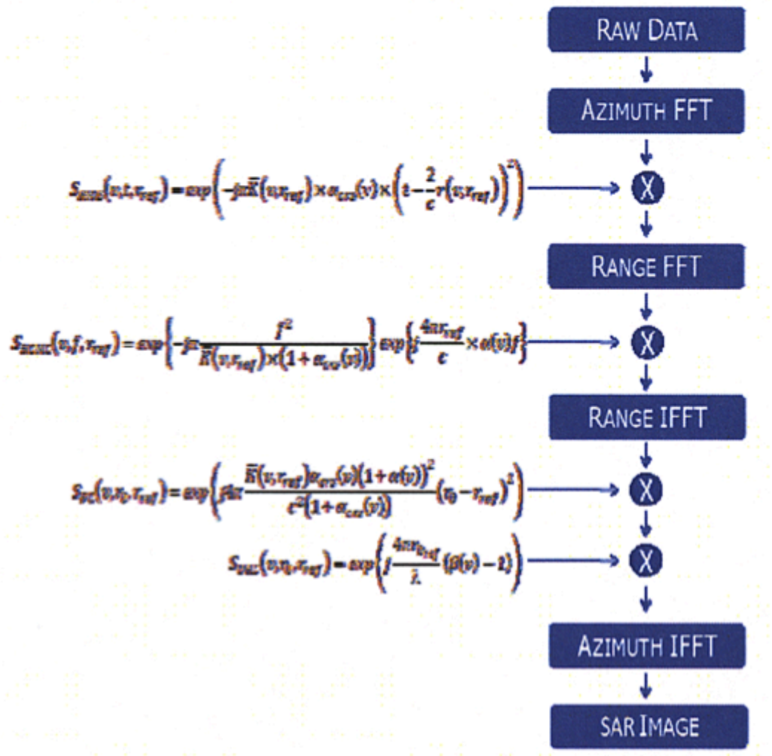

Fig.2.19 SHARAD chirp scaling compression algorithm

Chapter 3

Planetary Exploration on Saturn

3.1 The Cassini Mission

Saturn is the second most massive planet in the Solar System, formed more than four billion years ago and offers a treasure of opportunities for exploration and discovery. The gas giant planet has a huge magnetosphere and a stormy atmosphere with fast winds that can reach speeds of 1.800 kilometers per hour near its equator. These super-fast winds combined with heat rising from within the planet's interior, cause the yellow and gold bands visible in its atmosphere. Saturn has the most extensive and complex ring system, extending from 7,000 km (4,300 mi) to 80,000 km (50,000 mi) away from Saturn's equator consist of countless small particles, ranging from µm to m in size [37]. The dense main rings extend from 7,000 km to 80,000 km away from Saturn's equator. With an estimated local thickness of as little as 10 m and as much as 1 km [38], they are composed of 99% pure water-ice with impurities that may include tholins or silicates [39].

The larger moon of Saturn Titan is mysterious too. Biggest than Mercury and Pluto, Titan is of particular interest to scientists because it is one of the few moons in the solar system with its own dense atmosphere: the moon is cloaked in a thick, smog-like haze composed in the stratosphere of nitrogen (98.4%) with the remaining 1.6% composed of methane (1.4%) and hydrogen (0.1-0.2%) [40] (see Fig. 3.1). In addition to Titan, Saturn has many smaller icy satellites, 62 with confirmed orbits, 53 of which have names but only 13 of them have diameters larger than 50 kilometers [41]. Saturn, its moons and its awesome rings sit inside the enormous cavity in the solar wind created by the planet’s strong magnetic field. The field rotates with the planet, is filled with plasmas originating from both the planet and its moons. The interaction between Saturn's magnetosphere and the solar wind generates bright oval aurorae around the planet's poles observed in visible, near-infrared and ultraviolet light [42]. Saturn’s magnetosphere is extensive and maintains dynamic interfaces with both the solar wind and with Titan’s atmosphere.

The Cassini-Huygens mission was an international collaboration between three space agencies. Seventeen nations contributed to building the spacecraft. The orbiter, supplied by NASA, is named like Jean-Dominique Cassini, who discovered the satellites Iapetus, Rhea, Dione and Tethys, as well as ring features such as the Cassini division, in the 1671-1684. The Titan probe, supplied by European Space Agency (ESA), is named like the 17th Dutch astronomer Christiaan Huygens, who first discovered Saturn’s largest satellite. The Italian Space Agency (ASI), provided hardware systems for the obiter spacecraft as well as the Cassini’s high-gain communication antenna. The Cassini spacecraft was the first to explore the Saturn system of rings and moons from orbit. After a 6.7-year Venus-Venus-Earth-Jupiter Gravity Assist (VVEJGA) trajectory Cassini entered Saturn’s orbit in July of 2004 and immediately began sending intriguing images and data. For this reason on April 15, 2008, *Cassini* received funding for a 27-month extended mission consisted of 60 more orbits of Saturn, with 21 more close Titan flybys, seven of Enceladus, six of Mimas, eight of Tethys, and one targeted flyby each of Dione, Rhea, and Helene.

The extended mission began in the began on July 1, 2008, and was renamed the Cassini Equinox Mission as the mission coincided with Saturn's equinox. The Huygens Probe dove into Titan's thick atmosphere in January 2005 and after a two-and-a-half-hour descent landed on solid ground. Instruments on board collected information about the atmosphere's chemical composition and the clouds surrounding Titan. The data were radioed to the Cassini orbiter, which then relayed the data to Earth. On November 29, 2016, the spacecraft performed a Titan flyby that took it to the gateway of F-ring orbits. This was the start of the Grand Finale phase involved a series of close Saturn passes, approaching within the rings and culminating in an entry into Saturn's atmosphere on September 15, 2017 and its impact with the planet [43]. The sophisticated instruments on both spacecrafts provided scientists with vital data and the best views ever of this mysterious, vast region of our solar system.

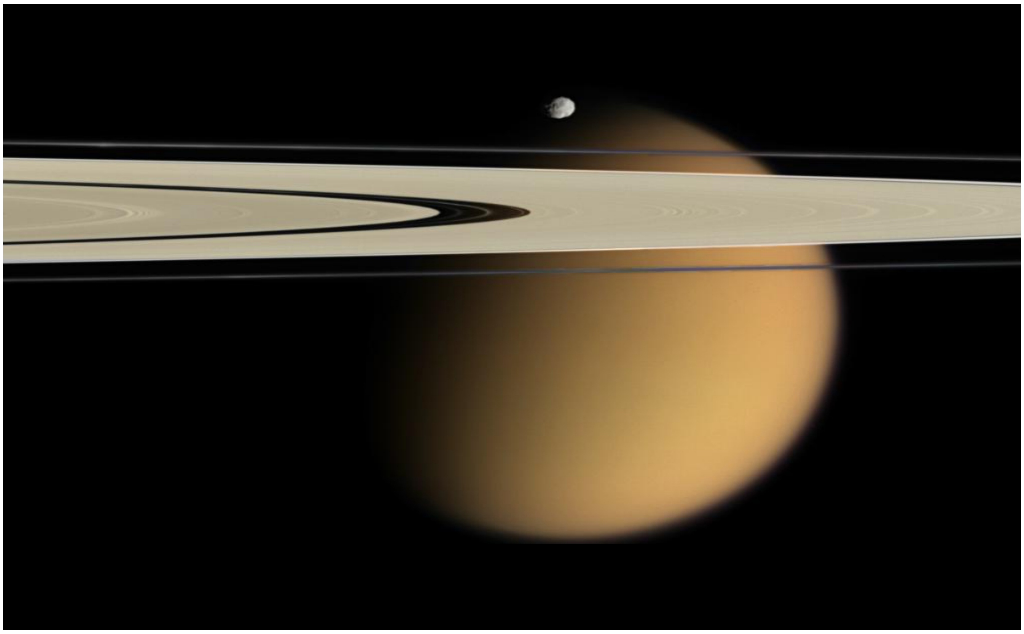

Fig. 3.1 *Cassini* image of Titan, behind Epimetheus and the rings

3.2 Cassini-Huygens: Instrument onboard the orbiter

[44] The Cassini orbiter and the Huygens probe were equipped with a set of sophisticated instruments and cameras able to collect images in many varying conditions and light spectra; from visible light to the infrared. Twelve science instruments were mounted onboard the Cassini spacecraft and each instrument was designed to carry out sophisticated scientific studies of Saturn, from collecting data in multiple regions of the electromagnetic spectrum, to studying dust particles, to characterizing Saturn's plasma environment and magnetosphere. Cassini was capable of making a wide range of in situ and remote-sensing observations.

Science investigations can be divided into three different types:

- Optical Remote Sensing.

The instruments involved are:

1. Composite Infrared Spectrometer (CIRS): it consists of dual interferometers that measure infrared emissions coming from atmospheres, rings, and surfaces over wavelengths from 7 to 1000 micrometers (1400 to 10 cm-1) to determine their composition and temperatures. It mapped the atmosphere of Saturn in three dimensions to determine temperature and pressure profiles with altitude, gas composition, and the distribution of aerosols and clouds. It also measured thermal characteristics and the composition of satellite surfaces and rings.
2. Imaging Science Subsystem (ISS): is a remote sensing instrument that captures most images in the visible light but also infra-red images and ultraviolet images. it consists of a wide angle camera (WAC), with angular resolution of 60 microradians per pixel, and a narrow angle camera (NAC), with angular resolution of 6.0 microradians per pixel.

3. Ultraviolet Imaging Spectrograph (UVIS): the instrument measures the views in ultra-violet light. Designed to measure ultraviolet light over wavelengths from 55.8 to 190 nm, this instrument is also a tool to help determine the composition, distribution, aerosol particle content and temperatures of their atmospheres. It is particularly adept at determining the composition of gases. Spatial observations take a wide-by-narrow view, only one pixel tall and 64 pixels across. The spectral dimension is 1,024 pixels per spatial pixel. Also, it can take many images that create movies of the ways in which this material is moved around by other forces.
4. Visual and Infrared Mapping Spectrometer (VIMS): it had a pair of imaging grating spectrometers designed to measure reflected and emitted radiation over wavelengths from 350 to 5100 nm, to help determine their compositions, temperatures and structures and to learn about the composition of moon surfaces, rings and the atmosphere of Saturn and Titan.

- Fields, Particles and Waves

The instruments involved are:

1. Cassini Plasma Spectrometer (CAPS): it has measured the flux of ions as a function of mass per charge, and the flux of ions and electrons as a function of energy per charge and angle of arrival relative to CAPS.
2. Cosmic Dust Analyzer (CDA): it was intended to provide direct observations of particulate matter in the Saturnian system, to investigate the physical, chemical, and dynamical properties of these particles, and to study their interactions with the rings, icy satellites, and magnetosphere of Saturn.
3. Ion and Natural Mass Spectrometer (INMS): intended to measure positive ion and neutral species composition and structure in the

upper atmosphere of Titan and magnetosphere of Saturn, and to measure the positive ion and neutral environments of Saturn’s icy satellites and rings.

4. Dual Technique Magnetometer (MAG): the primary objective was to determine the planetary magnetic fields and the dynamic interactions in the planetary environment.
5. Magnetospheric Imaging Instrument (MIMI): designed to measure the composition, charge state and energy distribution of energetic ions and electrons, detect fast neutral species, and conduct remote imaging of the Saturn’s magnetosphere.
6. Radio and Plasma Wave Science (RPWS): the major functions were to measure the electric and magnetic fields and electron density and temperature in the interplanetary medium and planetary magnetospheres.

- Microwave Remote Sensing

The instruments involved are:

1. Cassini Radar (RADAR): The onboard radar was an active and passive sensing instrument with a five-beam Ku-band antenna feed assembly associated with the spacecraft high gain antenna to direct radar transmissions toward targets, and to capture blackbody radiation and reflected radar signals from targets.

2. Cassini’s Radio Science Subsystem (RSS): intended to study the compositions, pressures and temperatures of the atmospheres and ionospheres of Saturn and Titan; the radial structure of Saturn’s rings and the particle size distribution within the rings, and planet-satellite masses, gravity fields and ephemerides within the Saturn system. RSS is split in two parts: one resides on the spacecraft, the other at stations equipped to receive very stable radio signals at each of the three Deep Space Network complexes.

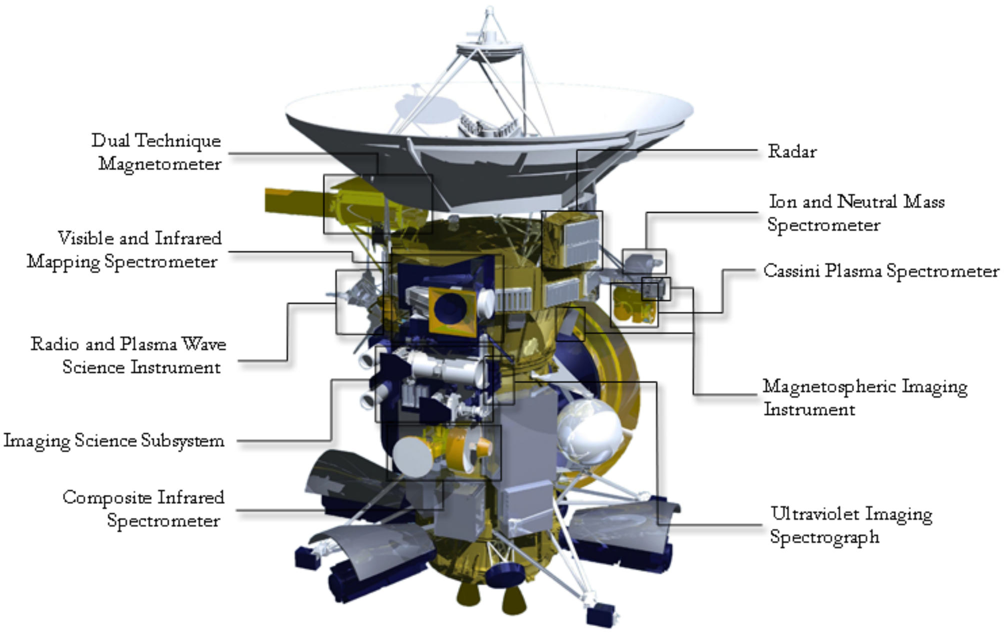

Fig. 3.2 *Cassini* Spacecraft Instruments

3.3 The Cassini Radar

Italian contribution provided Cassini with the core of the telecommunication system: the High-Gain Antenna (see Fig.3.2). At the top of the Cassini stack is the large, four-meter-diameter High-Gain Antenna (HGA) and two low-gain antennas (LGA1 and LGA2). HGA was also used for radio and radar experiments and it was used for receiving signals from Huygens.

The Cassini RADAR was a multimode instrument working in Ku-band (13.78 GHz). It used the five beam antenna feed assembly associated with the spacecraft high gain antenna to transmit and receive electromagnetic radiation according to different possible operative modes: Scatterometer mode, Imaging mode, Altimeter mode and Radiometer mode. Each mode allows for the collection of different types of data, from straightforward imaging to 3-dimensional modeling to passive collection of information, such as simply recording the energy emanating from a planet's surface.

RADAR scientific objectives were:

- to determine whether liquid surfaces exist on Titan, and, if so, to determine their distribution;
- to investigate the geologic features and topography of the solid surface of Titan;
- to acquire data on non-Titan targets (rings, icy satellites) as conditions permit.

In imaging mode the radar works as Synthetic Aperture Radar (SAR), that is an active mode able to provide a microwave image of the observed target with a relatively high spatial resolution. SAR images is the sharpest that Cassini can achieve on the surface of Titan, with 350 to 1700 meter horizontal resolution (see Fig. 3.3). To collect SAR data, Cassini looks off to one side of the ground track as it flies by, instead of straight down as it does for the altimetric measurements. The radio antenna chirps a signal at the planet and then listens for the echo and measures the delay time, the time between the chirp and the echo. The echo is not exactly like the original chirped signal. The echo is stretched out over time, because the signal returns first from the ground closest to Cassini, and later from the ground farther from Cassini. Also, the echo is Doppler shifted to slightly different wavelengths depending upon whether the echo comes from the ground ahead of the spacecraft along its track, which appears to be moving toward Cassini, shifting the wavelength shorter, or from the ground behind the spacecraft, which appears to be retreating and thus has a longer-wavelength shift. By processing the data into a map of echo strength in delay-Doppler space it can be seen how the strength of the signal varies relative to the spacecraft’s position. This processing must be performed for each chirping signal produced by the spacecraft. SAR processing depends

Fig. 3.3 Titan RADAR SAR Swaths.

on incredibly accurate knowledge of the speed and position of the spacecraft relative to the surface that it is mapping. Instead of the inherent albedo, or brightness of the surface that is seen in optical images, SAR images show the strength of a reflected radio signal. Variation in the strength of a reflected radio signal can result from three main factors: slope, roughness, and dielectric constant.

Radar altimetry similarly involves bouncing microwave pulses off the surface of the target body and measuring the time it takes the echo to return to the spacecraft. In this case, however, the goal is not be to create visual images but rather to obtain numerical data on the precise altitude of the surface features of Titan. In this mode, Cassini acquires profiles with 24 to 27 kilometer (15 to 18 mile) horizontal resolution and 90 to 150 meter (300 to 500 foot) vertical resolution.

In radiometer mode the radar operates as a passive instrument just recording the electromagnetic energy spontaneously radiated from the surface of Titan. This information stores the amount of latent heat in Titan's atmosphere, a factor that has an important impact on the precision of the other active radar measurements. Radiometry roughly correlates with temperature, and radiometry results are often described as brightness temperatures of surfaces. In this mode, Cassini can create maps of Titan with 7 to 310 kilometer pixel resolution. When it turns in the active mode, RADAR acts as a scatterometer. That is, it bounces pulses off Titan's surface and then measure the intensity of the energy returning. This returning energy or backscatter, is always less than the original pulse, because surface features inevitably reflect the pulse in more than one direction. From the backscatter measurements, scientists can infer the composition of the surface of Titan.

As described in details by Lorenz et al. [45], on a RADAR dedicated flyby, observations begin several hours before the closest approach, at a range of around 100,000 km and a precise sequence of observations is performed. After a warm-up period to stabilize the noise diode reference and cold-sky measurements, the beam is pointed at Titan in the radiometric mode. At a range of 100,000 km the beam footprint is around 500 km across (a resolution of 1/10th of Titan's disk). The beam is moved in a spiral or raster pattern to cover the whole disk. Within 25,000 km range (about 1 hour before the closest approach) active scatterometer measurements start. Radiometer observations can continue, although the incidence angles may be optimized for scatterometry, rather than the ride along radiometry.

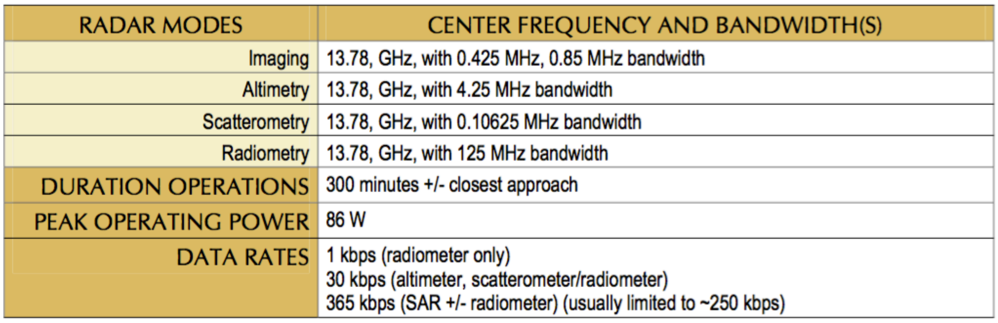

RADAR MODES	CENTER FREQUENCY AND BANDWIDTH(S)
Imaging	13.78, GHz, with 0.425 MHz, 0.85 MHz bandwidth
Altimetry	13.78, GHz, with 4.25 MHz bandwidth
Scatterometry	13.78, GHz, with 0.10625 MHz bandwidth
Radiometry	13.78, GHz, with 125 MHz bandwidth
DURATION OPERATIONS	300 minutes +/- closest approach
PEAK OPERATING POWER	86 W
DATA RATES	1 kbps (radiometer only) 30 kbps (altimeter, scatterometer/radiometer) 365 kbps (SAR +/- radiometer) (usually limited to ~250 kbps)

Table 1. Instrument Description

Within 10,000 km, altimeter observations are more useful, and the spacecraft is held nadir-pointing. Again, simultaneous radiometry is performed. The simultaneous radiometry and altimetry are of partic- ular meteorological interest, since elevated terrain should be cooler by about 1 K/km due to radiative- convective temperature profile of Titan's atmosphere. Also in this case we have a high resolution altimeter mode between 4000 and 9000 km where the transmitted bandwidth is 4.25 MHz and the altimeter foot- print is pulsewidth limited and is 24 to 27 km wide. The low resolution altimeter mode is planned between 9000 and 22.500 km and in this case the radar actually works as a scatterometer transmitting a wave- form with a bandwidth of about 106 KHz to measure the average surface reflectivity over a beamwidth footprint up to 100 km wide ([13]).

The imaging mode is selected while the spacecraft altitude passes from 4000 km to its minimum value (1000 km from the surface of Titan). In particular in this time interval we have a high resolution imaging mode between 1000 and 1500 km where the radar image pixel is 380 (azimuth) × 600 (range) meters wide and a low resolution imaging mode between 1500 and 4000 km where the radar image pixel is 600 × 2500 m wide. In any case the number of looks integrated to improve the radiometric quality of the image is ≥ 3, the incidence angle is included in the range $10^{\circ} \div 30^{\circ}$ and a quite simple unfocused processing algorithm can be used to obtain the radar images from the raw radar data.

Outbound, the altimeter, scatterometer and radiometry observations are repeated in reverse order (see Fig. 3.4). Titan' surface has been essentially covered completely at some incidence and polarization, with some repeated coverage to look for seasonal change and exploit multiple incidence angles.

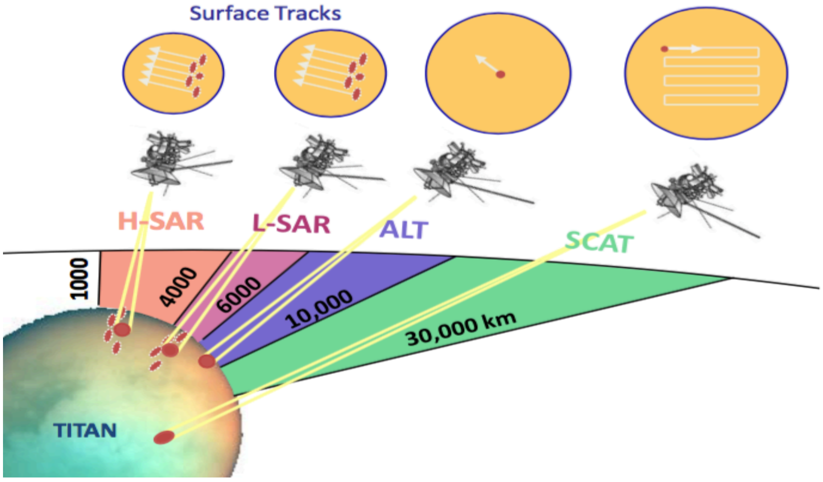

Fig. 3.4 Cassini Radar Operation Modes

3.4 Cassini Data Processing (CASPAD)

[46] Cassini altimetry data processing is performed in the framework of PAD facility, that contains hardware and software tools necessary to receive and elaborate the instrument raw data sets, generate and archive the science data products. The system is able to manage BODP (Burst Ordered Data Products) files supplied by JPL compliant to PDS (Planetary Data System) standards.

The physical architecture of the PAD System is composed by several software components running on two operating system platforms. The first is a server that hosts the local data archive and it is supported by a Linux operating system. The local archive is accessed as a network drive by the data processing subsystem. The second is a client platform where all data processing algorithms are working under Windows® XP Professional operating system.

The core of data processing is represented by a set of algorithms and tools developed in a Matlab® environment. Each tool is provided with a userfriendly graphical interface (GUI), which allows users to exploit all implemented functionalities. The architectural design of PAD tools is shown in Fig. 3.5, where the following main logical components can be identified:

PAD Framework

The main functionality of the PAD Framework software is to give users a global vision of the status of all the operations that can be made on the BODP files within the Cassini Radar PAD. It provides easy access to all system functionalities. Users can select the flyby to operate and start any operation available for the processing of telemetry files.

PAD File Manager

The PAD File Manager is the software component that allows users to import the PDS telemetry files into the Local Archive, and to deliver the output ABDR products to the scientific community. The LBDR data retrieval can be executed through the JPL secure HTTPS site, or from any file system location indicated by the user. The delivery functionality can publish the ABDR file on a public FTP repository and/or copy it to a writable portable transfer media.

PAD Data Publisher

The PAD Data Publisher is the software component containing all the commands and the methods that allow users to forward the ABDR files to the Cassini Ground System repository located at JPL. The produced ABDR file is not physically sent nor moved to the Cassini Ground System repository located at JPL. Once the PAD File Manager has published the ABDR files to the public FTP repository, the scientific community receives an e-mail notification to access the password protected repository in order to download the new available file.

ABDR Production Tool

The off-line ABDR Production Tool (PT) retrieves the input LBDR files by managing a list of LBDR files locally stored, allowing user to select the input file. After interactive selection of the LBDR file to be processed, the tool proposes to start the creation of subsets of the input LBDR product (intermediate PT Files) each containing only data records pertinent to one of the active Cassini Radar operational modes, i.e. Altimeter, SAR and Scatterometer mode. These files are created for internal use and stored into the local archive in both binary and ASCII format, in order to be accessed by SLT. The PT allows user to perform the generation of the ABDR product starting from the selected LBDR file. Moreover, user is allowed to interactively modify selected keywords into ABDR PDS label.

An ABDR file is produced which contains records for only the two periods (one inbound, one outbound) in which the radar is in altimeter mode, by filling in automatically all the appropriate data fields in the Science Data Segment with the values obtained from SLT processing, and by filling the end of each record in the LBDR file with the values resulting from range compression of sampled echoes data counts (i.e. the altimeter profile), starting from SLT results files. When LBDR processing is terminated, the ABDR PT stores the new file into the local archive along with a report file. Data contained into the ABDR product shall be validated by using SLT functionalities, before submission to the local file server.

Science Look Tool

The off-line Science Look Tool (SLT) performs the altimetric processing.

It is a graphical application including procedures and algorithms designed to check and simulate the performances of the Cassini Radar Altimeter through calculation, visualization and plotting of relevant parameters. The SLT uses an intermediate BODP file produced by the ABDR Production Tool, stored into the local archive, and it automatically performs range compression of sampled data.

The SLT evaluates the altimeter profile range start, altimeter profile range step and altimeter profile length required for the PT ABDR production functionality, starting from compressed data. Each compressed burst is typically constituted of 15 chirp pulses. In order to reduce the speckle, a single pulse is obtained by averaging all the received pulses within the burst. Hence, each compressed burst becomes an array containing only one averaged pulse-compressed echo. The averaged bursts are stored into internal memory as bi-dimensional arrays. The range compressed data are used to perform waveform analysis and final altitudes estimate by using different altimetry models previously implemented. In addition, the tool permits user to simulate the performances of the Cassini Radar Altimeter, thus allowing obtaining a complete analysis of ALT data from a scientific perspective. In order to infer the significant geophysical parameters describing the surface’s topography from the altimetry data, a Maximum Likelihood Estimator (MLE) has been implemented to be enclosed in the developed algorithm. The Maximum Likelihood Estimator algorithm is based on fitting averaged bursts with a theoretical model describing the Radar Impulse Response. The algorithm is able to select automatically which is the best theoretical model to be used during the processing. The selection is based on threshold criteria related to the current value of the off-nadir angle, in order to cope with the expected occurrence of near-nadir measurements along the hyperbolic trajectory followed during the flyby. All the performances have been numerically evaluated: this method ensures the best fitting of data, thus reducing the errors in heights estimation.

The SLT provides several auxiliary functionalities that allow the user to obtain the complete monitoring of both processing and results. On user request, the SLT provides 2-D or multi-plots of S/C and Radar ancillary data, processing results and algorithm configuration. All the results can be exported (i.e. printed/saved) by user. In addition, on user request, a report file in xml format is generated containing all the results produced by the SLT, e.g. relevant processing parameters, MLE procedure results, relative elevations of Titan's surface vs. along-track distance (i.e. topographic profiles), altimeter waveforms vs. range bins, ancillary data (e.g. observation geometry and orbital parameters vs. time, instrument data, etc.), surface parameters vs. along-track distance, etc. It will be used by scientists for further validation of data.

Map Tool

The off-line PAD Map Tool (MT) is a graphical application that allows users to visualize and navigate through Titan's 2D and 3D maps, finalized to the analysis of their informative content, as immediate instrument of interpretation of scientific data. The purpose of MT is the production of altimetric regional maps obtained by visualization of sub-satellite ground-tracks and overlapping of data collected along tracks to a pre-existent map of Titan, over the region illuminated by the Cassini Radar in high-resolution ALT mode, for each Titan fly-by. Hence, Titan's maps represent the final results of data processing. The realization of the altimetric map can be accomplished by referencing the radar altimetry profile with respect to the surface of Titan.

The Titan's altimetric maps are generated starting from SBDR, LBDR and BIDR data files, and from output data produced by the SLT (e.g. the topographic profile with information about the surface slope, etc.) which could be superimposed to referenced images of Titan surface in a given projection. The content of SBDR, LBDR and BIDR data files is extracted by means of a Data Production Utility, which saves all relevant information needed to produce MT datasets (map internal files) containing satellite geometry, Scatterometer, Radiometer and SAR data, which becomes then available to Map Tool for visualization.

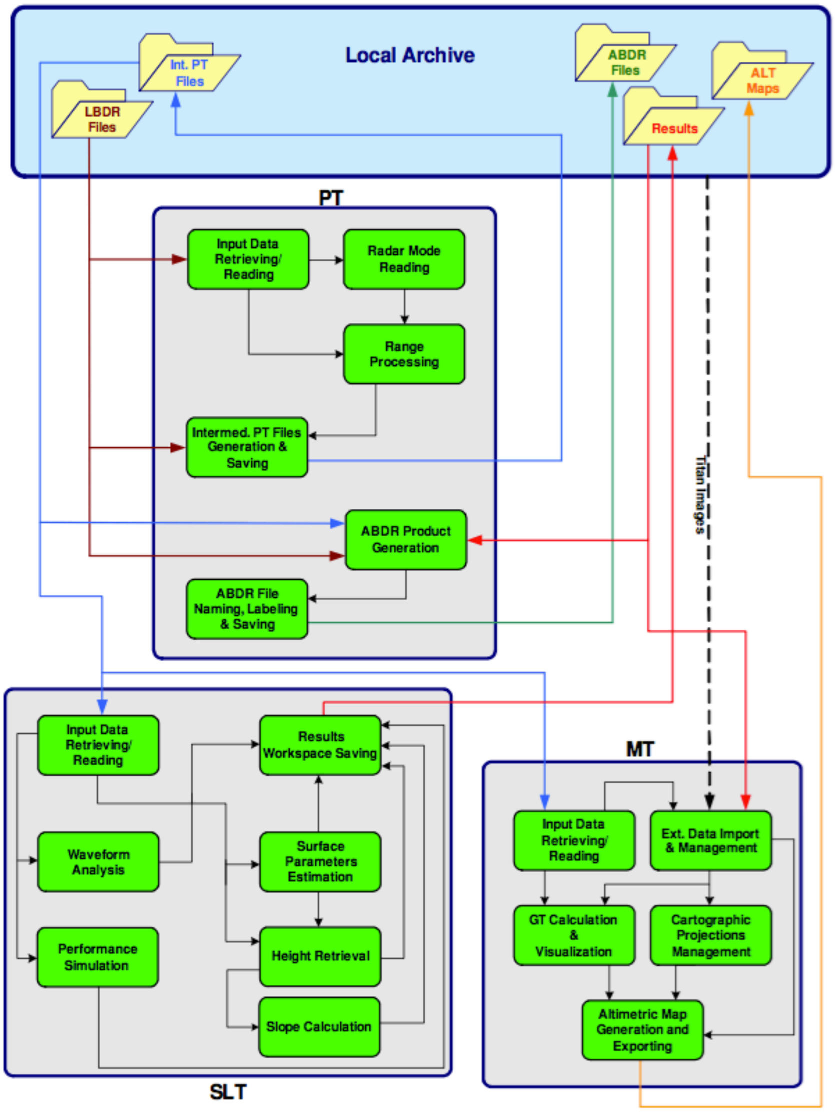

Fig. 3.5 PAD Tools Architectural Design

Chapter 4

Resolution Enhancement: Bandwidth Extrapolation Methods

4.1 Introduction

Radars are commonly used for detection, tracking and identification of targets. They are active systems that transmit electromagnetic pulses towards a target and measure the field scattered from the target at discrete frequencies and for several angles. By recording these radar measurements we can obtain the scattering response of the target as a function of spatial coordinates. The transformation of the radar scattering data into a spatial scattering response of the target is known as radar imaging. In classical radar imaging algorithms, this transformation is based on an inverse Fourier transform. In cases where the transmitted signal corresponds to a linearly frequency modulated signal (named chirp), the received signal can be sampled and using an inverse Fourier transformation is possible to yield the target's scattering intensity (phase and amplitude) as a function of range.

Since these algorithms are based on a Fourier transformation, they can have a problem with limited resolution. The resulting target's range profile in fact has a resolution which is inversely proportional to the bandwidth of the available data. High resolution images can thus be achieved by transmitting a wideband signal but at the expense of high spectrum occupancy. Unfortunately, in many practical applications, radars may have bandwidth limitations or the scattered field of the target may vary importantly with frequency that not allowing the use of large bandwidths. Thus, algorithms with improved resolution are desired for radar imaging. In radar applications, one solution consists of transmitting pulses with a large band and extrapolating the signal across a wider bandwidth using well suited data extrapolation algorithms.

Linear predictive Bandwidth Extrapolation (BWE) technique has been introduced as a means of consistent improving the resolution of the pulse compressed coherent radar data. It consists to extrapolate the bandwidth of the signal in the transform domain to enhance and sharpen the resolution of the original signal in the original domain. A way to extend bandwidth is fitting a priori model to the measured radar signal. Auto-Regressive (AR) models are commonly used for this purpose. Once the AR models have been fitted to the measured radar signal, they are employed to estimate linear prediction coefficients suitable for extrapolate radar samples out the original band. Subsequent an IFT processing of the expanded spectral signal yields to obtain recompressed pulses with a better resolution than the Conventional Fourier techniques. Bandwidth Extrapolation methods were investigated for the first time in the late 1960s, when R.T. Lacoss began studing the application of super-resolution techniques to seismic data [26]. Starting on the late 1970s the Lincoln Laboratory investigated several concepts for potential resolution improvement. These were applied for the first time to radar data by S.B.

Bowling in the 1977, who investigated the use of modern spectral-analysis methods for Doppler-processing enhancement [28] and mentioned the potential of the approach for improving range resolution. In the 1990, K.M. Cuomo investigated the Burg method for extrapolating signals and improve the range resolution of coherent radar data [29]. In using this approach, he reached remarkable results and leads to the current interest in these methods.

In this chapter fundamentals of spectral analysis methods will be presented. In particular, after a brief discussion about Conventional Fourier processing usually applied on radar data, we will focus our attention Bandwidth Extrapolation (BWE) fundamentals and on three Auto-Regressive (AR) methods: Yule-Walker, Burg and Modified Covariance. These three methods, all based on a forward- and backward-prediction error minimization have been chosen as potentially practical for radar data-analysis problems and will be employed in the following chapters where the behavior of these methods with different data sets (simulated and measured) is investigated.

4.2 Conventional Data Processing

The conventional Fourier approach which relates the autocorrelation function of a signal and its power spectrum by means of the Fourier transform has ruled the analysis of radar data until the present time. Based on this basic principle, coherent wideband radars can achieve fine range resolution by transmitting pulses with a wide frequency bandwidth. When the transmitted waveform is a linear frequency modulated wave, or chirp, the received signal after sampling can be inverse Fourier transformed to obtain the target scattering intensity (amplitude and phase) as a function of the range. Limitations in the resolution are caused by the fact that conventional pulse compression schemes are based on conventional Fourier techniques which relates properties of the compressed pulse (e.g. resolution and side-lobes levels) to the size and the shape of the spectral window function applied to the received signal.

The Fourier approach has the advantage of being elegant and robust but it often suffers of a lack of resolution due to fact that the received data record is short compared to the periodicity of the spectral component in the data. The lack of resolution can be attributed to an unrealistic assumptions regarding the nature of data outside the observation interval. It implicitly assumes that the unavailable data samples outside the window region are zero, which is not totally true in many cases. Based on this assumption, the truncated data set in the time domain can be seen as the product of a data set with infinite length and a window function with non-zero amplitude only within the observation interval. This point wise multiplication in time corresponds to convolution in the frequency domain between the true spectrum of the data set, which is the extended version of the measured one, and the spectrum of the window function.

Let’s consider a rectangular window, its spectrum has the following form:

$$W(f) = \frac{\sin(\pi f T)}{\pi f T} \tag{4.1}$$

where T is the data set length and the first zero occurs at f=1/T. For this reason, frequency components in the true spectrum spaced less than l/T are not resolved in the measured spectrum. The frequency resolution of the measured spectrum is therefore equal to l/T. The rectangular window can be also replaced by a tapering function well suited to reduce the effect of the side-lobes, the penalty for this windowing is a further loss in spectral resolution, so that spectral details of width greater than l/T are unfortunately obscured.

To better understand what said before, let’s describe a typical pulse compression scheme is the case that a linear frequency modulation (LFM) signal (i.e. chirp) is transmitted by the radar. (Fig.4.1)

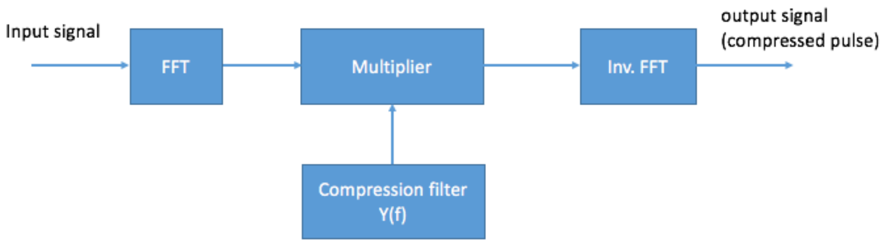

Fig. 4.1 Pulse Compression Scheme

Let’s *s(t)* be the LFM pulse in input:

$$s(t) = rect\left(\frac{t}{T}\right) e^{2\pi j(f_0 t + \frac{kt^2}{2})} \tag{4.1}$$

where the phase response *ϕ(t)* and the instantaneous frequency f_I are defined as follows:

$$\phi(t) = 2\pi\left(f_0 t + \frac{kt^2}{2}\right) \quad , \quad f_i = \frac{1}{2\pi}\cdot\frac{d\phi}{dt} = f_0 + kt \tag{4.2}$$

which means that during T seconds duration of the pulse, the frequency change linearly from $f_0 - kT/2$ to $f_0 + kT/2$.

The spectrum of this waveform is given by:

$$S(f) = \mathcal{F}\{s(t)\} = \int_{-\infty}^{\infty} s(t)\, e^{-j2\pi f t}\, dt = \int_{-T/2}^{T/2} e^{j2\pi[(f_0-f)t+\frac{kt^2}{2})}\, dt$$

the spectrum of the compressed pulse can be calculated from:

$$S_{out}(f) = S_{in}(f)\cdot Y(f) \tag{4.5}$$

where $S_{in}(f) = S(f)$ and $Y(f)$ is the transfer function of the compression filter matched to the transmitted chirp defined as follows:

$$Y(f) = e^{j\pi(f_0-f)^2/k} \tag{4.6}$$

Given the expression (4.4) and (4.5) it's more convenient find the output pulse in the time domain: $s_{out}(t)$ as the convolution between the input signal $s_{in}(t)$ and the impulsive response of the compression filter $y(t)$ obtained from the following formula:

$$y(t) = \int_{-\infty}^{\infty} Y(f)\, e^{2\pi f t}\, dt = \int_{-\infty}^{\infty} e^{j(f_0-f)^2/k}\, e^{-j2\pi f t}\, dt \tag{4.7}$$

Note that if we make a substitution $f - f_0 = u$ so $f = u - f_0$ and the integral can be solved using the following integration formula:

$$\int_{-\infty}^{\infty} e^{-\pi\beta u^2}\, e^{-j2\pi u t}\, du$$

$$= \frac{1}{\sqrt{\beta}}\cdot \exp\left(-\frac{\pi t^2}{\beta}\right) \tag{4.8}$$

comparing the equation (4.8) $y(t)$ becomes:

$$y(t) = \sqrt{\frac{jB}{T}} \cdot e^{j2\pi f_0 t} \cdot e^{-j\pi t^2 k}$$

$$= \sqrt{\frac{jB}{T}} \cdot e^{j2\pi(f_0 t - t^2 k/2)} \tag{4.9}$$

so the output signal $s_{out}(t)$ can be obtained by:

$$s_{out}(t) = \sqrt{\frac{jB}{T}} \cdot \int_{-\frac{T}{2}}^{\frac{T}{2}} e^{j2\pi(f_0\tau + \tau^2 k/2)} \cdot e^{j2\pi(f_0(t-\tau)-(t-\tau)^2 k/2)}\, d\tau =$$

$$= \sqrt{\frac{jB}{T}} \cdot e^{j2\pi(f_0\tau + t^2 k/2)} \int_{-\frac{T}{2}}^{\frac{T}{2}} e^{j2\pi kt\tau}\, d\tau \tag{4.10}$$

and using the standard integral form: $\int e^{ax}\, dx = \frac{e^{ax}}{a}$ then

$$\int_{-\frac{T}{2}}^{\frac{T}{2}} e^{j2\pi kt\tau}\, d\tau = \frac{1}{j2\pi kt}\left[e^{j2\pi kt\tau}\right]_{-T/2}^{T/2} = \frac{1}{j2\pi kt}\left[e^{j2\pi ktT/2} - e^{-j2\pi ktT/2}\right]$$

and

$$s_{out}(t) = \frac{1}{\pi kt} \cdot \sqrt{\frac{jB}{T}} \cdot \sin(\pi BT) \cdot e^{j2\pi\left(f_0 t - \frac{kt^2}{2}\right)} =$$

$$= \sqrt{BT} \cdot \sqrt{j} \cdot \frac{\sin(\pi BT)}{\pi Bt} \cdot e^{j2\pi\left(f_0 t - \frac{kt^2}{2}\right)} \tag{4.11}$$

The compressed output has the form of a *sinc* function with the 4-dB width of the main lobe equal to $\tau = 1/\mathrm{B}$. At the output of the pulse compressing stage the frequency resolution of the measured spectrum is therefore proportional to l/B where B is the radar bandwidth. The wider is the signal bandwidth the higher the resolution that the radar can achieve.

4.3 Bandwidth Extrapolation

In using of wideband radar for imaging a sufficient resolution is required in order to distinguish targets in the radar scenario. As seen before, the pulse compression schemes based on Fourier transformations deliver a resolution which is dependent to the radar bandwidth. However, in many applications we can make more realistic assumption on the deterministic properties of the received signal and use them to improve the radar resolution.

At high frequency, where the dimension of the target are typical compared to the radar wavelength the far-field backscatter modelling of radar signals can be expressed by superimposition of fields of discrete scattering centers [30]. This means that the received signal in the frequency domain is given by:

$$V(f,\theta) = \sum_i A_i(f,\theta)e^{\frac{j4\pi f R_i(\theta)}{c}} \tag{4.12}$$

where A_i is the amplitude of each scattering center and R_i is its effective range from the sensor. As shown in the formula, the total target response can be modelled as the sum of complex sinusoids where the radar frequency f is the independent variable and the frequency of each sinusoid determined by the time delay due to the distance from the sensor. By means of a Fourier transform this frequency response can be converted into a range profile (pulse compression process) characterized by peaks in correspondence to the scatter locations and with a resolution which is inversely proportional to the radar bandwidth ($\delta r = c/2B$). Since radar bandwidth is a limiting factor for range resolution, we can overcome this limitation and employee high-resolution techniques to obtain radar datasets with resolutions that classical methods lack. The aim is to lengthen the data record outside the radar bandwidth so that Fourier imaging can provide the desired resolution. Unfortunately, the extension of data record with additional measurements is often impossible in radar systems because of the fast changes with frequency of the scattering characteristics of target.

Since at the high frequency, the scattering field of a complex object consists of a superimposition of sinusoids, significant improvements in range resolution can be obtained by expanding the available radar data using an Auto-Regressive (AR) approach. Thanks the assumption on the signal nature, we can use a parametric time-series AR model of the data in order to exploits sinusoidal properties of the radar signal and make realistic assumptions on data outside the receiving window region. In this way the unknown linear prediction coefficients of the AR model are computed independently for the spectral data of each radar pulse and then used in linear prediction filters to extrapolate the received signal outside the effective radar bandwidth.

Knowing the samples of a data sequence, after linear prediction coefficients estimation, we can calculate the next sample in the scattered field data expressed by the equation (4.12). The linear prediction model for a uniformly sampled frequency spectrum given by:

$$v[n] = V(n\delta f, \theta) \tag{4.13}$$

may be expressed by defining N point sequence as:

$$v_e[n] = \begin{cases} -\sum_{i=1}^{N} a^*[i]v[n+i] & for\ n < N_1 \\ v[n-N_1] & for\ N_1 \leq n \leq N_2 \\ -\sum_{i=1}^{N} a[i]v[n-i] & for\ n \geq N_2 \end{cases} \tag{4.14}$$

where v[n] is the n^{th} element of the original data sequence, $v_e[n]$ is the n^{th} element of the extrapolated data sequence, N_1 and N_2 are the first and last indices of the extended sequence and $a[i]$ and N is the model coefficients and the model order respectively.

Numerous techniques exist for estimating coefficients of the linear-prediction model from measured data, three algorithms will be presented in the next paragraphs. The degree of improvement in resolution depends primarily on the ability to fit the measured data with The Auto-Regressive (AR) model parameters in order to estimate the best linear prediction coefficients. The linear prediction filters built with the estimated AR coefficients create new spectral samples consistent to the measured data, in this way the effective bandwidth is increased with an high resolution improvement of the recompressed pulse respect to the original one.

The typical processing steps related to the Bandwidth extrapolation (BWE) are described in [29] and illustrated in Fig. 4.2. First the radar compressed pulse in the form of amplitude and phase versus slant-range is Fourier transformed into its spectral components [I, Q]. If a window weighting function to reduce the range sidelobes was applied to the spectral data, it has to be removed before the linear prediction processing in order to avoid that the spectral components near the center frequency dominate the extrapolation process. Then a linear prediction processor based on Burg algorithm [25] is implemented. The via Burg estimated coefficients are used to generate forward and backward linear prediction synthesis filters needed to extrapolate the input spectral range data forward and backward in the frequency domain and increasing the effective bandwidth of the input pulse. For side lobe reduction, a weighting function can be re-applied to the extrapolated spectrum before apply the inverse Fourier transformation and get the recompressed pulse.

Figure 4.2 shows an input pulse 10MHz bandwidth, after bandwidth extrapolation the effective bandwidth is increased by a factor of 2 which produces an output pulse (recompressed pulse) with a resolution double than the input one.

A detailed description of these AR methods estimate coefficients and linear prediction principles can be found in the following paragraphs.

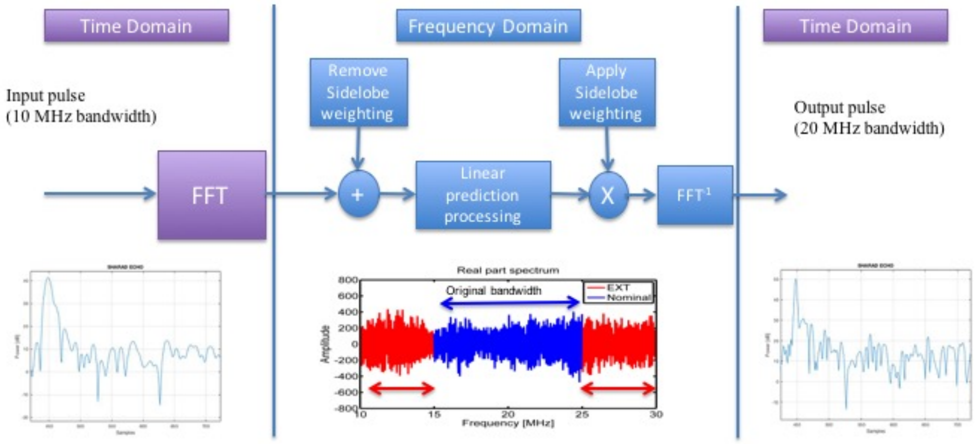

Fig. 4.2 Bandwidth Extrapolation (BWE) Scheme.

4.4 Linear Prediction: Auto-Regressive Methods

Linear prediction modelling is used in several area of applications, such as model-based spectral analysis, speech coding, speech recognition, model-based interpolation, signal restoration. In this paragraph, we introduce the theory of linear prediction modelling and consider efficient methods for the computation of predictor coefficients [30] [27].

Let's consider a continuous-time series signal $x(t)$, this signal can be sampled to obtain a discrete-time signal $x(nT)$, known as time series, where T is the sampling interval and n an integer variable. Assumed the samples of the signal can be considered as realization of a stochastic process, at time n the process is defined by the random variable $x[n]$. A linear prediction model forecasts the amplitude of $x[n]$ in the following expression:

$$\check{x}[n] = -\sum_{k=1}^{N} a[k]x[n-k] \tag{4.15}$$

where the integer variable n is the discrete time index, $\check{x}[n]$ is the prediction of $x[n]$ and $a[n]$ is the predictor coefficients. The equation (4.15) says that the "output" $\check{x}[n]$ is a linear function of the past N samples $[\,x[n-1], x[n-2], x[n-3], \ldots, x[n-N]\,]$ multiplied by a complex weight vector $\vec{a}$. In other words, the signal $\check{x}[n]$ is *predictable* from linear combinations of the past samples. Hence the name *linear prediction*. A scheme of the linear prediction expressed by the formula (4.15) is illustrated in Fig. 4.3.

The prediction error $e[n]$, defined as the difference between the sample value $x[n]$ and its predicted value $\check{x}[n]$, is given by:

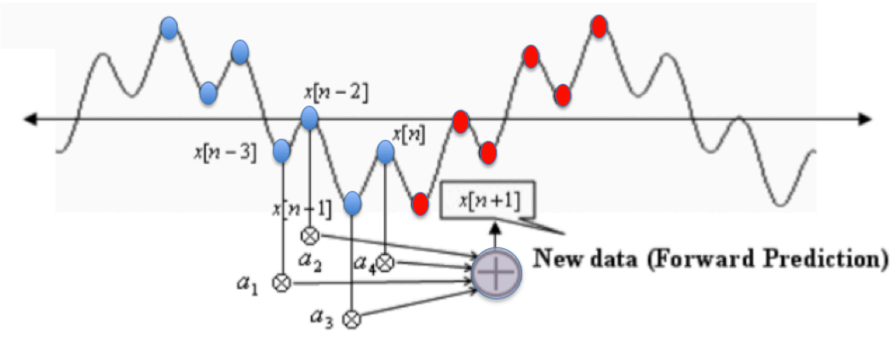

Fig. 4.3 Linear Prediction Scheme

$$e[n] = x[n] - \check{x}[n] = x[n] - \sum_{k=1}^{N} a[k]x[n-k] \qquad (4.16)$$

From this definition, a signal modelled by a linear prediction can be describe by the following feedback equation:

$$x[n] = -\sum_{k=1}^{L} a[k]x[n-k] - e[n] \qquad (4.17)$$

Where x$[n]$ denotes the data samples and $e[n]$ is the random input excitation (i.e. the prediction error) which describes the random nature of the process. This error can be defined as: $e[n] = Gu[n]$ where $u[n]$ is a zero-mean, unit-variance random signal and G is a gain factor expressed as the square root of the variance of $e[n]$. The model expressed by the formula (4.17) can be also specified in the frequency domain by the following *z*-transform.

$$H(z) = \frac{X(z)}{U(z)} = \frac{G}{1-\sum_{k=1}^{L} a[k]z^{-i}} \qquad (4.18)$$

Taking the z-transform of (4.17) shows that the linear prediction model is an *all-pole model* also known as *Auto-Regressive* (AR) model and the relative all-pole IIR filter can be used to reconstruct *x[n]* from the error signal *e[n]* and is represented with the following scheme (see Fig. 4.4).

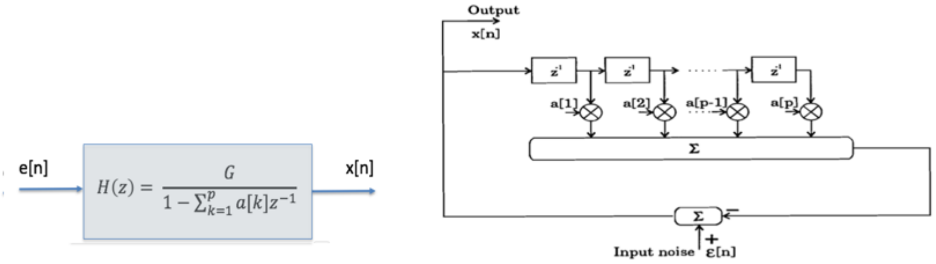

Fig. 4.4 Discrete all-pole model in the frequency domain (sx). Discrete all-pole model in the time domain (dx)

The previous model identified by the equation (4.15) is also called the *Forward-prediction* model because the value of sample *x[n]* is predict using a linear combination of *N* most recent samples. The formula can be rewritten as follows:

$$\breve{x}^f[n] = -\sum_{k=1}^{N} a[k]x[n-k] \tag{4.19}$$

where *N* is the prediction order and the superscript *f* is a reminder that we are considering the "forward" predictor. The relative estimation error is given by:

$$e_N^f[n] = \quad x[n] - \breve{x}^f[n] \quad = x[n] - \sum_{k=1}^{N} a[k]x[n-k] \tag{4.20}$$

Similarly we can also define a *Backward-prediction* model which predicts a sample *x[n-N]* from *N* future samples *x[n-N+1],…, x[n]* and the relative prediction error as follows:

$$\check{x}^b[n-N] = -\sum_{k=1}^{N} a^*[k]x[n+k-N] \qquad (4.21)$$

$$\begin{aligned} e_N^b[n] &= x[n] - \check{x}^b[n-N] \\ &= x[n-N] + \sum_{k=1}^{N} a^*[k]x[n+k-N] \qquad (4.22) \end{aligned}$$

with the prediction order *N* and $a^*[k]$ which is the set of prediction coefficient that should be estimated. Notice that the two models are based on the same *N* measurements and the two errors (4.20) and (4.22) can be interpreted as the outputs of two FIR filters (Fig.4.5) to the input *x[n]* with transfer functions *A(z)* and *B(z)* respectively:

$$A(z) = 1 - \sum_{k=1}^{N} a[k]z^{-i} \qquad (4.23)$$

$$B(z) = \sum_{k=1}^{N} a^*[k]z^{-i} + z^{-(N+1)} \qquad (4.24)$$

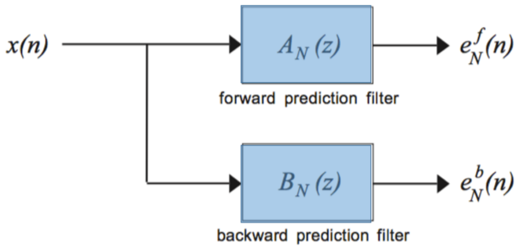

Fig. 4.5 The Forward and Backward prediction FIR filters.

As said before, the techniques for extrapolate data are based on the modeling of the available data. This is done by describing the signal as a discrete process with the Auto-Regressive (AR) model defined by the equation (4.17). Several methods exist for estimating the prediction coefficients *a[n]* of this AR model, each of them consist in a different way to minimize the mean squared errors between the predicted and the actual samples defined by:

$$\mathcal{E}_N^f \triangleq E\left[\left|e_N^f\right|^2\right] \; for\ the\ Forward\ prediction\ model \qquad (4.25)$$

$$\mathcal{E}_N^f \triangleq E\left[\left|e_N^f\right|^2\right] \; for\ the\ Baackward\ prediction\ model \qquad (4.26)$$

In this thesis we will focus our attention on three of them: The Yule-Walker method, also known as the autocorrelation method, The Burg's Method and The Modified Covariance Method.

4.4.1 Yule-Walker Equation

Let's consider the Auto-Regressive (AR) model defined by the following equation:

$$\sum_{k=0}^{N} a[k]x[n-k] = \; e[n] \qquad (4.27)$$

To get the Yule-Walker equation we can multiply both sides of the previous equation with *x[n-l]* and take the expected value:

$$\sum_{k=0}^{N} a[k]E\{x[n-k]x[n-l]\} = \; E\{e[n]x[n-l]\} \qquad (4.28)$$

where the first term of the equation which involves the data sequence and its shifted version is the typical definition of the autocorrelation function of the data defined as:

$$R[l-k] = E\{x[n-k]x[n-l]\} \tag{4.29}$$

while the second term, if we impose the orthogonality of the estimation error to each element of the data sequence is equal to zero.

$$E\{e[n]x[n-l]\} = 0 \qquad for\ 1 \le l \le N \tag{4.30}$$

The equation (4.28) can be rewrite in the follow form:

$$\sum_{k=1}^{N} a[k]\, R[l-k] = -R[l] \qquad for\ 1 \le l \le N \tag{4.31}$$

the above equations are called the normal equations or Yule-Walker equations and can be represented in the matrix form as follows:

$$\boldsymbol{Ra} = -\boldsymbol{r}$$

$$\begin{bmatrix} R(0) & R(1) & \cdots & R(N-1) \\ R(1) & R(0) & & R(N-2) \\ \vdots & & \ddots & \vdots \\ R(N-1) & R(N-2) & \cdots & R(0) \end{bmatrix} \begin{bmatrix} a_{N,1} \\ a_{N,2} \\ \vdots \\ a_{N,N} \end{bmatrix} = - \begin{bmatrix} R(1) \\ R(2) \\ \vdots \\ R(N) \end{bmatrix} \tag{4.32}$$

where the vector $\boldsymbol{r}$ is the cross-correlation vector, its *i-th* element is the correlation between the random variable *x* and the observations *x[i]*, $\boldsymbol{R}$ is the autocorrelation matrix and $\boldsymbol{a}$ is the prediction coefficients vector.

$$\boldsymbol{a} = -\boldsymbol{R}^{-1}\boldsymbol{r} \qquad (optimal\ linear\ estimator)$$

We can find the unique set of optimal prediction coefficients as long as the *N x N* matrix $\boldsymbol{R}$ is non singular. Note that this matrix is *Toepliztz* which means that all the elements on any line parallel to the main diagonal are identical. Solution of the equation (4.32) is computationally an expensive process.

The Gaussian elimination for matrix inversion is the oldest solution but this approach does not efficiently use the symmetry of *R* and *r*. A faster algorithm is the Levinson recursion proposed by Norman Levinson in 1947, which recursively calculates the solution. Once the coefficients are estimated, the AR model can be applied to predict forward and backward samples.

4.4.2 The Burg Method

Another possible method to estimate the autoregressive coefficients *a[k]* from the data sequence is the Burg algorithm. This algorithm does not estimate the autoregressive parameters *a[k]* directly but it estimates the reflection coefficients k_i for $1 \leq i \leq N$. In statistical literature they are also know as: partial correlation coefficients [34], k_i is interpreted as the partial correlation between *x(n)* and *x(n-p)* holding *x(n-1) ...x(n-p+1)* fixed.

Note that Burg algorithm is a recursive algorithm, which means that reflection coefficients k_i are estimated directly with a recursive algorithm. In each recursion step, a single reflection coefficient is estimated while the previous coefficients remain fixed. For example, to estimate the *p*-th reflection coefficient an AR(p) model is fitted to the data sequence with $p - 1$ reflection coefficient: $k_1, k_2, \ldots, k_{p-1}$ fixed to the value calculated in the previous steps. Once reflection coefficient has been estimated we can calculate the autoregressive parameter at step *p* which is related to the parameters at previous step by means the Levinson-Durbin recursion formula [33].

As stated in the previous paragraph, since the prediction coefficient depends on the index of the samples, the same will true for the forward and backward prediction errors, for recursion step p-th and index sample n they can be written as follows:

$$\check{e}_p^f[n] = x[n] + \sum_{k=1}^{N} a[k]x[n-k] \tag{4.33}$$

$$\check{e}_p^b[n] = x[n-N] + \sum_{k=1}^{N} a^*[k]x[n+k-N] \tag{4.34}$$

The new reflection coefficient k_p is determined by minimize the average of the forward and backward error powers in the stage p defined as follows:

$$\check{E}_p = \frac{1}{2} \sum_{n=p+1}^{N} \left(\left| \check{e}_p^f[n] \right|^2 + \left| \check{e}_p^b[n] \right|^2 \right) \tag{4.35}$$

where N is the length of the data sample available.

The average estimated prediction error (4.35) can be minimized by choosing the optimum reflection coefficient k_p. This is done by substituting the recursive forward and backward errors and differentiating it with respect the reflection coefficient. So, minimizing $\check{E}_p$ with respect to the reflection coefficient k_p yields

$$\frac{\partial \check{E}_p}{\partial k_p} = 2 \sum_{n=p+1}^{N} \{ (\check{e}_{p-1}^f[n] + k_p \check{e}_{p-1}^{b\,*}[n-1]) \check{e}_{p-1}^{b\,*}[n-1] + \left(\check{e}_{p-1}^{b\,*}[n-1] + k_p \check{e}_{k-1}^f[n] \right) \check{e}_{k-1}^f[n] \} = 0$$

From which the reflection coefficient can be solved

$$k_p = \frac{-2 \sum_{n=p+1}^{N} \check{e}_{p-1}^f[n]\, \check{e}_{p-1}^{b\,*}[n-1]}{\sum_{n=p+1}^{N} \left(\left| \check{e}_{p-1}^f[n] \right|^2 + \left| \check{e}_{p-1}^b[n-1] \right|^2 \right)} \tag{4.36}$$

New functions $\check{e}_p^f[n]$ and $\check{e}_p^b[n]$ can then be computed using the following equation:

$$\begin{aligned}\check{e}_p^f[n] &= \check{e}_{p-1}^f[n] + k_p \check{e}_{p-1}^b[n-1] \\ \check{e}_p^b[n] &= \check{e}_{p-1}^b[n-1] + k_p^* \check{e}_{p-1}^f[n]\end{aligned}$$

The new functions which are the forward and the backward prediction errors at step p can then be used to estimate a new reflection coefficient k_{p+1}. After the final parameter k_N has been calculated, an AR(N) model can be calculated by applying the Levinson-Durbin formula.

The recursion is initialized with $a_0[0] = 1$ and

$$\begin{aligned}a_p[m] &= a_{p-1}[m] + k_p\, a_{p-1}[p-m] \\ a_p[p] &= k_p\end{aligned} \qquad m = 1,2, \ldots, p-1 \qquad (4.37)$$

is repeated for p = 1, 2, …, N.

As previously discussed, the Burg algorithm is an iterative procedure for calculating linear-prediction coefficients of a sampled signal. At each iteration, forward and backward prediction errors are used to calculate a reflection coefficient, which is then used to update prediction coefficients and prediction errors in subsequent iterations. This is an important characteristic of the Burg method which guarantee its stability. The Levinson recursion guarantees a stable estimator, because constrains the filter poles to fall within the unit circle assuring stability. This results in extrapolation coefficients that cannot cause exponentially increasing signals with the advantage that the extrapolation will never cause numerical overflow.

4.4.3 The Modified Covariance Method

MCM estimation is not order recursive, as the Burg method is, this method also minimizes the prediction error power, but this minimization is with respect to all of the prediction coefficients simultaneously. In the modified covariance method, in fact, for each model order M, the prediction parameters are selected to minimize E_M without any constraint.

One may define separate forward and backward prediction error powers by rewriting (4.35) as:

$$\breve{E} = \frac{1}{2}\left(\breve{E}^f + \breve{E}^b\right) \tag{4.38}$$

where $\breve{E}^f$ and $\breve{E}^b$ are the forward and backward prediction error powers defined as follows:

$$\breve{E}^f = \sum_{n=L+1}^{N} \left|\breve{e}^f[n]\right|^2 = \left|x[n] + \sum_{k=1}^{N} a[k]x[n-k]\right|^2 \tag{4.39}$$

$$\breve{E}^b = \sum_{n=L+1}^{N} \left|\breve{e}^b[n]\right|^2 = \left|x[n-L] + \sum_{k=1}^{L} a^*[k]\, x[n+k-l]\right|^2 \tag{4.40}$$

The parameters in this case are given by the minimization of $\breve{E}$ with respect to each of the prediction coefficients by solving $\frac{\partial \breve{E}}{\partial a[m]} = 0$ and yield the AR coefficients as the solution of a normal equation as follows:

$$\boldsymbol{Ra} = -\boldsymbol{r} \tag{4.41}$$

This minimization of $\breve{E}$ gives rise to a system of N equations to be solved simultaneously. The expression for this system equations can be greatly simplified by defining the covariance of x[n] as follow:

$$c_x[i,k] = \sum_{n=L+1}^{N} \left(x^*[n-i]\, x[n-k] + x[n+i-L]\, x^*[n+k-L] \right) \tag{4.42}$$

where $c_x[i,k]$ is the forward-backward estimator of the autocorrelation of data sequence x[n] at lag $i - k$. The system of equations derived from the application of the minimization for m = 1, 2, …, N can be represented in matrix form by

$$\begin{pmatrix} c_x[1,1] & c_x[1,2] & \cdots & c_x[1,N] \\ c_x[2,1] & c_x[2,2] & & c_x[2,N] \\ \vdots & & \ddots & \vdots \\ c_x[N,1] & c_x[N,2] & \cdots & c_x[N,N] \end{pmatrix} \begin{pmatrix} \breve{a}[1] \\ \breve{a}[2] \\ \vdots \\ \breve{a}[N] \end{pmatrix} = - \begin{pmatrix} c_x[1,0] \\ c_x[2,0] \\ \vdots \\ c_x[N,0] \end{pmatrix}$$

The equation (4.43) is called the Modified Covariance Method due to the non-standard definition of the covariance matrix elements defined by the equation (4.42).

Note that the MCM does not guarantee the poles inside the unit circle as Burg does, resulting un unstable filter. To address this problem, the MCM model can be altered to stabilize the prediction filter. Parameters obtained using the MCM can be modified to guarantee a stable prediction filter by reflected inside the unit circle the unstable poles.

Consider p_i be an unstable pole of the linear prediction filter such that:

$$p_i = \alpha_i e^{j\beta_i} \text{ where } \beta_i > 1 \tag{4.44}$$

then this pole can be reflected inside the unit circle and the modified pole is given by:

$$p'_i = \frac{1}{\alpha_i} e^{j\beta_i} \tag{4.45}$$

4.5 Bandwidth Interpolation

Electromagnetic compatibility (EMI) between radar, the spacecraft and other science instruments is an important issue that needs attention during the design of a space mission for remote sensing, especially when low-frequency radars (i.e. Radar Sounders) are designed to characterize subsurface layering in planetary bodies. These sensors by definition generate large E-fields, but at the same time they require an interference-free environment for reception of weak subsurface echoes. Switching frequencies in the power subsystems aboard the S/C may fall into the operating frequency interval of these radars and interfere with the RF signals. Moreover, electromagnetic fields due to solar array power lines or DC/DC converters may be coupled to radar antennas and injected into the receiver. So, relevant electromagnetic interferences (EMI) are a major concern in processing radar data collected over a large bandwidth. Interfering signals produced by other devices in the spacecraft may contribute to reduce information achievable form the received echoes, they often dominate the return of a target, degrade the image in terms of the signal-to-noise ratio or because of the frequency gaps and, in an extreme case, these unwanted electromagnetic signals could be saturate the receiver and make the instrument completely useless.

The modern spectral-estimation techniques (i.e. bandwidth extrapolation), however, can be modified and used as a bandwidth interpolator to reconstruct the radar signal components after the EMI suppression process in a process we refer to as bandwidth interpolation [35].

Let's consider a signal with the presence of electromagnetic interferences (EMI), after detection and suppression of them a with dedicated processing (see Chapter 5), the spectrum shows frequency gaps that should be repaired. For this purpose, bandwidth-extrapolation algorithms can be applied directly as bandwidth interpolation to reconstruct missing signal components. Bandwidth extrapolation algorithm is used in the spectrum notch to produce synthetic data (missing spectrum samples) from the available spectrum samples.

Given a sequence of frequency samples of a target return s[n] defined as

$$s[n] = S(n\delta f, \theta) \tag{4.46}$$

where $n = 1, 2, \ldots, N$ and δf is the frequency steps between the samples. We assume that the signal has a single frequency notch in the middle of the sequence form $n = N_1$ to $n = N_2$ and the remaining samples can be divided into to sub-sequences $s_H[n]$ and $s_L[n]$ respectively, defined as follows:

$$s_H[n] = \begin{cases} s[n] & for\ N_2 \le n \le N \\ 0 & elsewhere \end{cases} \tag{4.47}$$

$$s_L[n] = \begin{cases} s[n] & for\ 1 \le n \le N_1 \\ 0 & elsewhere \end{cases} \tag{4.48}$$

Bandwidth-extrapolation algorithms could be applied directly in the frequency notch where linear prediction coefficients can be estimated separately from the high-frequency samples and low-frequency samples as follows:

$$s_L[n] = -\sum_{k=1}^{L_L} a_L[k]\ s_H[n-k] \tag{4.49}$$

$$for\ n = N_1, N_1 + 1, \ldots, N_2$$

and

$$s_H[n] = -\sum_{k=1}^{L_H} a_H^*[k]\ s_H[n-k] \qquad (4.50)$$

$$for\ n = N_2, N_2 - 1, \dots, N_1$$

where the constants L_H and L_L are AR model orders for high- and low-frequency data, respectively. In this way, two sets of data would be extrapolated into the frequency notch (see Fig. 4.6), the lower extrapolation will be performed using $a_L[k]$ as prediction coefficients while the upper extrapolation will employ $a_H[k]$. Both of them are estimated independently from the for high- and low-frequency data respectively (blue dots in Fig. 4.6) using one of the AR methods described in the previous paragraph.

Data are then reconstructed in the notch by using a weighted sum of the two extrapolations:

$$\hat{s}[n] = \left(\frac{N_2-n}{N_2-N_1}\right) s_L[n] + \left(\frac{n-N_1}{N_2-N_1}\right) s_H[n] \qquad (4.51)$$

where $\hat{s}[n]$ are reconstructed data into the frequency notch with $N_1 \leq n \leq N_2$.

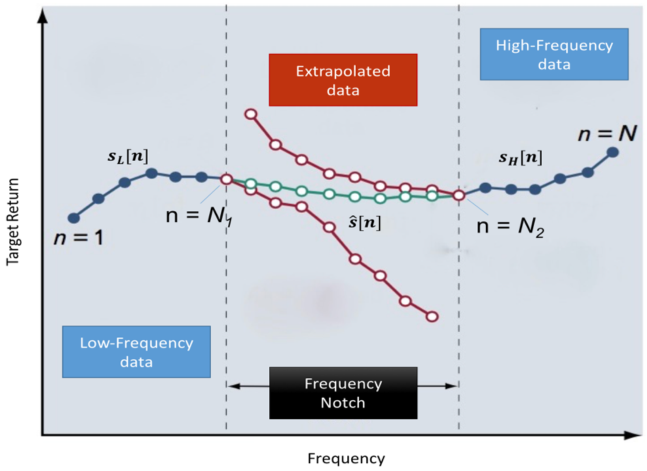

Fig. 4.6 Bandwidth Interpolation [35]

Note that bandwidth-extrapolation algorithms employed for bandwidth interpolation becomes less powerful as soon as notch width increase and a small number of data are available for estimating the linear prediction coefficients. Under this hypothesis the resulting interpolated data will be an imperfect approximations of the real data in the frequency notch. These lack of precision can be mitigated by combining high- and low-frequency data in the estimation of linear prediction coefficients needed for the bandwidth interpolation. The result is a single set of coefficients *a[n]* that are derived from data at all frequencies. The notch is then filled by extrapolating the signal from both sides.

Chapter 5

Validation of Super Resolution Approach: Multi-Scatterer Simulator

5.1 Introduction

The extrapolation technique as presented in the previous chapter can be used in radar imaging to enlarge the bandwidth and thus to improve the resolution. For a successful utilization of the autoregressive (AR) methods its necessary to investigate the behaviors of these algorithms with respect to the kind of signal, the number of available samples and the extrapolation order. In this chapter, we compare the performance of data-extrapolation algorithms for high-resolution radar imaging using three methods based on the autoregressive (AR) model, including the Yule-Walker method, the Burg method and the Modified Covariance method. The performance and the applicability of each algorithm in terms of extrapolation accuracy is compared using the simulated radar data. For these purpose a multi-scatterer simulator has been developed. This chapter describes the *algorithms and models used for simulations, discusses their implementation, and compares simulation results with measured returns from the SHARAD radar sounder.*

5.2 A Radar Signal Simulator

When an AR model is used for the calculation of the linear prediction coefficients needed in the data extrapolation, its performance will depend on a number of factors. It is important to understand the behavior of those algorithms with respect the type of signal in input the all-pole prediction filter. The way in which signals are described correctly by the AR model determines the possibility for a well suited extrapolation of the signals and a good range resolution improvement. The number of the available original data samples, the noise level present in the signal, the prediction order N chosen for the AR model, all these aspects can modify the extrapolated sequence. For this purpose, the behavior of the AR algorithms can be evaluated using a radar signal simulator.

5.2.1 Radar Echoes Modelling

As in optical theory, radar image processing produces an intensity function that indicates the target configuration. In its idealized form, the radar processing produces a point-response function in two or three dimensions with peaks of high intensity in correspondence of target's position and an exponential decay with range away from the scatterer center. Since, the radar signal can be modeled as a coherent sum of complex sinusoids with radar frequency as the independent variable and the frequency of sinusoids determined by the range time delay, it is a convenient simplification to model the radar return signal as the sum of multiple independent target returns. In a simulated scene with 1 transmitter and S scatterers, the discrete-time return signal to the receiver S_T can be modelled as coherent sum of S signals.

$$S_T = \sum_{i=1}^{N} S_i \qquad (5.1)$$

This simplification allows each scatterer to be considered independently, greatly reducing the complexity of the calculations required to simulate the return signal. The scatterer returns $S_i(f)$ are modelled as copies of the transmitted signal $X(f)$ which have been modified by the effects of transmission, propagation, interaction with the scatterer and medium, and reception. The radar signal $S_i(f)$ reflected by a reflector can therefore be written in the frequency domain as:

$$S_i(f) = \sqrt{\sigma_i}\exp(j\phi_i) \qquad (5.2)$$

where

$$\phi_i = 4\pi({}^{f}/_{c})\Delta R_i \qquad (5.3)$$

f is the radar frequency, σ_i is the radar cross section of the i-th point-scatterer, c is the speed of light and ΔR_i is the relative slant range which is given by the dot product between two vectors:

$$\Delta R_i = \hat{R} \cdot \vec{D_i} \qquad (5.4)$$

where $\hat{R}$ is the radar line of sight unit vector and $\vec{D_i}$ is the vector of the distance between the radar and the i-th scattering-point.

In terms of rectangular signal space coordinates (see Fig. 5.1), the i-th response from the generic point scatterer is:

$$S_i = \sqrt{\sigma_i}\exp\left(j2\pi\, X_i X_f + j2\pi Y_i Y_f + j2\pi Z_i Z_f\right) \qquad (5.5)$$

Note the in the case of nadir-looking acquisition geometry, the radar line-of-sight vector $\hat{R}$ is parallel to the Z-axis and we can rewrite equation (5.5) in order to make it simpler:

$$j2\pi\, X_i X_f = j2\pi\, X_i \cdot (2f/c)\cos(\alpha)\sin(k) = j2\pi\, X_i \cdot 0$$

$$j2\pi\, Y_i Y_f = j2\pi\, Y_i \cdot (2f/c)\sin(\alpha)\sin(k) = j2\pi\, Y_i \cdot 0$$

$$j2\pi\, Z_i Z_f = j2\pi\, Z_i \cdot (2f/c)\cos(k) = j2\pi\, H \cdot (2f/c)$$

$$S_i = \sqrt{\sigma_i}\,\exp\left(j2\pi Z_i Z_f\right) = \sqrt{\sigma_i}\,\exp(j2\pi \cdot (2f/c) \cdot R) \qquad (5.6)$$

where R is the range between the *i*-th scatterer and the radar.

The amplitude of the reflected radar signal depends on the transmitted power, the Fresnel coefficients of the medium in which scatterers are immersed.

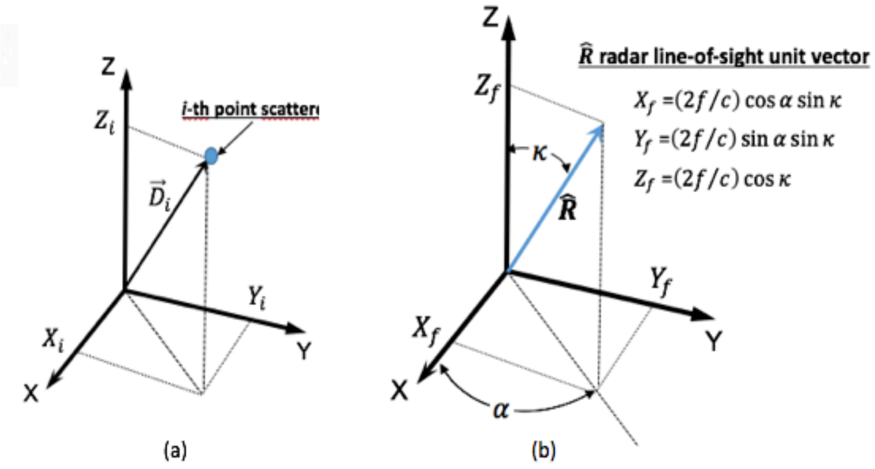

Fig. 5.1 (a) target-fixed system (b) signal-space definition

In order to make the simulated signal more realistic and with a proper Signal-to-Noise Ratio (SNR), an Additive White Gaussian Noise (AWGN) (see Fig.5.2) is added to the total radar response S_T. The Gaussian noise is assumed to be uncorrelated with itself (or "white") for any non-zero time offset τ, that is:

$$\mathcal{R}_n(\tau) = \; E[n(t)n(t-\tau)] = \frac{\mathcal{N}_o}{2}\delta(t) \tag{5.7}$$

The assumption of white Gaussian noise is valid in the very common situation included in radar applications where the noise is predominantly determined by front-end analog receiver thermal noise.

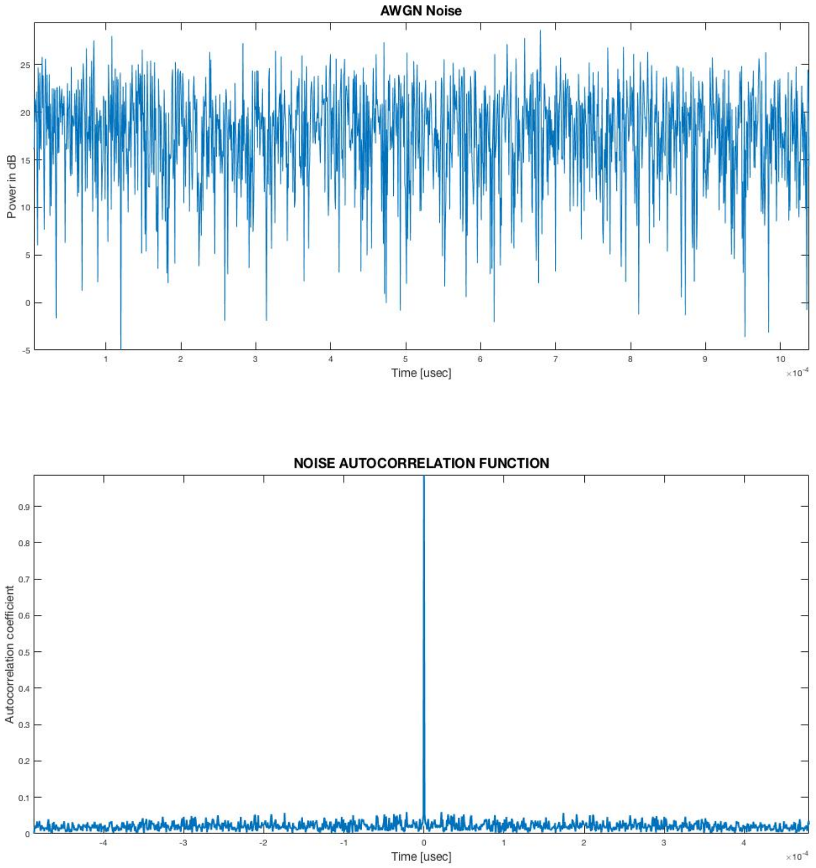

Fig. 5.2 Noise realization (up) and noise autocorrelation function (down)

The simulated signal received by the radar can be described as coherent super imposition of all the scatterers returns and generated directly in the frequency domain with the thermal noise contribution in its sampled as follows:

$$R_k = R(k\Delta f) = \sum_{i=1}^{Ns} a_i \exp(j2\pi \cdot (2\Delta f/c) \cdot R_i) + N\,(k\Delta f) \qquad (5.8)$$

where Ns is the number of scatterers in the scenario and a_i and R_i is the amplitude and the distance of each scatterer from the radar respectively.

On the basis of the typical observed double peak structures of radar signals reflected from the equatorial region of Mars, we assume that the outer layers of Mars in that region are described by a single layer placed on top of another layer and that the dielectric properties of the two layers are different. This typical radar signal can be simulated considering two identical point scatterers with same amplitude placed in a stratified medium with the dielectric proprieties shown in Fig. 5.4.

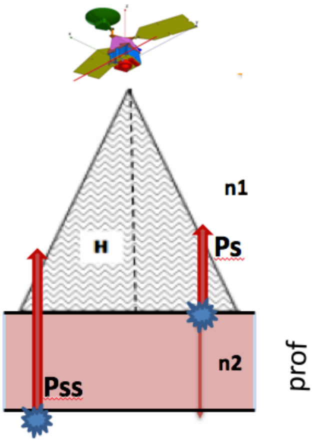

Simulation Parameters	Value
Center Frequency	20 MHz
SHARAD Bandwidth	10 MHz
Number of Samples	1385
Receive Window Length	135us
SC Altitude (H)	150 km
Scatters separation (prof)	100 m
Refractive Index	n1 = 1 vacuum n2 = 1.35 ice

Fig. 5.4 A General simulator scenario and setup for radar signal simulations (SHARAD case)

If the medium between scatterers is supposed to be uniform, the simulated signal and its relative frequency response are represented in Fig.5.5. In which signal is represented with (in blue) and without (red) AWG noise. Since the matched filter output of pulse compression process is associated with range sidelobes along with the mainlobe. To reduce these sidelobes, and improve radar capability to detect possible targets a different types of windows have been implemented and applied on simulated signal. In Fig.5.6 is shown an example of a simulated compressed pulse before and after Hanning windowing.

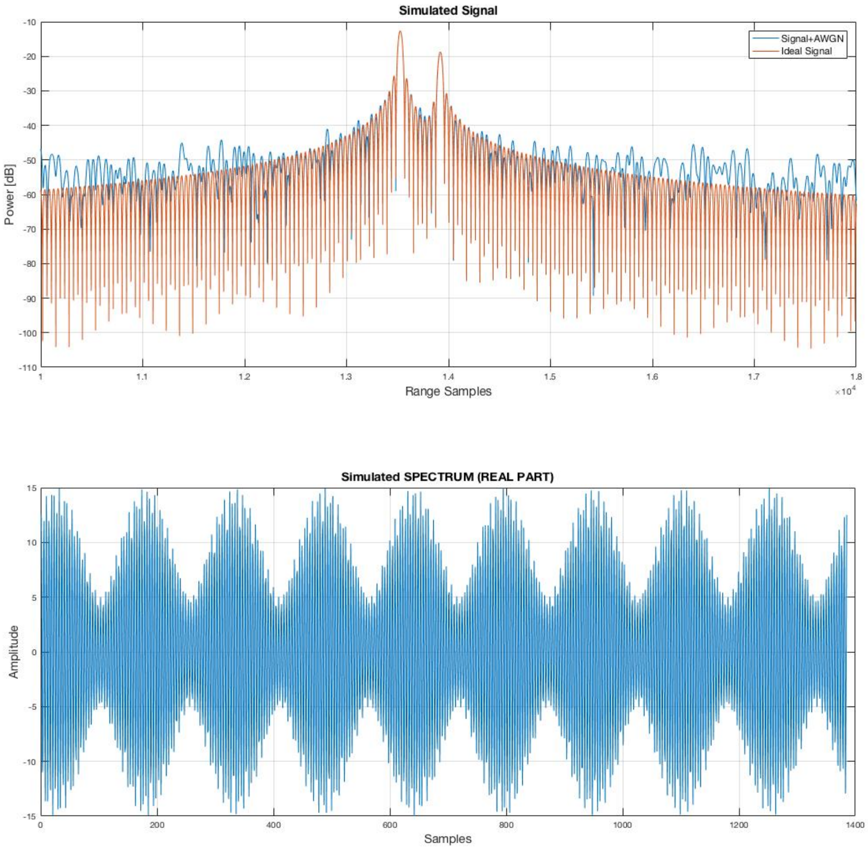

Fig. 5.5 Simulated Signal (up) and Simulated Spectrum (down)

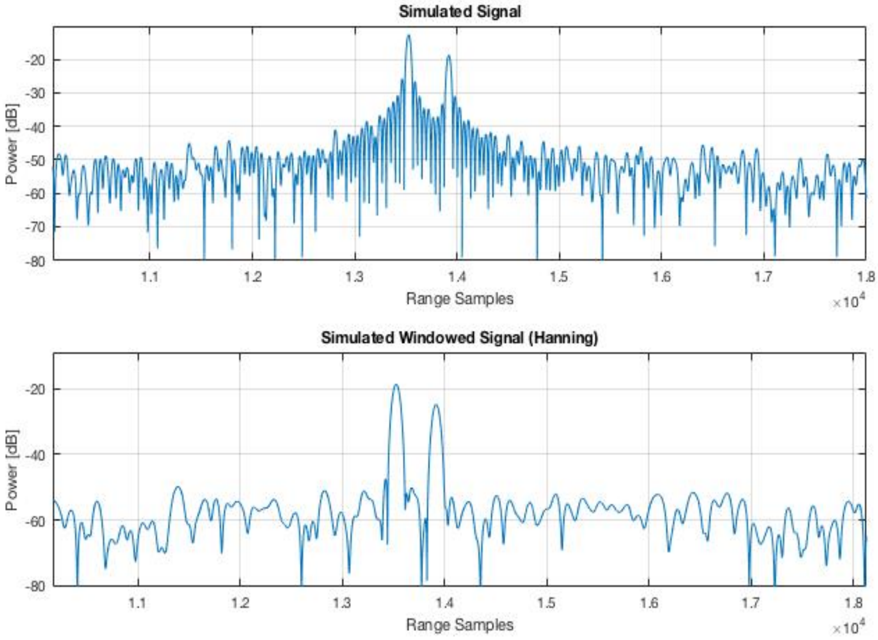

Fig. 5.6 Simulated Signal before (up) and after Hanning window function (down)

Orbiter altitude	255 – 320 km
Central frequency	20 MHz
Transmitted bandwidth	10 MHz
Antenna	10 m dipole
Transmitted power	10 W
Pulse length	85 μs
Pulse repetition frequency	700 or 350 Hz
Along-track resolution	0.3 – 1 km
Across-track resolution	3 – 7 km
Penetration depth	<~1 km
Vertical resolution	15 m (vacuum)

Table 5.1 Typical simulator parameters for radar simulations (SHARAD case)

5.2.2 Electromagnetic Interfaces Modelling

As said before, electromagnetic compability (EMC) between radar, the spacecraft and other science instruments is an important issue that needs attention during the design of a space mission for remote sensing. Switching frequencies in the power subsystems aboard the S/C may fall into the operating frequency interval of these radars and interfere with the RF signals. DC/DC converters, clocks, inverter, solar panels may be coupled to radar antennas and contribute to reduce information achievable form the received echoes and degrade the Signal-to-Noise Ratio (SNR). The presence of the electromagnetic interference (EMI) is evident in Fig. 5.7, in which a typical SHARAD spectrum clearly shows the presence of spikes located most at the upper part of the received bandwidth.

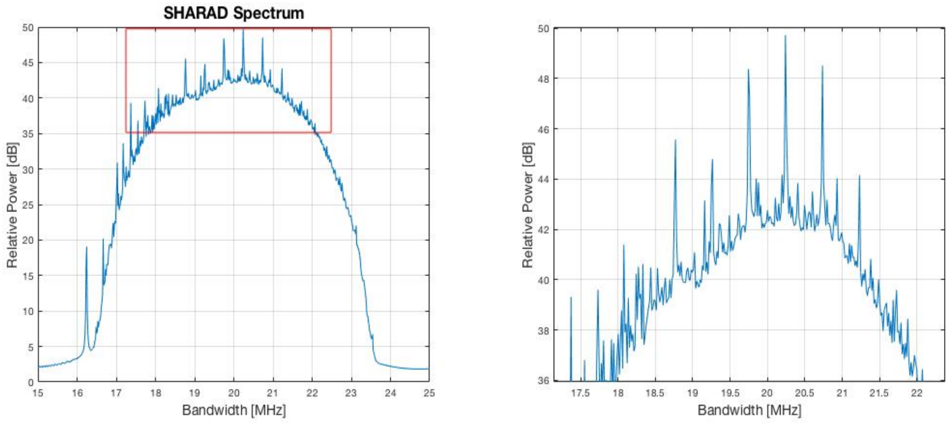

Fig. 5.7 Typical example of contaminated SHARAD spectrum

In order to study the performance and robustness of AR models in the signal bandwidth extrapolation in presence of electromagnetic interferences, we need to include EMIs in our simulator. In this section, we extend the data model of equation (5.8) to account for this additional disturbance which may arise in practice in many HF radars.

Consider with N_i the number of interferences in our spectrum, EMI interference contribution to the signal can be modelled in this way:

$$I_{T=}\sum_{i=1}^{Ni} b_i \exp(j2\pi f_i t) \tag{5.9}$$

where b_i and f_i are the amplitude and the frequency of the i-th interference. The full simulated signal can be modelled as:

$$R_k = S_T + I_T + N_T \tag{5.10}$$

Fig.5.8 shows an example of simulated complex spectral domain signal and the corresponding compressed pulse for a target consisting of two point scatterers in presence EMI.

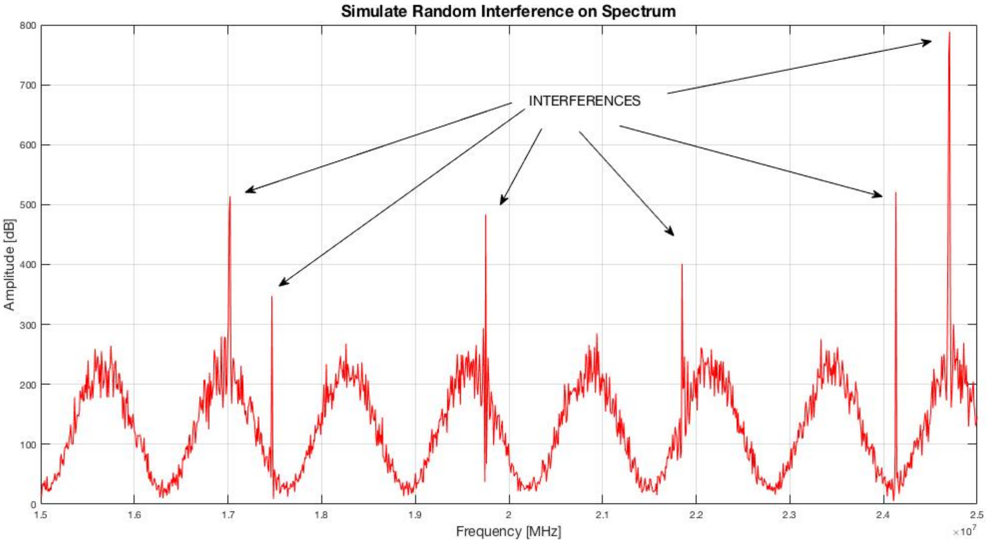

Fig. 5.8 Frequency Simulated Spectrum showing EMI

5.3 Comparison of AR Models

For better understand performances and robustness of BWE methods, a Monte Carlo approach will be used to estimate pulse compression shape, peaks positions and target powers residuals before and after BWE processing.

The methods of comparison are specific to the application at hand-data extrapolation. Using the coefficients from each method, a simulated scattered field data is extrapolated. The extended data sets are then transformed in time using an FFT. The pulse compressed signal obtained from the extrapolated data are searched for peak locations. The difference between the estimated peak locations $\widehat{\Delta}_{\tau}$, are then compared with the difference of the actual locations of peaks in the simulated signal Δ_{τ}. Each time through this process, different signal-to-noise ratios and initial phases are used in data simulation. The process is repeated many times to obtain the statistics for the image peak locations. Using the same procedure we can calculate also the relative power difference ($\Delta P_S P_{SS}$) between peaks in the pulse compressed signal obtained to the extrapolation and the original simulated signal.

The statistics calculated for the three AR methods are bias and standard deviation defined as follows:

$$B(x) = \mathcal{E}\{\widehat{\Delta}_{\tau}\} - \Delta_{\tau}$$

or

$$B(x) = \mathcal{E}\{\widehat{\Delta} P_s P_{ss}\} - \Delta P_s P_{ss} \qquad (5.11)$$

where $\mathcal{E}\{\ldots\}$ denotes the expectation operator, $\widehat{\Delta}_{\tau}$ is the estimated difference between the peaks location, Δ_{τ} is the actual peaks location of the original signal and N are trials with random noise.

The standard deviation of the estimated peaks location and power are defined by:

$$\sigma = \sqrt{\mathcal{E}\left\{\left|\widehat{\Delta}_\tau - \mathcal{E}\{\widehat{\Delta}_\tau\}\right|^2\right\}}$$

or

$$\sigma = \sqrt{\mathcal{E}\left\{\left|\widehat{\Delta}P_sP_{ss} - \mathcal{E}\{\widehat{\Delta}P_sP_{ss}\}\right|^2\right\}} \qquad (5.12)$$

We can define also another two parameters, two errors, which will be helpful to quantify the quality of data extrapolation methods. Denoted as ESR_{ext} and ESR_{emi}, Error-to-Signal Ratio in the extrapolation process and Error-to-Signal Ratio in the interpolation process after EMI suppression respectively.

These two errors will be used to better understand how the robustness of the AR methods in the coefficients estimation for the BWE processing modify the shape of the compressed pulse.

They described by the following formulas:

$$ESR_{ext} = \frac{\sum_{i=1}^{Ns} abs(R_k(i) - \widetilde{R_k(i)})^2}{\sum_{i=1}^{Ns} abs(R_k(i))^2} \qquad (5.13)$$

$$ESR_{emi} = \frac{\sum_{i\in\mathcal{Z}} abs(R_k(i) - \widetilde{R_k(i)})^2}{\sum_{i\in\mathcal{Z}} abs(R_k(i))^2} \qquad (5.14)$$

where: Ns is the number of samples of the signal sequence and $\mathcal{Z} = \{i\,!\,R_k(n) \geq threshold\}$ is the number of samples in which interferences are detected.

The first error in particular will quantify the difference sample by sample from the pulse compressed echo after extrapolation processing and the original one. The second will be calculate only in the spectrum notch after interferences cancellation and will quantify the ability of BWE processing as interpolator.

Using these measurements, the accuracy of the data extrapolation processing by each AR method can be quantified for any scenario and for any signal-to-noise ratio and interferences configuration.

5.4 Validation of Simulator Accuracy

5.4.1 Comparison with Real Data

Bibliography

[1] Merril L.Skolnik. **Introduction to Radar System**

[2] G.Picardi. **Elaborazione del Segnale Radar**

[3] D. J. Daniels, **Ground Penetrating Radar (2nd edition).** London, UK: Institution of Engineering and Technology, 2007.

[4] C. Oliver and S. Quegan. **Understanding Synthetic Aperture Radar Images.** Herndon, VA: SciTech Publishing, 2004.

[5] G. Picardi, D. Biccari, M. Cartacci, A. Cicchetti, O. Fuga, S. Giuppi, A. Masdea, R. Noschese, R. Seu, C. Federico, A. Frigeri, P. T. Melacci, R. Orosei, O. Bombaci, D. Calabrese, E. Zampolini, L. Marinangeli, E. Pettinelli, E. Flamini, and G.Vannaroni. **MARSIS, a radar for the study of the Martian subsurface in Mars Express Mission.**

[6] **MARS EXPRESS - MARSIS to planetary science archive interface control document INFOCOM technical report No. 024.005.2003**

[7] G. Picardi, D. Biccari, R. Seu, J. Plaut, W.T.K. Johnson, R.L. Jordan, A. Safaeinili, D.A. Gurnett, R. Huff , R. Orosei, O. Bombaci, D. Calabrese, E. Zampolini.**MARSIS: Mars Advanced Radar for Subsurface and Ionosphere Sounding.**

[8] Andrew Wilson, Agustin Chicarro (2004). **ESA SP-1240 : Mars Express: the scientific payload.** Noordwijk, Netherlands: ESA Publications Division.

[9] Bibring JP, Langevin Y, Mustard JF, Poulet F, Arvidson R, Gendrin A, Gondet B, Mangold N, Pinet P, Forget F (2006). **Global mineralogical and aqueous mars history derived from OMEGA/Mars express data**.

[10] A.F. Chicarro. **MARS EXPRESS MISSION: Overview and Scientific Observations**. 5th International Conference on Mars, Pasadena, California, 1999.

[11] **ESA - Mars Express - Mars Express orbiter instruments.** ESA Publications Division.

[12] R. Seu, D. Biccari, R. Orosei, L.V. Lorenzoni, R.J. Phillips, L. Marinangeli,G. Picardi, A. Masdea, E. Zampolini, **SHARAD: The MRO 2005 shallow radar.**

[13] R.Seu et alii, **The SHAllow RADar (SHARAD) Experiment, a Subsurface Sounding Radar for MRO.**

[14] Seu, R., et al. (2007), **SHARAD sounding radar on the Mars Reconnaissance Orbiter**, J. Geophys. Res., 112, E05S05.

[15] Picardi G., Sorge S., Seu R., Fedele G., Federico C., Orosei R., 1999a. **Mars Advanced Radar for Subsurface and Ionosphere Sounding (MARSIS): Models and system analysis.** Infocom TechnicalReport N.007/005/99

[16] **Spacecraft Parts Instruments: SHARAD Package**. Mars Reconnaissance Orbiter Website. Retrieved May 28, 2006.

[17] R. Croci et al.**SHARAD Design and Operation**. IGARSS 2007 Proceedings, Barcelona, 2007.

[18] **Spacecraft Parts: Gravity Field Investigation Package**. Mars Reconnaissance Orbiter Website. Retrieved May 28, 2006.

[19] **MRO HiRISE Camera Specifications**. HiRISE website. Retrieved January 2, 2006.

[20] **HiRISE: Instrument Development**. NASA Ames Research Center website. Retrieved February 7, 2006.

[21] Maltecca, L., Pecora, M., & Scandelli, L. **The Digital Electronic Subsystem of Marsis**. Proceedings of DASIA 2003 (ESA SP-532). 2-6 June 2003

[22] Seu, R. et al. 2004, Planetary and Space Science, 52, 157

[23] Seu, R., et al. (2007), **SHARAD sounding radar on the Mars Reconnaissance Orbiter**. J. Geophys. Res., 112, E05S05, doi:10.1029/2006JE002745.

[24] Susan Slavney, Roberto Orosei. **Mars Reconnaissance Orbiter, SHALLOW RADAR REDUCED DATA RECORD SOFTWARE INTERFACE SPECIFICATION**. Version 1.0 30 July 2007

[24] Picardi, G., S. Sorge, R. Seu, R. Orosei, C. Zelli, and E. Zampolini. **The subsurface investigation by Mars Advanced Radar for Subsurface and Ionosphere Sounding (MARSIS).** paper presented at International Geosciences and Remote Sensing Symposium, Honolulu, Hawaii, 24–28 July (2000).

[25] **J.P. Burg, Maximum Entropy Spectral Analysis**. Proc. 37th Meeting of the Society of Exploratory Geophysicists (1967).

[26] R.T. Lacoss. **Data Adaptive Spectral Analysis Methods.** Geophysics 36, 661 (1971)

[27] S.L. Marple. **Digital Spectral Analysis with Applications**. Prentice-Hall, Englewood Cliffs, NJ. 1987.

[28] S.B. Bowling. **Linear Prcdiaion and Maximum Entropy Spectrall Analysis for Radar Applications.** *Project Report RMP-J22*, MIT Lincoln Laboratory Radar Measuraments Program (24 May 1977), DTIC #AD·A042817.

[29] K.M. Cuomo. **A Bandwidth Extrapolation Technique for Improved Range Resolution of Coherent Radar Data**. *Project Report CjP-60*, MIT Lincoln Laboratory (4 Dec. 1992).

[30] J.Makhoul. **Linear Prediction: A Tutorial Review**. Proceedings of the IEEE, vol.63,pp.561-580.

[31] S.M. Kay. ***Modern Spectral Estimation: Theory and Application***. Englewood Cliffs, NJ: Prentice-Hall, 1988.

[32] Hsueh-Jyh Li, Ta-Yung Liu, and Sheng-Hui Yang. **Superhigh Image Resolution for Microwave Imaging**. International Journal of Imaging Systems and Technology Vol. 2, pp. 37-46 (1990).

[33] P. Stoica and R.L. Moses. **Introduction to Spectral Analysis.** Upper Saddle River, NJ: Prentice-Hall, 1997.

[34] T. W. Anderson. ***The Statistical Analysis of Time Series*** New York: Wiley, 1971.

[35] T. G. Moore, B. W. Zuerndorfer, and E. C. Burt. **Enhanced imagery using spectral-estimation-based techniques**. Lincoln Lab. J., 10(2), 171–186. (1997),

[36] J. P. Burg. **Maximum Entropy Spectral Analysis**. PhD thesis, Stanford Univ., Stanford, Calif. (1975)

[37] Porco, Carolyn. **"Questions about Saturn's rings"**. CICLOPS web site. Retrieved 2012-10-05.

[38] Cornell University News Service (2005-11-10). **Researchers Find Gravitational Wakes In Saturn's Rings**. ScienceDaily. Retrieved 2008-12-24.

[39] P.D. Nicholson et al. (2008). **A close look at Saturn's rings with Cassini VIMS.** *Icarus*. **193** (1): 182–212.

[40] Coustenis, A.; Taylor, F. W. **Titan: Exploring an Earthlike World.** World

Scientific. pp. 154–155. July 2008.

[41] Sheppard, Scott S. **The Giant Planet Satellite and Moon Page**. Departament of Terrestrial Magnetism at Carniege Institution for science. Retrieved 2008-08-28.

[42] Kurth, W.S.; Bunce, E.J.; Clarke, J.T.; et al. **Auroral Processes**. *Saturn from Cassini–Huygens*. Springer Netherlands. pp. 333–374. (2009).

[43] Lewin, Sarah. **Cassini Mission Kicks Off Finale at Saturn**. *Scientific American*. Retrieved November 30, 2016.

[44] NASA, JPL, Cassini-Huygens, Mission To Saturn and Titan, online documentation.

[45] Lorenz R.D. et al, **Cassini RADAR: prospects for Titan surface investigations using the microwave radiometer**. Planetary and Space Science 51 (2003) 353-364.

[46] G. Alberti et al. **The Processing of Altimetric Data (PAD) System for Cassini RADAR**. Mem.S.A.It. Vol.1,1. 2004